CHEMICAL VAPOR DEPOSITION OF HAFNIUM OXYNITRIDE FILMS USING DIFFERENT OXIDANTS

A Dissertation
Presented to
The Academic Faculty

by

Qian Luo

In Partial Fulfillment
of the Requirements for the Degree
Doctor of Philosophy in the
School of Chemistry and Biochemistry

Georgia Institute of Technology
December 2005

CHEMICAL VAPOR DEPOSITION OF HAFNIUM OXYNITRIDE FILMS USING DIFFERENT OXIDANTS

Approved by:

Dr. William S. Rees, Advisor
School of Chemistry and Biochemistry
School of Materials Science and Engineering
Georgia Institute of Technology

Dr. Angus P. Wilkinson
School of Chemistry and Biochemistry
Georgia Institute of Technology

Dr. Dennis W. Hess, Co-advisor
School of Chemical and Biomolecular Engineering
Georgia Institute of Technology

Dr. Z. John Zhang
School of Chemistry and Biochemistry
Georgia Institute of Technology

Dr. Russell D. Dupuis
School of Electrical and Computer Engineering
Georgia Institute of Technology

Date Approved: November 11, 2005

ACKNOWLEDGEMENTS

At the beginning, I would like to thank my advisors Dr. William Rees Jr. and Dr. Dennis Hess for their invaluable helps and guidance on my study in Georgia Tech. Their broad knowledge, creativity and enthusiasm for scientific research give me a very deep impression. They always encourage me to be creative and independent in my research. The encouragement and support that I constantly received from them are essential for the completion of this thesis.

Also, I want to thank other professors serving on my committee, they are Dr. Angus Wilkinson, Dr. Z. Zhang and Dr. Russell Dupuis. They gave me valuable advices for my research. Dr. Wilkinson also provided training on XRD measurement and helped on data analysis.

In addition, I want to extend my appreciation to those who provided me various helps during my study. Dr. Devin Brown provided training on electrical measurements. Dr. Jie Diao helped me on DC sputter. Guoan Wang and Jin Liu helped me on using equipments in clean room. Rees group members and Hess group members also gave me a lot of helps. They are Dr. Ebony Mays, Dr. Xi Zeng, Dr. Silvia Liong, Dr. Oliver Just, Dr. Javier Conception, Dr. Jack Eichler, Dr. Galit Levitin, Dr. Satya Myneni, Ashiwini Sinha and other group members.

Finally, I want to thank my family for their self-giving support. I can only complete my study with their support and encouragement.

TABLE OF CONTENTS

LIST OF TABLES

LIST OF FIGURES

SUMMARY

As the minimum feature size in complementary metal-oxide-semiconductor (CMOS) devices shrinks, the leakage current through the gate insulator (silicon oxide) will increase sufficiently to impair device operation. A high dielectric constant (k) insulator is needed as a replacement for silicon oxide in order to reduce this leakage. Hafnium-based materials are among the more promising candidates for the gate insulator, however, it is hampered by material quality and thus has been slow to be introduced into high volume integrated circuit production. Hafnium oxynitride films are deposited by Metalorganic Chemical Vapor Deposition (MOCVD) and downstream microwave Plasma Enhanced Chemical Vapor Deposition (PECVD) employing different oxidants including O_2, N_2O, O_2 plasma, N_2O plasma, N_2O/N_2 plasma, and O_2/He plasma in the current research. The effects of oxidants on deposition kinetics, morphology, composition, bonding structure, electrical properties and thermal stability of the resultant films each are investigated. The possible chemical/physical causes of these observations are developed and some mechanisms are proposed to explain the experimental results. Oxygen radicals, which are known of present in oxidizing environments are determined to play an essential role in defining both structures and the resultant electronic properties of deposited hafnium oxynitride films. This systematic investigation of oxidant effects on CVD grown hafnium oxide/oxynitride layers, in the absence of post-deposition annealing, provides new understanding to this area with potential importance to the CMOS industry.

CHAPTER 1

INTRODUCTION

Gate Dielectrics and SiO_2

Currently, Ultra-Large-Scale-Integration (ULSI) circuits such as microprocessors and semiconductor memories impact nearly everyone's life. Metal-Insulator-Semiconductor (MIS) field-effect transistors, the most important component of ULSI circuits, have been extensively developed since the first working Metal-Oxide-Semiconductor (MOS) transistor was demonstrated by Kahng and Atalla in 1960 [1]. Figure 1.1 shows the diagram of a MIS transistor. The transistor has a top gate electrode and a semiconductor substrate. Between the gate electrode and the silicon substrate, there is a thin insulating film that is termed the gate dielectric.

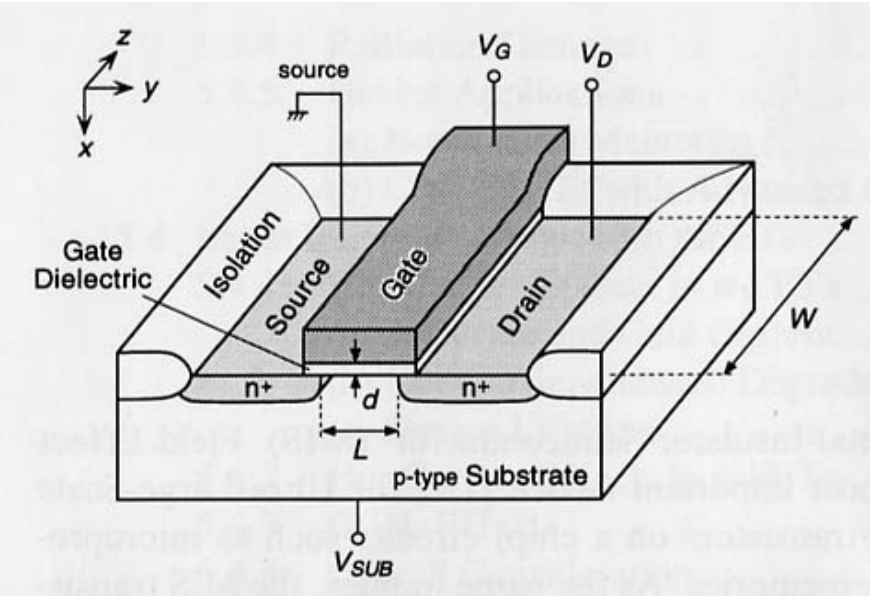

Figure 1.1 Diagram of a metal-insulator-semiconductor transistor [1].

Since the birth of MIS transistors in 1960, significant innovations and modifications in the materials and process sequences used to fabricate the transistors have taken place, such as a change in the gate electrode material from aluminum to polysilicon [2] and the use of ion implantation for semiconductor doping. However, silicon oxide (SiO_2), the heart of the MIS device structure, has never been replaced since SiO_2 is the major reason that silicon was successfully used as the base substrate for semiconductor devices. Other semiconductors such as Ge or GaAs were not selected because they do not have a stable native oxide and low defect density interface as does Si [3]. It is also the reason why the term of metal-oxide-semiconductor (MOS) is more commonly used than the generic term of MIS. The major advantages of silicon dioxide for MIS devices include:

(1) Silicon oxide is native to the silicon and can be thermally grown. The native oxide layer on a silicon substrate has a electrically stable interface with silicon; defect-charge densities are in the order of 10^{10} cm^{-2},

(2) Breakdown field of silicon oxide films is high, ~10 MV/cm,

(3) Silicon oxide thermal stabilityis good; the oxide remains amorphous at high temperature (>1000 ^{o}C) during subsequent process steps in semiconductor device integration processes.

To continuously increase integrated circuit performance at lower cost, the industry looks to Moore's law which has shown that the number of transistors on a chip doubles every 12-18 months [4]. Although the actual increased number of transistors per chip in semiconductor industry began to slow down at the end of 1980s (Figure 1.2), the number of transistors on a chip are currently more than 10^7/chip. This phenomenal

progress has been achieved by enlarging the wafer size (presently at 300 mm) and especially by scaling down the transistor dimensions. This rapid shrinking of the transistor feature size forces channel length (L in Figure 1.1) and gate dielectric thickness (d in Figure 1.1) of transistors to decrease.

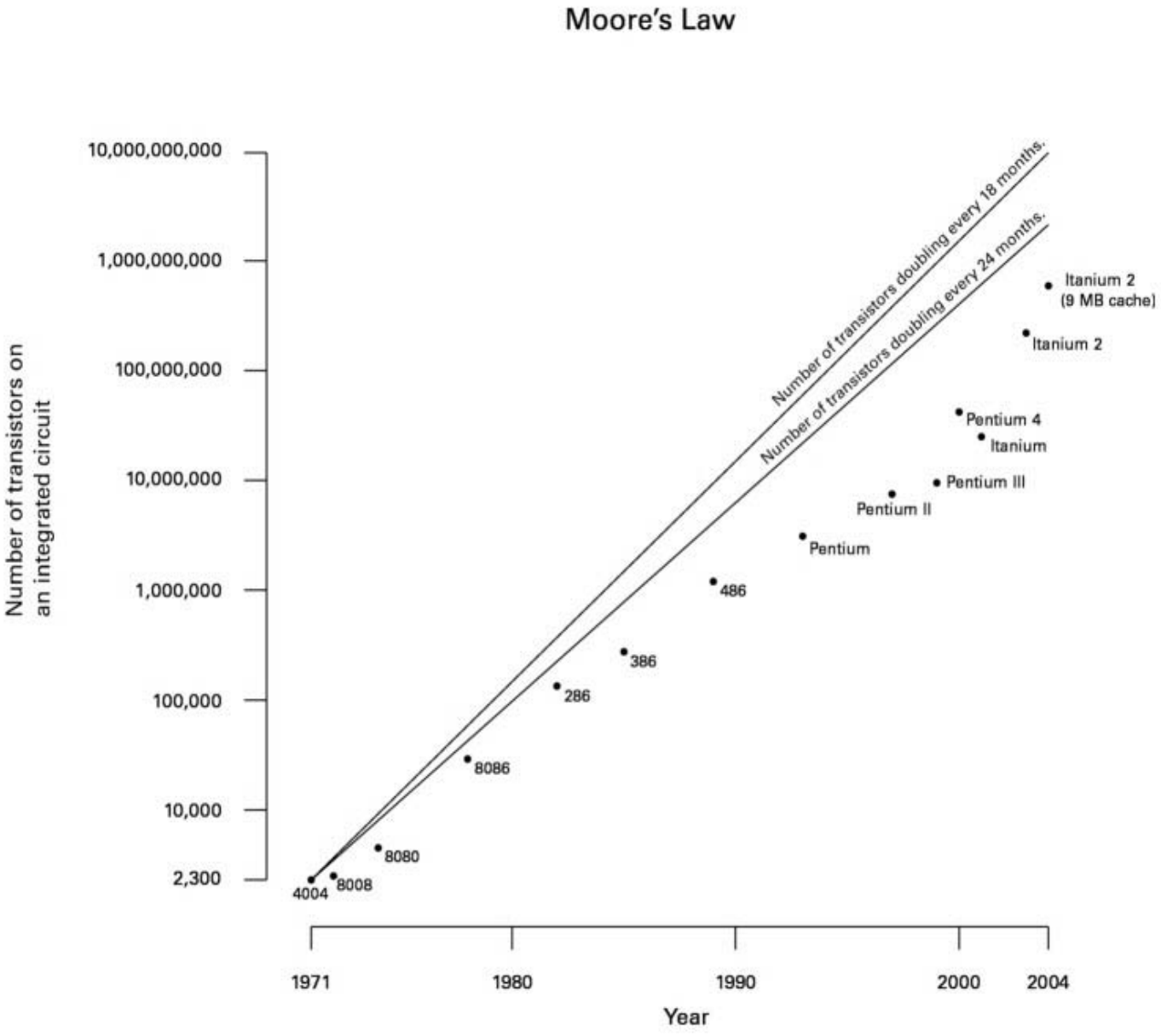

Figure 1.2 Moore's law vs Intel processor transistor counts [5].

Circuit performance improvement by shrinking can be illustrated by a simple model of the drive current in a Field-Effect-Transistor (FET) [1]. The equation for the FET drive current can be written as:

$$I_D = \frac{W}{L}\mu C_{inv}\left(V_G - V_T - \frac{V_D}{2}\right)V_D \qquad (1)$$

where W and L are the width and length of the transistor channel individually, μ is the carrier mobility, C_{inv} is the gate dielectric capacitance when the channel is in the inversion region, V_G is the gate voltage, V_D is the drain voltage, and V_T is the threshold voltage. As shown by equation (1), the drain current I_D increases with V_D until it saturates when $V_{D,sat} = V_G - V_T$,

$$I_{D,sat} = \frac{W}{L}\mu C_{inv}\frac{(V_G - V_T)^2}{2} \qquad (2)$$

carrier mobility μ is nearly constant and gate voltage V_G and threshold voltage V_T cannot change over a wide range due to reliability concerns and the intrinsic properties of semiconductor silicon. As a result, shorter gate length and higher gate dielectric capacitance are needed to increase the saturated drain current and the transistor speed. For a parallel plate capacitor, the capacitance is given by

$$C = \frac{\kappa\varepsilon_0 A}{t} \qquad (3)$$

where κ is the dielectric constant of the gate material, ε_0 is the permittivity of the free space, A is the capacitor area, and t is the thickness of the gate dielectric. Equation (3) shows that a reduction in the thickness of the gate dielectric increases the capacitance of the gate dielectric and thus the drain current of the transistors. Indeed, the thickness of

gate dielectrics and their lateral dimensions have been scaled down simultaneously for more than 40 years so that the industry could keep pace with or adhere to Moore's law. The International Technology Roadmap for Semiconductors (ITRS) indicates a set of requirements for each device generation to offer a guide for development of subsequent generations in the semiconductor industry. In this document, technology nodes based on the half metal pitch size of Dynamic Random Access Memory (DRAM) devices are used to represent the generations. According to ITRS 2004 [6], the technology node is 90 nm in 2004 and will be 65 nm in 2007. At the 90 nm node, the gate dielectric thickness in DRAM must be scaled down to 2.3 nm. If silicon oxide is to remain the gate dielectric layer at the 65 nm node, the thickness of the layer must be as small as 0.8 nm.

With the gate dielectric thickness and channel length shrinking, MOSFET devices begin to suffer problems induced by the increased lateral ($\xi_{//}$) and perpendicular (ξ_i) electric fields within the small transistors. The increased ξ_i causes more carriers to be injected into the gate dielectric from the channels or the gate electrode, as shown in Figure 1.3 [1]. Also, increased $\xi_{//}$ generates more electron-hole pairs in the substrate that may surmount the interfacial energy barrier.

Although the power supply voltage V_{cc} used to operate the transistors is reduced (scaled) with the transistor feature size, the voltage decreasing speed is much slower than the transistor-shrinking rate. Thus, unavoidably, ξ_i and $\xi_{//}$ increase with scaling, and it is believed that the perpendicular electric field must therefore remain at a level of ~3-5 MV/cm for future circuits.

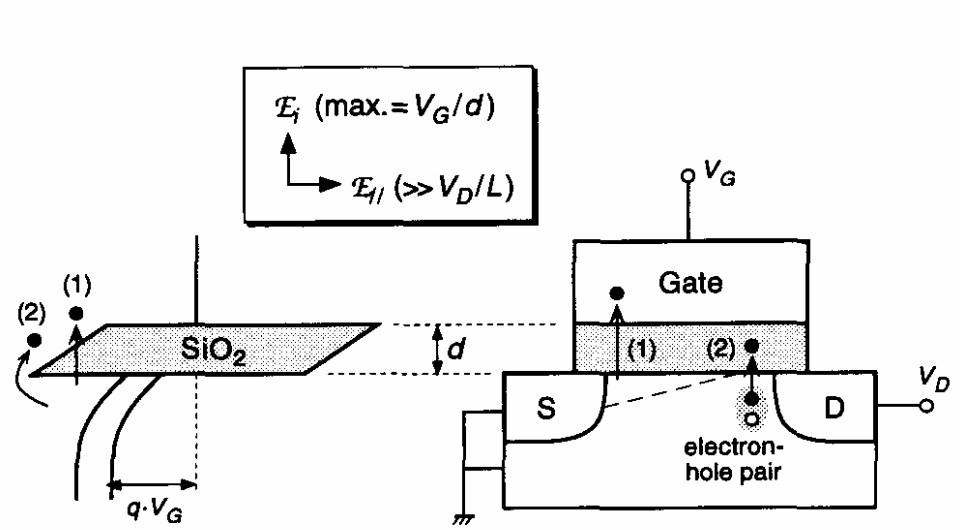

Figure 1.3 Schematic band diagram of FET structure to illustrate the electric fields in the transistors [1].

With such a high electric field, when the SiO_2 gate dielectric is thinner than 3 nm, the leakage current is dominated by direct quantum mechanical tunneling through the dielectric layer and therefore increases exponentially [7]. Figure 1.4 shows the gate current density as a function of silicon oxide thickness for 35 nm transistors [8]. The two horizontal lines indicate the maximum allowable gate current densities for desktop computers (lower line) and portable applications (higher line) individually. It is obvious that silicon oxide films with thickness less than 1.3 nm have unacceptably high leakage current (>1 A/cm^2) for both applications. At the 65 nm node, as projected by ITRS, a still thinner film (0.8 nm) will be needed. Such thin films with only several monolayers of silicon oxide induce a number of problems, including high leakage current, poor reliability, boron penetration from the doped polysilicon, and the stringent demands of film uniformity and thickness control [9]. Furthermore, such concerns demonstrate that

the transition between 90 nm and sub-90 nm nodes requires more than a simple feature shrinkage as has been the case with classical device scaling. Significant innovations, including new materials, processes and device structures, must be devised to allow a successful transition [10, 11]. Among these changes, high dielectric constant (high-k) materials, as potential alternative to silicon oxide gate dielectric, have recently attracted intense attention.

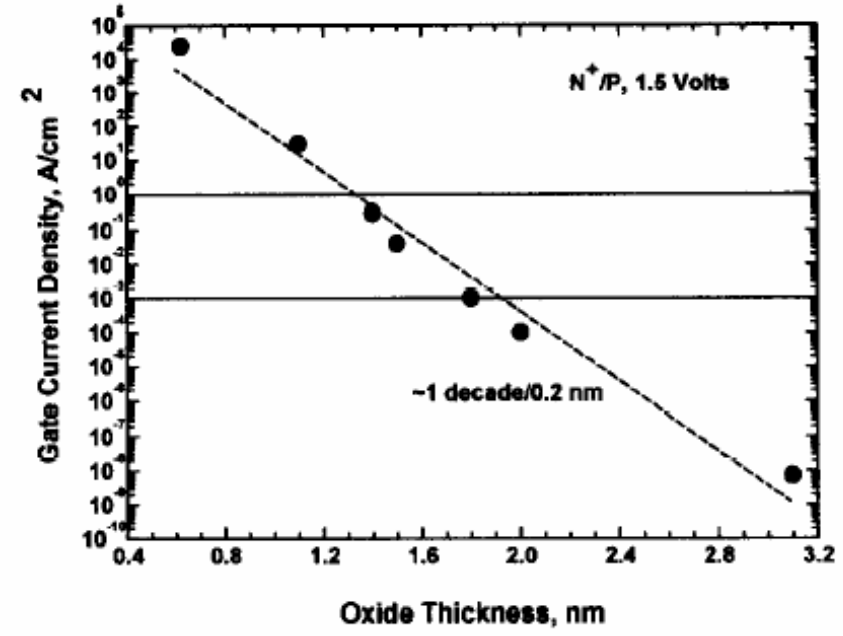

Figure 1.4 Gate leakage current vs silicon oxide thickness at 1.5 V for 35 nm NMOSFETs [8].

High-k Materials

Origin of High Dielectric Constant

As equation (1) indicates, an increase in the dielectric constant of the gate insulator can also increase the capacitance of the gate structure analogous to a reduction of the gate dielectric thickness. For an identical capacitance, high-k dielectrics can have

larger thicknesses than silicon oxide. The gate capacitance can be conveniently expressed by the equivalent oxide thickness (EOT) with respect to silicon oxide.

$$EOT = t \times \frac{k_{SiO_2}}{k_{High-k}} \qquad (4)$$

where k_{SiO2} is 3.9, $k_{High\text{-}k}$ is usually larger than 10, and t is the thickness of the high-k dielectric. With the same EOT, the larger physical thickness of high-k dielectrics results in a reduction of the gate leakage current while generating sufficient inversion charge in the channel of transistors for device operation.

The static dielectric constant is a function of material polarizability, including the electronic contribution and the lattice contribution (also called ionic contribution) [12],

$$k = k_e + k_l \qquad (5)$$

the electronic component is the optical dielectric constant ε_∞ which is often equated to the square of the refractive index,

$$k_e = \varepsilon_\infty = n^2 \qquad (6)$$

and the electronic polarizability is determined by the electrical field induced electron redistribution. For a dielectric material subjected to an electric field, electrons transfer between occupied and unoccupied electronic states. Due to the electron shift with respect to the nuclei in an electric field, an electric dipole moment is produced. The magnitude of the electron redistribution is related to the applied electric field and the energy gap between initial and the final electronic states, as described by equation (7):

$$k_e \propto \frac{V_{ab}^{\ 2}}{E_{ab}} \qquad (7)$$

V_{ab} is the electric field operator applied to the dielectric, E_{ab} is the energy gap between initial a and final b states. In this scenario, because the initial state is the highest occupied level in the valence band and the final state is the lowest unoccupied level in the conduction band, the energy gap for a metal oxide compound is E_g as shown in Figure 1.5 [13]. Clearly, oxides with smaller energy gaps have higher electronic polarizability and thus higher dielectric constants.

Usually, transition metal oxides have small energy gaps because of the partially filled d-orbitals from transition metal atoms. For these compounds, the lowest conduction band consists of π* antibonding orbitals formed from metal d orbitals (d_{xy}, d_{xz}, d_{yz}) and oxygen p orbitals. The wave functions of these d orbitals from transition metal ions have little overlap with the wave functions of oxygen p orbitals and thus the π bonding between them is very weak (Figure 1.6) [13]. The splitting energy Δ between the bonding and antibonding orbitals, which is determined by the overlap of orbitals, is also small. As Figure 1.5 shows, the small splitting energy leads to a small band gap E_g. In contrast, the lowest conduction band in silicon oxide is formed by the σ* antibonding orbitals. The σ bonds are formed by the overlap of Si s, p orbitals and O p orbitals and are much stronger than the π bonds in metal oxides (Figure 1.6). The larger splitting energy gives silicon oxide a larger band gap than that of transition metal oxides. Based on equation (7), the small band gap in transition metal oxides gives them a high electronic polarizability.

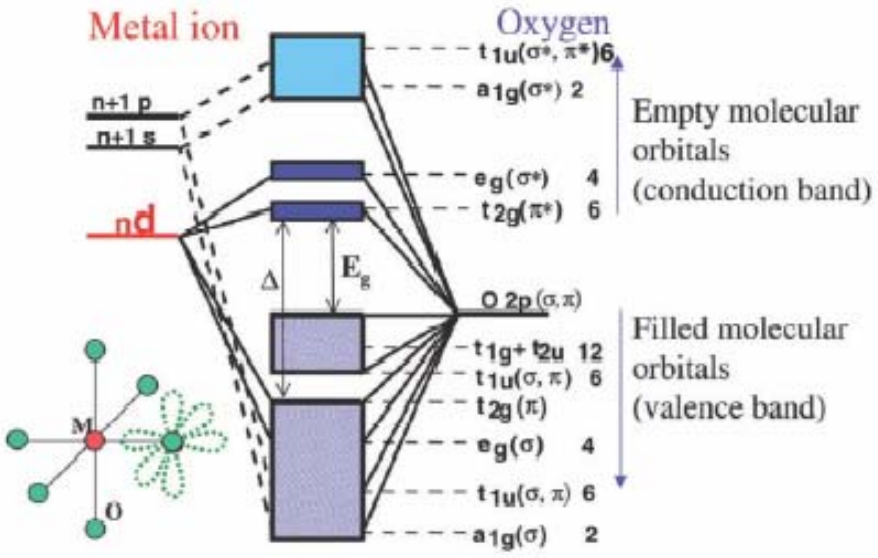

Figure 1.5 The molecular orbital spectrum of the octahedral metal-oxygen complex. Δ is the smallest energy gap between the bonding and anti-bonding orbital. E_g is the band gap between the conduction band and valence band [13].

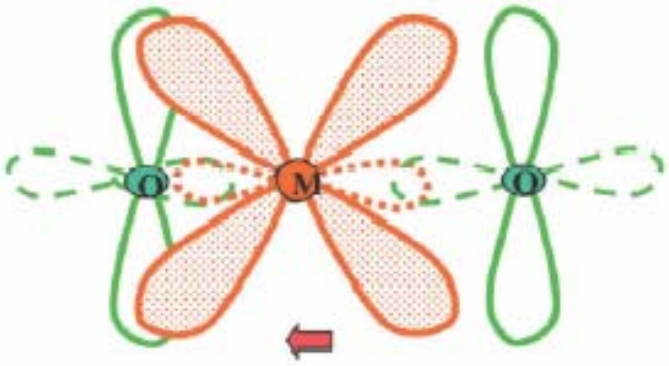

Figure 1.6 Schematic of the p-p σ bond (broken line) and p-d π bond (continuous line) between the metal ion and the oxygen ions [13].

For most of the wide band gap oxides in the operating frequency range for CMOS devices (100 MHz – 10 GHz), ε_∞ is typically within the range of 4-5 that does not

represent the main contribution to the dielectric constant for high-k materials. Thus, the ionic contribution is larger than the electronic portion in high dielectric constant materials. The ionic polarizability can be expressed as:

$$k_l = \frac{Ne^2 Z_T^{*2}}{m\omega_{TO}^{\ 2}} \qquad (8)$$

where N is the number of ions per unit volume, e is the electronic charge, Z_T^* is the effective charge, m is the reduced ion mass, and ω_{TO} is the frequency of the optical phonon. Large ionic polarizability can be obtained if Z_T^* is large and ω_{TO} is small. Usually, transition metal ions have large effective charge; $\omega_{TO}^{\ 2}$ is proportional to the reduction of the force constant (K) of metal-oxygen bonds after application of the electric field. Such effects can be expressed by

$$\omega_{TO}^{\ 2} \propto K = K_0 - \frac{V_{T1u}^2}{E_{T-A}} \qquad (9)$$

where K_0 is the force constant of the metal-oxygen bond that is determined by the σ bond without the effect of applied electric field, V_{T1u} is the vibronic constant for the bond vibrations in the electric field, and $E_{T\text{-}A}$ is the energy difference between the states before and after application of the electric field. The vibrations correspond to the displacement of metal ions with respect to oxygen atoms; these vibrations have the same symmetry (T_{1u}) as those responsible for the generation of electric dipole moments. The vibrations increase the overlap of the metal d states and the oxygen p states. The increased d-p overlap provides a path for electrons to transfer from oxygen atom to metal atom. The π-type electron "feedback" weakens the M-O σ bonds and reduces the force constant of the vibrations [14]. This effect is inversely proportional to $E_{T\text{-}A}$ in equation (9). Because $E_{T\text{-}A}$

is the same order of magnitude as E_g, the small E_g in transition metal oxides also results in a high ionic polarizability as indicated by equations (8) and (9).

Barrier Offsets

In addition to the high dielectric constants, potential dielectric candidates are also required to have high barrier offsets. For electrons transferring from the silicon substrate to the gate electrode, the conductance barrier height ΔE_c is:

$$\Delta E_c \cong q\left[\chi - \left(\Phi_M - \Phi_B\right)\right] \qquad (10)$$

As Figure 1.7 [9] shows, χ is the electron affinity of the semiconductor, Φ_M is the metal work function, and Φ_B is the potential barrier between the metal and the dielectric. For electrons transferring from the metal gate to the silicon substrate, the barrier height is:

$$\Delta E_c = \Phi_B \qquad (11)$$

The leakage current through the dielectric layer may originate from three mechanisms: direct tunneling transport, Frenkel-Poole emission or hopping conduction [15]. The equations describing these currents are:

$$J_{DT} = \frac{A}{t_{diel}^2}\exp\left(-2t_{diel}\sqrt{\frac{2m^*q}{\hbar^2}\left(\Delta E_c - \frac{V_{diel}}{2}\right)}\right) \qquad (12)$$

where A is a constant, t_{diel} is the thickness of the dielectric, m* is the electron effective mass in the dielectric, and V_{diel} is the voltage on the dielectric;

$$J_{FP} = E\exp\left(-\frac{q}{kT}\left(\Delta E_c - \sqrt{\frac{qE}{\pi\varepsilon_i}}\right)\right) \qquad (13)$$

where ε_i is the dielectric constant of the insulator;

$$J_{hop} = \frac{q^2 l^2 n^* \Gamma E}{kT} \qquad (14)$$

where l is the distance between two hopping sites, n* is the density of the free electrons in the dielectric, and Γ is the average hopping frequency.

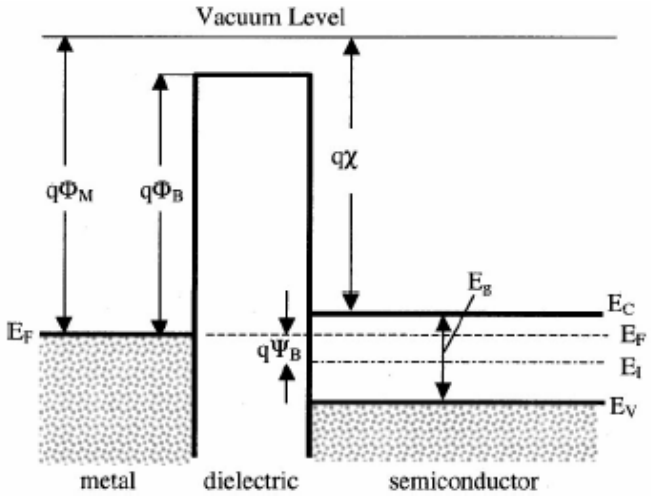

Figure 1.7 Energy band diagram for an ideal MIS capacitor with n-type silicon substrate [9].

For dielectrics without defects, the leakage current follows the direct tunneling transport mechanism; for defective dielectrics, Frenkel-Poole emission or hopping conduction is the dominating mechanism. The leakage current in dielectrics increases exponentially with barrier offsets decreasing, as the above equations show. Thus, high-k dielectics acceptable for gate insulator applications must also have large barrier offsets.

Robertson calculated the barrier offsets for some metal oxides including several high-k dielectrics by the model of metal induced gap states (MIGS) [16, 17]; the calculated band offsets are shown in Figure 1.8 [17], where both conduction band offsets ΔE_c and valence band offsets ΔE_v are indicated. These values indicate the relative difficulty in transporting electrons or holes between the silicon substrate and a specific

dielectric. Clearly, conduction band offsets are usually smaller than valence offsets. As a result, conduction band offsets are generally considered in the selection of gate dielectrics. Those metal oxides with conduction band offsets <1.0 eV can be precluded for gate dielectrics applications because of high leakage currents. Figure 1.8 also shows the relations of band gaps of silicon and high-k dielectrics:

$$E_{BG,High-k} = E_{BG,Si} + \Delta E_c + \Delta E_v \qquad (15)$$

Although the valence band offsets for different oxides are not the same, it is believed that larger band gaps generally indicate larger conduction band offsets. Undoubtedly, oxides with larger band gaps have smaller leakage currents since the conduction band offsets are increased. Furthermore, it should be noted that the dielectric constant and the leakage current of a high-k oxide have an inverse relationship. Therefore, semiconductor devices require trade-offs between high dielectric constant and low leakage current to establish the most suitable material candidate to replace silicon oxide. Robertson's calculations offer reasonable predictions for the selection of high-k materials, but the unpredictable interface effects between metal and dielectric and semiconductor and dielectric increase the difficulties of identifying the appropriate high-k layer.

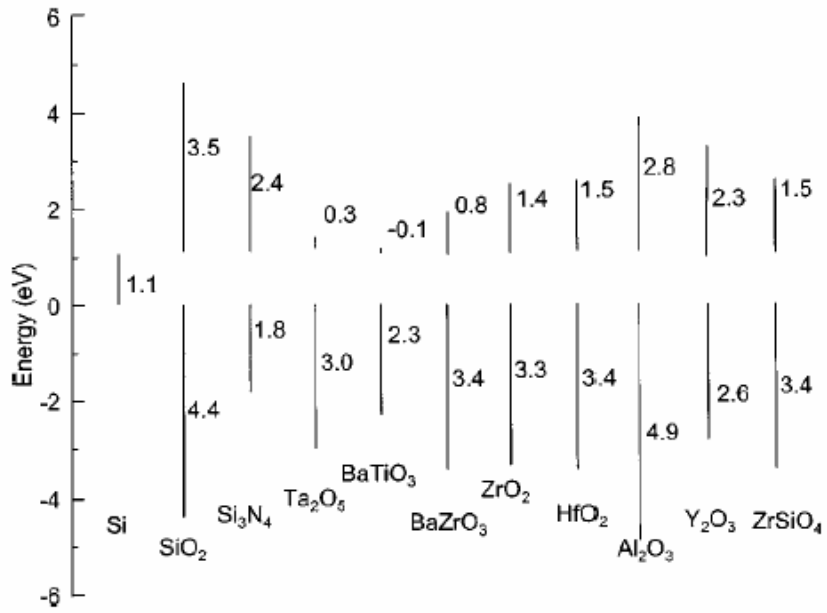

Figure 1.8 Conduction and Valence Band offsets of several potential high-k gate dielectric materials calculated by Robertson [17].

Progress and Limitations in High-k Research

Based on the calculations by Robertson [17], the dielectric constants and band gaps of a number of high-k candidates are compared in Figure 1.9 and Table 1.1. These potential gate dielectrics have been experimentally studied for possible incorporation into transistor structures.

As Table 1.1 indicates, Al_2O_3 and Si_3N_4 have many favorable properties, such as large conduction band offsets (> 2.4 eV), relatively large band gaps (8.8 eV and 5.3 eV respectively), and good thermal stability. Recent studies have demonstrated that Al_2O_3 and Si_3N_4 can remain amorphous after high temperature annealing. Al_2O_3 also has low leakage current because of the small conduction band offsets and low defect density [18-22]. In spite of these advantages, both materials have a common shortcoming: low dielectric constant (9 for Al_2O_3 and 7 for Si_3N_4). Their low dielectric constants prevent

significant shrinkage of the gate dielectric thickness; thus neither material is considered as the long-term replacement for silicon oxide.

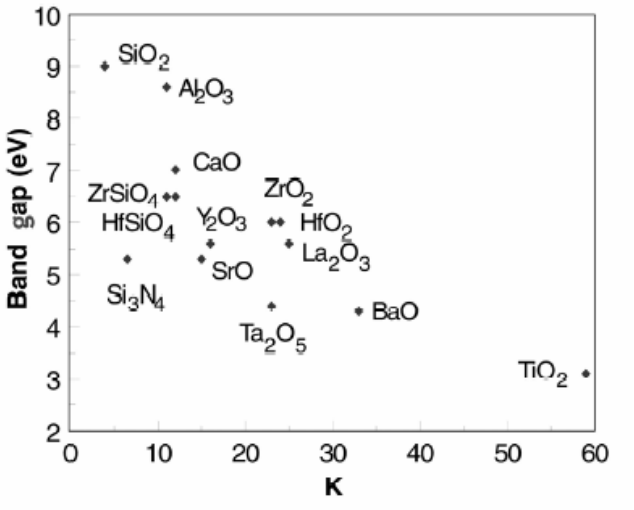

Figure 1.9 Static dielectric constants and band gaps of potential high-k dielectrics [17].

Table 1.1 Calculated dielectric constants, experimental band gaps and conduction band offset of high-k dielectrics [17].

	K	Gap (eV)	CB offset (eV)
Si		1.1	
SiO_2	3.9	9	3.2
Si_3N_4	7	5.3	2.4
Al_2O_3	9	8.8	2.8 (not ALD)
Ta_2O_5	22	4.4	0.35
TiO_2	80	3.5	0
$SrTiO_3$	2000	3.2	0
ZrO_2	25	5.8	1.5
HfO_2	25	5.8	1.4
$HfSiO_4$	11	6.5	1.8
La_2O_3	30	6	2.3
Y_2O_3	15	6	2.3
a-$LaAlO_3$	30	5.6	1.8

At the right side of Figure 1.9 are oxides with relatively large dielectric constants; TiO_2 is a typical material in this category. Although TiO_2 has a high permittivity of 80-110, it crystallizes at temperatures ~400 ˚C or lower [23, 24]. Unfortunately, polycrystalline films are not desirable for gate dielectrics because of their high leakage current and non-uniform electric properties caused by the random orientations of polycrystalline grains. BaO and SrO also have relatively high dielectric constants, but they are excluded from the candidate list for their sensitivity to water. ZrO_2, HfO_2 Pr_2O_3 and La_2O_3 are the most promising oxides, but ZrO_2 is not stable when in contact with the silicon substrate at high temperatures, and Pr_2O_3 and La_2O_3 are hygroscopic [25-29].

Because most high-k materials have advantages and disadvantages, systems of materials termed pseudobinary or pseudoternary that combine the advantages of two or three components have been of interest recently. In such systems, a tradeoff can be established between their advantages and disadvantages. These systems include silicates (M-Si-O) [30], aluminates (M-Al-O) [31] and other more complicated sytems (e.g., Zr-Sn-Ti-O [32, 33]). These systems usually have relatively high dielectric constants because they contain a transition metal oxide. Also, they are amorphous and can withstand high temperature annealing without crystallization because of their silicon oxide component. For these systems, it is necessary to find the optimal composition range of components. A low transition metal oxide portion decreases the dielectric constant of the compound, while a high transition metal oxide level may lead to phase separation of the compounds at high temperatures [34, 35].

Among the various high-k candidates, the semiconductor industry has focused most of their current interests on hafnium-based systems. Considerable efforts have been

expended with the hafnium-based system, including hafnium oxide, hafnium oxynitride, hafnium silicate and hafnium silicon oxynitride [36-38]. Indeed, encouraging results have recently been announced on hafnium – based high-k dielectrics [39]. Despite such progress, high-k dielectrics are still not ready for introduction into integrated circuit (chip) high volume production [40]. The limitations that remain consist of intrinsic and extrinsic problems as described below.

(1) Dielectric constants of some oxides or binary/ternary systems are not sufficiently high, to warrant introducing them into the overall fabrication sequence.

(2) Thermal stabilities are not sufficient to withstand high temperature (>1000 °C) annealing in subsequent processing steps; some metal oxides crystallize during the deposition process. Polycrystalline gate dielectrics are problematic because the grain boundaries are good leakage paths for charge carriers. Also, the uncontrollable grain size and orientation lead to irreproducible electrical properties. In addition to the crystallization concern, some of the metal oxides react with the silicon substrate and produce an interface layer that consists of M-Si and M-Si-O. The interface layer unavoidably decreases the capacitance of the gate stack due to the reduced dielectric constant and thus increases the EOT although this does reduce the leakage current of the system as equations (16) (17) demonstrate:

$$\frac{1}{C_{tol}} = \frac{1}{C_{high-k}} + \frac{1}{C_{\text{int}erface}} \qquad (16)$$

$$EOT_{tol} = t_{\text{int}erface} + EOT_{high-k} \qquad (17)$$

Because it is difficult to avoid the formation of an interface layer without the insertion of a barrier layer between the gate dielectric and the substrate, it is extremely important to select a material that has a stable and controllable M-Si-O system, especially when the EOT will fall below 1 nm.

(3) Interface trap and bulk defect densities are often high, which degrades the carrier mobility in transistors. High-k metal oxides have a more rigid bonding structure than silicon oxide because of their bonding is ionic with a high coordination number; these attributes account for the fact that high-k oxides are poor glass formers [41]. Although oxides have high heats of formation of non-stoichiometric defects, the defect densities in these metal oxides are still high because the oxide network cannot easily relax and the dangling bonds within the network cannot be removed by re-bonding. The defects can exist both at the interface and in the bulk oxide in forms such as oxygen vacancies, interstitial oxygen, -OH groups, and Si-H bonds [42, 43]. Carrier mobility in transistor channels may be reduced because interface states trap carriers. In addition, the flat band voltage and thus the transistor threshold voltage shifts with the incorporation of fixed oxide charges as indicated by equation (18).

$$V_{FB} = \Phi_{ms} + \frac{Qt}{K\varepsilon_0} \qquad (18)$$

where Φ_{ms} is the work function difference between the metal electrode and the semiconductor, Q is the fixed oxide charge, t is the thickness of the films and K is the dielectric constant.

(4) Leakage currents through the dielectrics are high so that device performance is reduced. Intrinsically, high-k dielectrics have small band gaps that usually lead to

high leakage currents. Often, however, the high leakage current of high-k dielectrics originates from defects in the deposited films. The defects introduce energy levels into the band gap of metal oxides and increase the probability that electrons or holes can transport through the dielectric.

(5) Distinct from the growth of silicon oxide by silicon oxidation, high-k dielectrics have to be deposited. The deposition process must be compatible with the other steps in CMOS processing, cost and throughput. Also, the poly-silicon gate metal must be changed to another more suitable conductor such as Pt, TiN or Ru because the interface between poly-silicon and high-k oxides increases the EOT of the gate dielectrics.

Although substantial effort has gone into the development of hafnium-based high-k materials, the problems have not been completely solved; therefore, the industry has postponed the introduction of high-k materials to the 45 nm node. Device reliability concerns caused by defects in hafnium-based materials remains one of the biggest challenges. To reduce the interface trap density, HfO_2 films are annealed in O_2, H_2, N_2 or D_2 to stabilize dangling bonds and diminish oxygen vacancies [44-47]. However, annealing normally increases the thickness of interfacial layers and thus the equivalent oxide thickness (EOT) of the films, and increases the process complexity. To improve the thermal stability and dopant/electron barrier properties of HfO_2 films, nitrogen atoms are introduced into HfO_2 films analogous to approaches invoked for SiO_2. These hafnium oxynitride films are obtained by sputtering in N_2, chemical vapor depositions in NO or NH_3, or (primarily) post-deposition annealing in NH_3 or N_2. Although specific properties (e.g., dielectric constant, leakage current and breakdown field) of the films have been

improved by these post-deposition treatments, some aspects of transistor performance are also degraded by introducing large hysteresis and low carrier mobility. The fundamental causes behind the improvement and degradation are not yet clear. Therefore, improved understanding of deposition-film structure-film property relationships and further development of processing methods are essential to allow the semiconductor industry to move forward to sub-65 nm technologies in 2007.

Objective

Recently, different oxidants including O_2, N_2O, O_3 and some of their mixtures have been used in post-deposition processing sequences in an attempt to improve the properties of deposited hafnium oxide films. Few studies have been reported that invoke chemical vapor deposition processes with different oxidants, even though the specific oxidant is one of the primary factors that establishes the properties of deposited films. The goal of this thesis is to investigate the effects of different oxidants on the structure and properties of deposited hafnium oxide films and improve the understanding of the fundamental relationships between oxidant, film structures and film properties. In addition, to the author's knowledge, no studies have been reported on the use of liquid injection for HfO_2-based films. If improved fundamental understanding of these processes is obtained, novel chemical vapor deposition and plasma-enhanced chemical vapor deposition technologies may be possible that can overcome some of the hurdles of hafnium oxide film introduction into sub-65 nm semiconductor manufacture. As a result, the objectives of the thesis include:

(1) Investigate the effects of different oxidants (O_2, N_2O, plasma dissociated O_2, plasma dissociated O_2/He, plasma dissociated N_2O, plasma dissociated N_2O/N_2)

on the structure and electrical properties of hafnium oxide films. Establish the role of oxygen atoms in film deposition and film properties, and propose a mechanism for chemical vapor deposition in different oxidants. Advance the understanding of the relationship between the structures and properties of the deposited films. Investigate the structures associated with some of the defects and the propose methods to improve the film quality.

(2) Based on the results of the fundamental study, develop metal-organic chemical vapor deposition (MOCVD) and downstream microwave plasma enhanced chemical vapor deposition (PECVD) technologies for HfO_2 or HfO_xN_y film depositions to improve their physical and electrical properties.

(3) Engineer the introduction of nitrogen atoms into hafnium oxide films by developing appropriate MOCVD/PECVD techniques. Investigate the role of nitrogen atoms and the effect of nitrogen location and bonding structures in hafnium oxynitride films.

REFERENCE

1. Hori, T., *Gate dielectrics and MOS ULSIs: principles, technologies, and applications*. 1997: Springer.
2. Sarace, J.C., Kerwin, R. E., Klein, D. L., and Edwards, R., Solid-State Electron., 1968. **11**: p. 653.
3. Prabhakaran, K. and T. Ogino, Surf. Sci., 1995. **325**: p. 263.
4. Moore, G.E., Electron. Mag., 1965. **38**: p. 114.
5. *Wikipedia the free encyclopedia*.
6. *International Technology Roadmap for Semiconductor (ITRS)*. 2004, Semiconductor Industry Association.
7. Buchanan, D., IBM J. Res. Dev., 1999. **43**: p. 245.
8. Green, M.L., Sorsch, T. W., Timp, G. L., Muller, D. A., Weir, B. E., Silverman, P. J., Moccio, S. V., and Kim, Y. O., Microelectron. Eng., 1999. **48**: p. 25.
9. Green, M.L., Gusev, E. P., Degraeve, R., and Garfunkel, E. L., J. Appl. Phys., 2001. **90**: p. 2057.
10. Braun, A.E., in *Semiconductor International*. 2005. p. 19.
11. Brown, G.A., Zeitzoff, P. M., Bersuker, G., and Huff, H. R., *Materials Today*. 2004. **7**: p. 20.
12. Robertson, J., Eur. Phys. J. Appl. Phys., 2004. **28**: p. 265.
13. Bersuker, G., Zeitzoff, P., Brown, G., and Huff, H. R., *Materials Today*. 2004. **7**: p. 26.
14. Engman, R., *The Jahn-Teller Effect in Molecules and Crystals*. 1972: Wiley-Interscience.

15. Sze, S.M., *Physics of Semiconductor Devices*. 1981: Wiley-Interscience.

16. Monch, W., Phys. Rev. Lett., 1987. **58**: p. 1260.

17. Robertson, J., J. Vac. Sci. Technol. B, 2000. **18**: p. 1785.

18. Klein, T.M., Niu, D., Epling, W. S., Li, W., Maher, D. M., Hobbs, C. C., Hedge, R. I., Baumvol, I., and Parsons, G. N., Appl. Phys. Lett., 1999. **75**: p. 4001.

19. Gusev, E.P., Copel, M., Cartier, E., Baumvol, I., Krug, C., and Gribelyuk, M. A., Appl. Phys. Lett., 2000. **76**: p. 176.

20. Chin, A., Liao, C. C., Liu, C. H., Chen, W. J., and Tsai, C., Tech. Dig. VLSI Symp., 1999: p. 135.

21. Buchanan, D.A., Gusev, E.P., Cartier, E., and Guha, S., Tech. Dig. Int. Electron Devices Meet., 2000: p. 223.

22. Libsch, F.R. and M.H. White, Solid-State Electron., 1990. **33**: p. 105.

23. Campbell, S.A., Gilma, D. C., Wang, X., Hsich, M. T., Kim, H. S., Gladfelter, W. L., and Yan, Y. H, IEEE Trans. Electron Devices, 1997. **44**: p. 104.

24. Ma, Y., Y. Ono, and S.T. Hsu, Mater. Res. Soc. Symp. Proc., 1999. **567**: p. 355.

25. Copel, M., M. Gribelyuk, and E. Gusev, Appl. Phys. Lett., 2000. **76**: p. 436.

26. Wilk, G., Green, M., Ho, M. Y., Busch, B., Sorsch, T., Klemens, F., Brijs, B., Van Dover, R., Kornblit, A., Gustafsson, T., Garfunkel, E., Hillenius, S., Monroe, D., Kalavade, P., and Hergenrother, J., Tech. Dig. Symp. VLSI Tech., 2002: p. 88.

27. Nigro, R.L., Raineri, V., Bongiorno, C., Toro, R., Malandrino, G., and Fragala, I. L., Appl. Phys. Lett., 2003. **83**: p. 129.

28. Aspinall, H.C., Gaskell, J., Williams, P. A., Jones, A. C., Chalker, P. R., Marshall, P. A., Smith, L. M., and Critchlow, G. W., Chem. Vap. Deposition, 2004. **10**: p. 83.

29. Maria, J.P., Wichasana, D., Kingon, A. I., Busch, B., Schulte, H., Garfunkel, E., and Gustafson, T., J. Appl. Phys., 2001. **90**: p. 3476.

30. Qi, W.J., Nieh, R., Lee, B. H., Onishi,K., Kang, L., Jeon, Y., Lee, J. C., Kaushik, V., Nguyen, B. Y., and Prabhu, L., Tech. Dig. VLSI Symp., 2000: p. 40.

31. Lee, C.H., Luan, H. F., Bai, W. P., Lee, S. J., Jeon, T. S., Senzaki, Y., Roberts, D., and Kwong, D. L., Tech. Dig. Int. Electron Devices Meet., 2000: p. 27.

32. Senzaki, Y., Alers, G., Hochberg, A., Roberts, D., Norman, J. T., Fleming, R., and Krautter, H., Electrochem. Solid State Lett., 2000. **3**: p. 435.

33. Mays, E.L., D.W. Hess, and W.S.R. Jr., J. Crystal Growth, 2004. **261**: p. 309.

34. Neumeyer, D.A. and E. Cartier, J. Appl. Phys., 2001. **90**: p. 1801.

35. Ramanathan, S., McIntyre, P. C., Luning, J., Lysaght, P. S., Yang, Y., Chen, Z., Stemmer, S., J. Electrochem. Soc., 2003. **150**: p. F173.

36. Choi, C.H., Jeon, T. S., Clark, R., and Kwong, D. L., IEEE Electro. Dev. Lett., 2003. **24**: p. 215.

37. Hendrix, B.C., Borovik, A. S., Xu, C., Roeder, J. F., Baum, T. H., Bevan, M. J., Visokay, M. R., Chambers, J. J., Rotondaro, A. L. P., Bu, H., and Colombo, L., Appl. Phys. Lett., 2002. **80**: p. 2362.

38. Zhao, C., Van Elshochtet, S., Conard, T., Xu, Z., Richard, O., Caymax, M., De Gendt, S., and Heyns, M., in *Proceedings - Electrochemical Society*. 2004.

39. in *EE Times*. 2005. p. April 25.

40. Wallace, R.M., Appl. Surf. Sci., 2004. **231-232**: p. 543.

41. Lucovsky, G., J. Vac. Sci. Technol. A, 2001. **19**: p. 1553.

42. Foster, A.S., Phys. Rev. B, 2001. **64**: p. 224108.

43. Warren, W.L., IEEE Trans. Nuclear Science, 1996. **43**: p. 2617.

44. Bastos, K.P., Morais, J., Miotti, L., Soares, G.V., Pezzi, R.P., Silva, R.C.G.d., Boudinov, H., Baumvol, I.J.R., Hegde, R.I., Tseng, H.H., and Tobin, P.J., J. Electrochem. Soc., 2004. **151**: p. F153.

45. Petry, J., Richard, O., Vandervorst, W., Conard, T., Chen, J., and Cosnier, V., J. Vac. Sci. Technol. A, 2003. **21**: p. 1482.

46. Wang, J.C., Hung, Y.P., Lee, C.L., and Lei, T.F., J. Electrochem. Soc., 2004. **151**: p. F17.

47. Kim, I., Han, S.K., and Osburn, C.M., J. Electrochem. Soc., 2004. **151**: p. F22.

CHAPTER 2

METALORGANIC CHEMICAL VAPOR DEPOSITION (MOCVD) AND PLASMA ENHANCED CHEMICAL VAPOR DEPOSITION (PECVD)

Chemical Vapor Deposition (CVD)

Chemical vapor deposition (CVD), which is a simple but yet versatile technique, is an essential process in the fabrication of ULSI devices and circuits [1-4]. Chemical vapor deposition is a process to synthesize thin solid films from gas phase reactants by a chemical reaction. The CVD process can produce thin films with reproducible and controllable and reproducible properties such as uniformity, purity, adhesion, surface morphology and microstructure. Although the CVD process may appear to be a simple technique, the basic chemistry behind this approach to film deposition is still unclear for most materials. Commonly, it is believed that the process consists of several complicated individual process steps that are summarized below and illustrated in Figure 2.1 [5]:

(1) Mass transport of the reactant gases from the gas inlet to the reaction zone, where the reaction zone is a narrow region close to the surface of the heated substrates;

(2) Gas phase reactions in the reaction zone that lead to the formation of film precursors;

(3) Mass transport the film precursors to the growth surface;

(4) Adsorption of the film precursors onto the growth surface;

(5) Surface diffusion of the precursors to the growth sites;

(6) Reaction of precursors at the surface and film growth on the substrates;

(7) Desorption of the by-products of surface reactions;

(8) Mass transport of by-products from the reaction zone to the main gas flow that exhausts from the reactor.

Each step in the process must be controlled so that the deposited films have the desired properties.

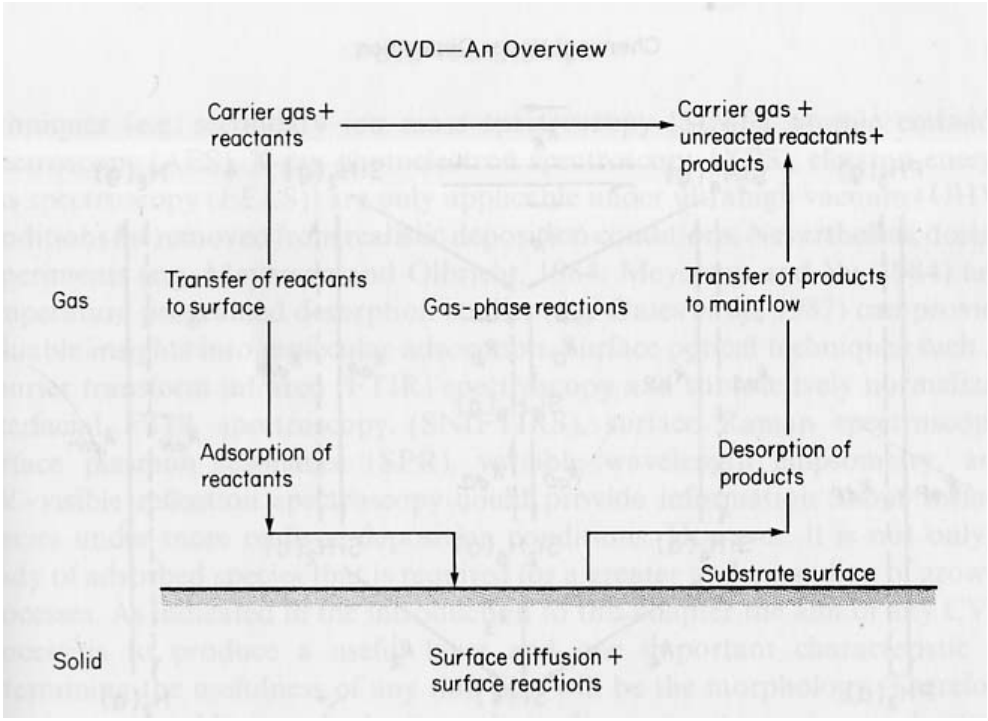

Figure 2.1 Basic steps of CVD processes [5].

CVD Apparatus

For various thin film applications, CVD reactor configurations are different. However, in general, a CVD system consists of three components: a reagent handling arrangement for the source or reactant compounds, a reactor chamber and an exhaust system.

Film Precursors and Gas Handling System

Film precursors for CVD reaction systems may be gaseous, liquid or solid sources. Gaseous sources are fed into the reactor chamber from a high-pressure gas cylinder, sometimes mixing with other gases before flowing into the chamber. For solid and liquid precursors, a carrier gas is needed to flow through precursor containers and carry the precursor vapor into the reactor chamber. The amount of introduced film precursor is controlled by the temperature of the source container, the pressure in the container, precursor vapor pressure and carrier gas flow rate. After equilibrium is established in the precursor container, the film precursor flow rate can be calculated from [6]:

$$F = F_{carriergas} P/(P_{total} - P) \qquad (2.1)$$

where $F_{carrier\ gas}$ is the flow rate of the carrier gas, P is the partial pressure of the precursor, and P_{total} is the total pressure in the precursor container.

In metalorganic chemical vapor deposition (MOCVD), organometallic compounds with high vapor pressure are used as precursors. For these compounds, safety and environmental concerns are important issues; specific information on gas handling and safety of MOCVD systems is available [7]. Typically, additional reactant gases such as O_2, N_2, H_2, or NH_3 flow into the reactor chamber through separate gas lines outfitted with gas flow controllers.

Chamber

Film deposition occurs in the CVD chamber, so the chamber configuration can have a significant influence on the physical and chemical properties of the deposited films. A variety of CVD chamber configurations are used for different films; a few basic configurations are given in Figure 2.2 [6].

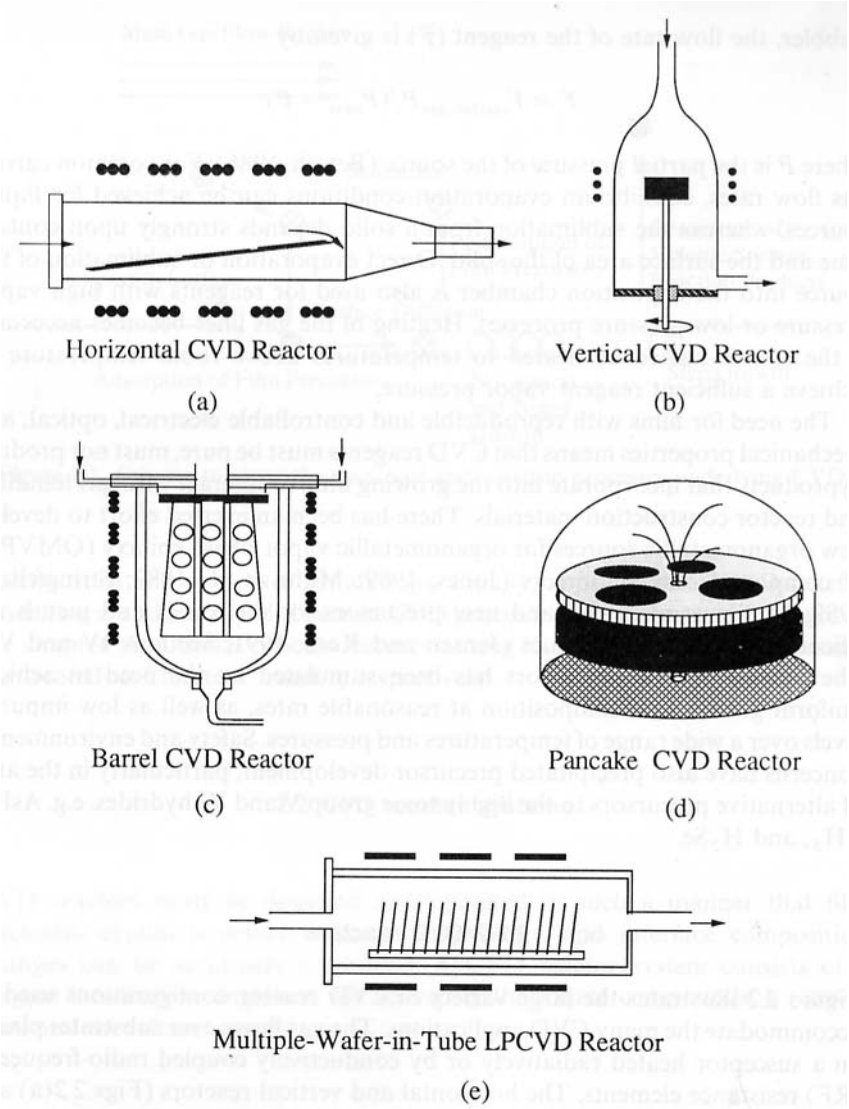

Figure 2.2 Basis configurations of CVD reactors [6].

The horizontal (Figure 2.2a) and vertical (Figure 2.2b) chambers are typically used to grow compound semiconductors by metalorganic chemical vapor deposition (MOCVD); these can be used for atmospheric pressure or low pressures deposition. A barrel configuration (Figure 2.2c) can process multiple wafers at the same time and it is commonly used for epitaxial (silicon) growth. In the pancake reactor (Figure 2.2d), the

walls are usually cooled, or at least not heated, to avoid chamber contamination by deposition on the walls and subsequent production of particulates due to flaking. Low pressure CVD is the typical reactor type used for dielectric and passivating film deposition in microelectronic device and integrated circuit fabrication [8]. Figure 2.2e shows a traditional horizontal multiple-wafer-in-tube LPCVD chamber. At low pressures, the diffusion coefficient of precursor molecules is high so that the deposition rate is determined by the surface reaction rate rather than the precursor diffusion rate to the surfaces; thus, multiple wafers can be uniformly coated simultaneously.

Exhaust System

The byproducts of CVD processes may be hazardous and toxic and therefore cannot be vented to the atmosphere directly. Rather, the gaseous byproducts and un-completely decomposed precursors need to be trapped by chemical or physical methods that include wet chemical scrubbers, dry absorption and pyrolysis. Also, pumps and throttle valves are used to control the pressure of the reactor. Exhaust systems for CVD reactors consist of all these units.

MOCVD System Used in This Thesis

The CVD system used for the studies in this thesis is a custom-designed MOCVD reactor that was built by a former group member - Dr. Ebony L. Mays [9]; a schematic illustration of the system is shown in Figure 2.3. The primary segments of the system are described in the following sections.

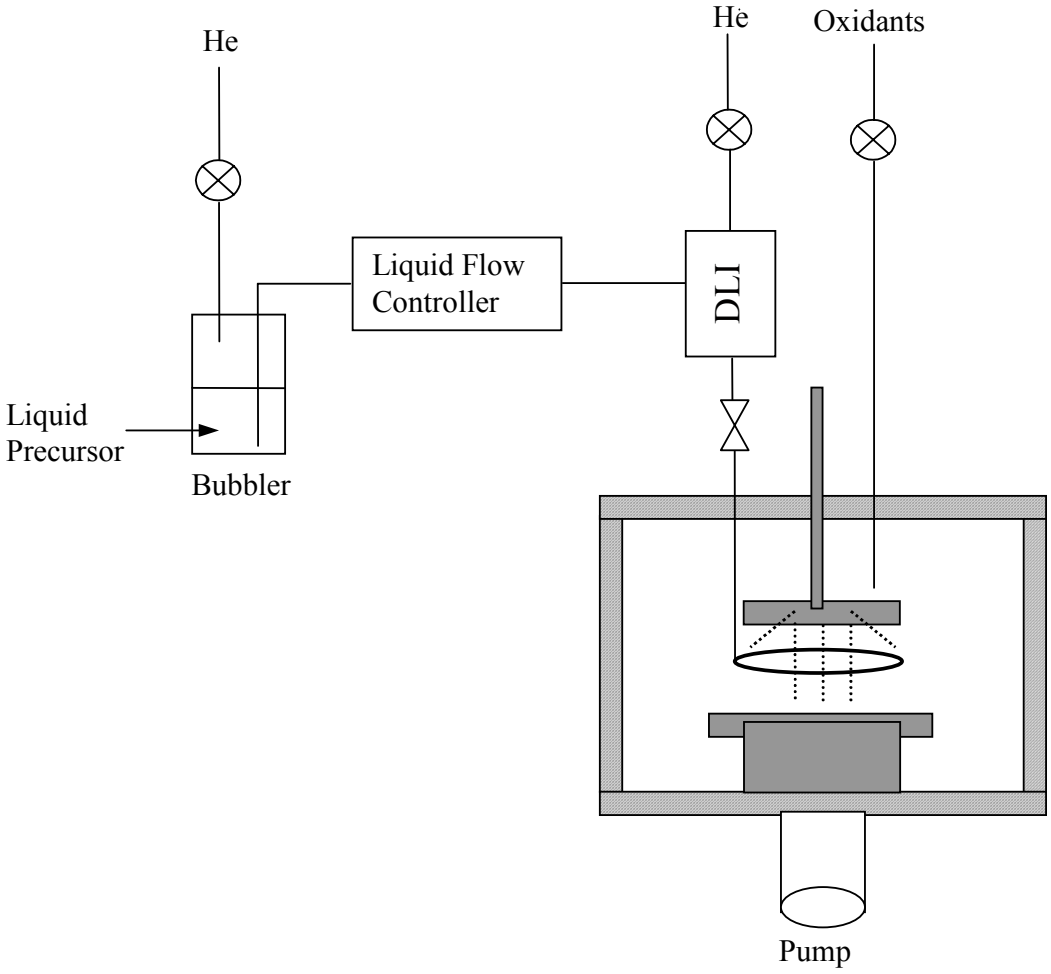

Figure 2.3 Schematic illustration of the MOCVD system with DLI system used for the studies in this thesis.

Precursor and Direct Liquid Injection (DLI) System

In order to obtain uniform growth of high-k hafnium oxynitride films with reproducible physical and chemical properties by MOCVD, the precursors used for film deposition must be pure, highly volatile, stable in containers and gas lines, and have few byproducts that could contaminate the deposited films. A large number of studies have been performed using various hafnium-containing organometallic compounds; vapor

pressures and decomposition temperatures of these precursors are summarized in Table 2.1.

Table 2.1 Precursors previously used for hafnium oxide deposition along with their general properties.

Precursor	Deposition temperature (°C)	Volatility	References
$HfCl_4$	> 800	Low volatility solid	[10, 11]
$Hf(NO_3)_4$	450	Low volatility solid	[12, 13]
$Hf(O^tC_4H_9)_4$	315 - 450	1 torr at 65 °C	[14-17]
$Hf(NC_2H_5)_4$	300 - 600	1 torr at 80 °C	[18-22]
$Hf(OCH_2CH_2NMe_2)_4$	150	4.5 torr at 80 °C	[23]
$Hf(CH_3COCHCOCH_3)_4$	350	Evaporate at 200 °C	[24]
$Hf(OCMe_2CH_2OMe)_4$	350 - 600	Evaporate at 130 °C	[25]

Based on the data in Table 2.1, it is evident that hafnium tetrakis-diethylamide (TDEAH) has a high vapor pressure at low temperature and a relatively low decomposition temperature. Since TDEAH is a commercially available precursor, this is a suitable precursor for the studies to be performed in this thesis. Some chemical and physical studies have been performed on the TDEAH precursor purchased from Epichem Inc and results are discussed below.

Thermogravimetric Analysis (TGA)

TGA measurements are performed on a Perkin Elmer TGA 7 that is kept in a glove box. The TGA furnace is purged with ultrahigh purity argon gas so that analyses are performed in an argon atmosphere; the argon flow rate is maintained at 20 ml/min. For each run, ~20 mg of liquid precursor compound is placed in the platinum sample pan by a micro-liter syringe. TGA curves are collected by ramping the furnace to 350 °C at the speed of 10 °C/min.

The TGA curve of the TDEAH precursor is shown in Figure 2.4. Clearly, the precursor begins to lose weight at ~90 °C. Because 90 °C is lower than the decomposition temperature of TDEAH, the weight loss at low temperature can be attributed to precursor evaporation. All material is evaporated or decomposed when the temperature reaches ~250 °C and the mass of residue is about 10 % of the precursor. The residue is thus composed of decomposition products of TDEAH. These TGA results demonstrate that the precursor can be evaporated at temperatures above 90 °C.

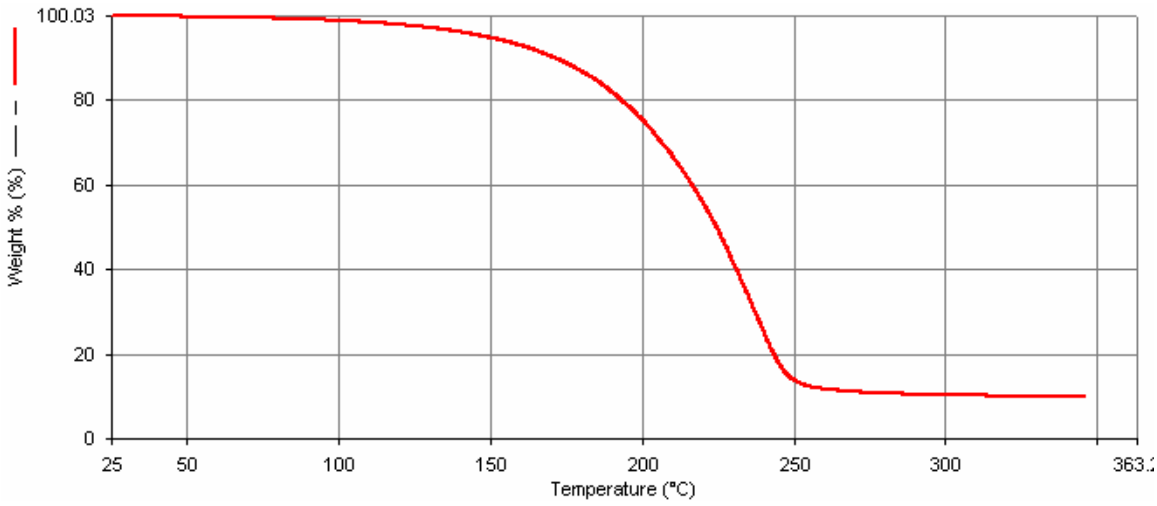

Figure 2.4 TGA curve of the liquid precursor TDEAH. The furnace atmosphere is Ar and the temperature ramping speed is 10 °C/min.

Viscosity Analysis

In order to establish if TDEAH is suitable for direct liquid injection (DLI) MOCVD, the viscosities of TDEAH are measured in the temperature range of 40 – 100 °C. The measurement is performed on a Cambridge Instrument Viscolab 2000 Viscometer enclosed in a glove box. Before measurement, the viscometer is calibrated by using standard fluids from Cambridge Applied Systems Inc. The viscometer result is determined by the average of ten data points.

The viscosities of TDEAH and the dependence of viscosity on temperature are shown in Table 2.2 and Figure 2.5. At low temperatures, the precursor is a viscous liquid with viscosity ~5 cP; with increasing temperature, the viscosity of the precursor decreases significantly. At 95 °C, which is the working temperature for the evaporator of the DLI system, the viscosity of the precursor is 1.935 cP. The low viscosity of TDEAH at high temperatures confirms that the precursor can be easily handled in the DLI system.

Table 2.2 Viscosities of precursor TDEAH in the temperature range of 40 – 100 °C.

Temp. °C	40.2	45.1	50.0	55.0	60.0	65.0	70.0
Visc. (cP)	5.419	5.055	4.612	3.918	3.762	3.359	3.367
Temp. °C	75.0	80.1	85.0	90.0	95.0	100.0	
Visc. (cP)	2.903	2.605	2.306	2.122	1.935	1.71	

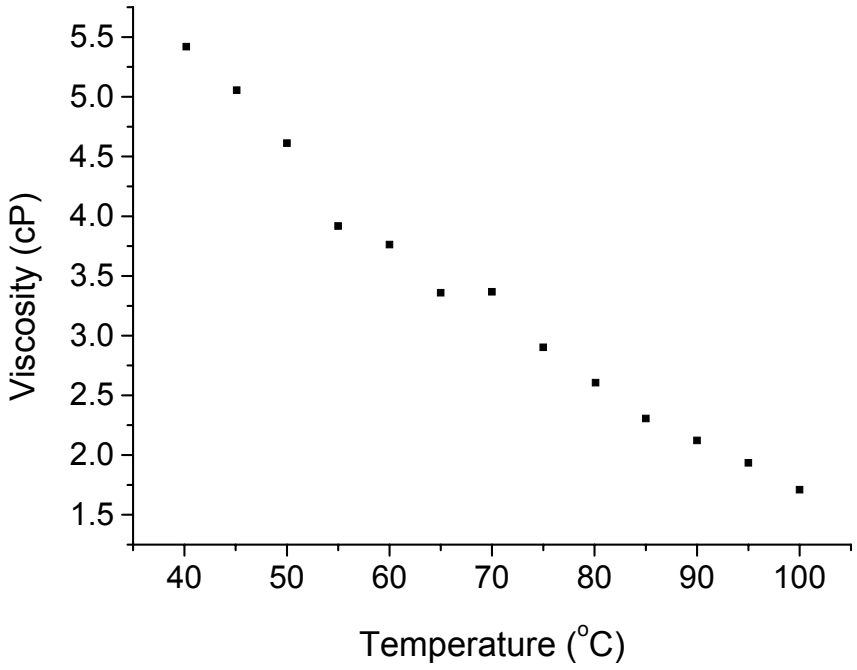

Figure 2.5 Viscosity curve of the precursor TDEAH.

Direct Liquid Injection (DLI) System

A DLI system, manufactured by Bronkhorst, is used to avoid the effects of precursor container temperature and precursor volume on the amount of precursor introduced precursor introduced into the deposition chamber. As shown in Figure 2.3, the DLI system consists of a liquid flow controller, a mass flow controller for carrier gas and a temperature controlled mixing and evaporation device. Liquid precursor is pressed into the mixing valve by helium gas and mixed with He carrier gas before being evaporated and delivered into the deposition chamber. To avoid condensation of the evaporated precursor onto the walls of the delivery tubing before it enters the chamber, the tubing is heated by heating tapes to a temperature 10 °C higher than the evaporator temperature.

Based on TGA analysis, viscosity measurement and the decomposition temperature of TDEAH (300 °C), the evaporator temperature is set at 95 °C and the tubing is heated to 105 °C. At these temperatures, TDEAH can be evaporated readily and delivered into the deposition chamber without decomposition.

Chamber and Exhaust System

The chamber and the exhaust unit of the MOCVD system used in this thesis have been described in a previous thesis [8]. During depositions, the chamber is heated to 60 °C to minimize precursor condensation on the chamber wall. The exhaust system consists of a throttle valve and an Alcatel 2063C2 pump so that the pressure of the system can be controlled independent of the flow rate. A wet chemical scrubber is linked to the pump exhaust to remove undecomposed organometallic precursor. To keep the organometallic compound from being dissolved in pump oil, nitrogen gases bubble up through the oil during deposition.

Plasma Enhanced Chemical Vapor Deposition (PECVD)

Fundamentals of PECVD

To permit the deposition of films onto polymer substrates, to control film morphologies, and to generally reduce thermal budgets it is often necessary to deposit films at low temperatures (< 350 °C). Plasma-enhanced chemical vapor deposition (PECVD) in radio frequency (rf) or microwave discharges has been widely used to achieve such goals, including the deposition of high-k materials [26-31]. In PECVD, most of energy needed for breaking bonds is supplied by the high-energy electrons in a plasma instead of by thermal energy in MOCVD.

The fundamental physics and chemistry of rf or microwave plasmas have been extensively described [32, 33]. The complex chemical reactions in a plasma include two types of processes: homogeneous gas-phase collisions and heterogeneous surface interactions.

Reactive free radicals, metastable species, and ions in plasmas are generated by gas-phase collisions. Electron impact reactions are primarily responsible for reactive species, ion, and electron generation; examples of electron impact reactions are listed in Table 2.3 [34]. Dissociation and excitation reactions indicated at the top of the table require the lowest energies. For ionization reactions, electrons with energy >8 eV are required. Because high-energy electrons are in the tail of the electron energy distribution achieved in these plasmas, few electrons have the required energy. Thus, excitation and dissociation represent the primary gas-phase reactions and higher concentrations of neutral radicals relative to ions and electrons are present in such plasmas. In addition, gas phase collisions occur between heavy particles, especially in gases such as He and Ar due to the existence of metastable species. Possible collision reactions are listed in Table 2.4 [35].

Table 2.3 Examples of electron impact reactions in plasma [34].

Excitation (rotational, vibrational, electronic)	$e + X_2 = X_2^* + e$
Dissociative attachment	$e + X_2 = X^- + X^+ + e$
Dissociation	$e + X_2 = 2X + e$
Ionization	$e + X_2 = X_2^+ + 2e$
Dissociative ionization	$e + X_2 = X + X^+ + 2e$

Table 2.4 Possible reactions due to heavy particle collisions [35].

Penning dissociation	$M^* + X_2 = 2X + M$
Penning ionization	$M^* + X_2 = X_2^+ + M + e$
Charge transfer	$M^+ + X_2 = X_2^+ + M$ $M^- + X_2 = X_2^- + M$
Collisional detachment	$M + X_2^- = X_2 + M + e$
Associative detachment	$X^- + X = X_2 + e$
Ion – ion recombination	$M^- + X_2^+ = X_2 + M$ $M^- + X_2^+ = 2X + M$
Electron – ion recombination	$e^- + X_2^+ = 2X$ $e^- + X_2^+ + M = X_2 + M$
Atom recombination	$2X + M = X_2 + M$
Atom abstraction	$A + BC = AB + C$
Atom addition	$A + BC + M = ABC + M$

The energetic radicals, ions and electrons produced by plasmas have significant effects on film deposition processes and structures of films. Various heterogeneous processes occur on substrate surfaces in PECVD; the generic elementary heterogeneous processes possible are shown in Table 2.5 [36]. Energetic particle bombardment plays an important role in these surface reactions. Although particle bombardment results in a number of advantages for thin film deposition, such as generating nucleation sites, increasing the film density, breaking bonds in film precursors which enhances reaction

rates, and controlling film stress, high-energy particles also may increase the defects in films and damage surfaces. Thus, careful design of reactor configurations and parameter optimization are required in PECVD processes.

Table 2.5 Elementary heterogeneous processes at surfaces in plasma [36].

1. Ion – surface interactions a. neutralization and secondary electron emission b. sputtering c. ion – induced chemistry
2. Electron – surface interactions a. secondary electron emission b. electron – induced chemistry
3. Radical – surface or atom – surface interactions a. surface etching b. film deposition

An overall PECVD process can be divided into several primary steps analogous to those in MOCVD process:

(1) Generation of reactant species in plasma gas-phase reactions

(2) Diffusion of film precursors and plasma produced reactant species to a deposition zone near the substrate surface

(3) Adsorption of reactant species onto the substrate surface

(4) Reaction at the substrate surface

(5) Desorption of byproducts from deposited films

(6) Byproduct diffusion way from deposition zone

Similar to MOCVD reactors, PECVD reactors consist of several basic components: precursor and gas handling, chamber and exhaust system. The primary difference is that a PECVD reactor needs a power supply to create the discharge. Several examples of PECVD configurations are shown in the Figure 2.6 [37]. Capacitively coupled parallel plate reactors (Figure 2.6a) are usually used for low temperature depositions. In this configuration, the substrate and deposited films are immersed in the discharge and directly exposed to particle bombardment. Inductively coupled reactors (Figure 2.6 b, c) and ECR reactors (Figure 2.6 d) can be used at relatively high temperatures. These configurations provide more control of the specific plasma chemistry since byproducts are not exposed to the discharge atmosphere.

PECVD Reactor Used in This Thesis

The downstream microwave PECVD reactor used for the studies in this thesis is a modification of the MOCVD system described earlier in this chapter; a schematic illustration of the PECVD system is shown in Figure 2.7. In this modification, an upstream microwave plasma source is added to the MOCVD system. As indicated by the figure, reactant gases flow through the plasma applicator that is connected to a microwave generator, prior to being introduced into the deposition chamber. The pressure in the deposition chamber is maintained between 1 and 2 torr during depositions. Microwave power is generated by a Astex AX2115 power generator and transferred in a wave-guide channel to the Astex AX7610-4 applicator through an Astex AX3060 smartmatch microwave impedance matching unit. Microwave energy is coupled to the

flowing gas through the wall of a dielectric tube in the applicator and the smartmatch adjusts automatically to maximize the energy coupling efficiency. Thus, a plasma is produced in the dielectric tube. The outlet of the downstream plasma applicator is connected to a port on the side of the deposition chamber through a 90° bend so that essentially all of the ions and electrons produced by the plasma recombine by collisions with each other or on the tube walls. With this design, the reactant gases introduced into the reactor chamber comprise only energetic neutral species and the deposited high-k films are not exposed to charging induced by ions and electrons.

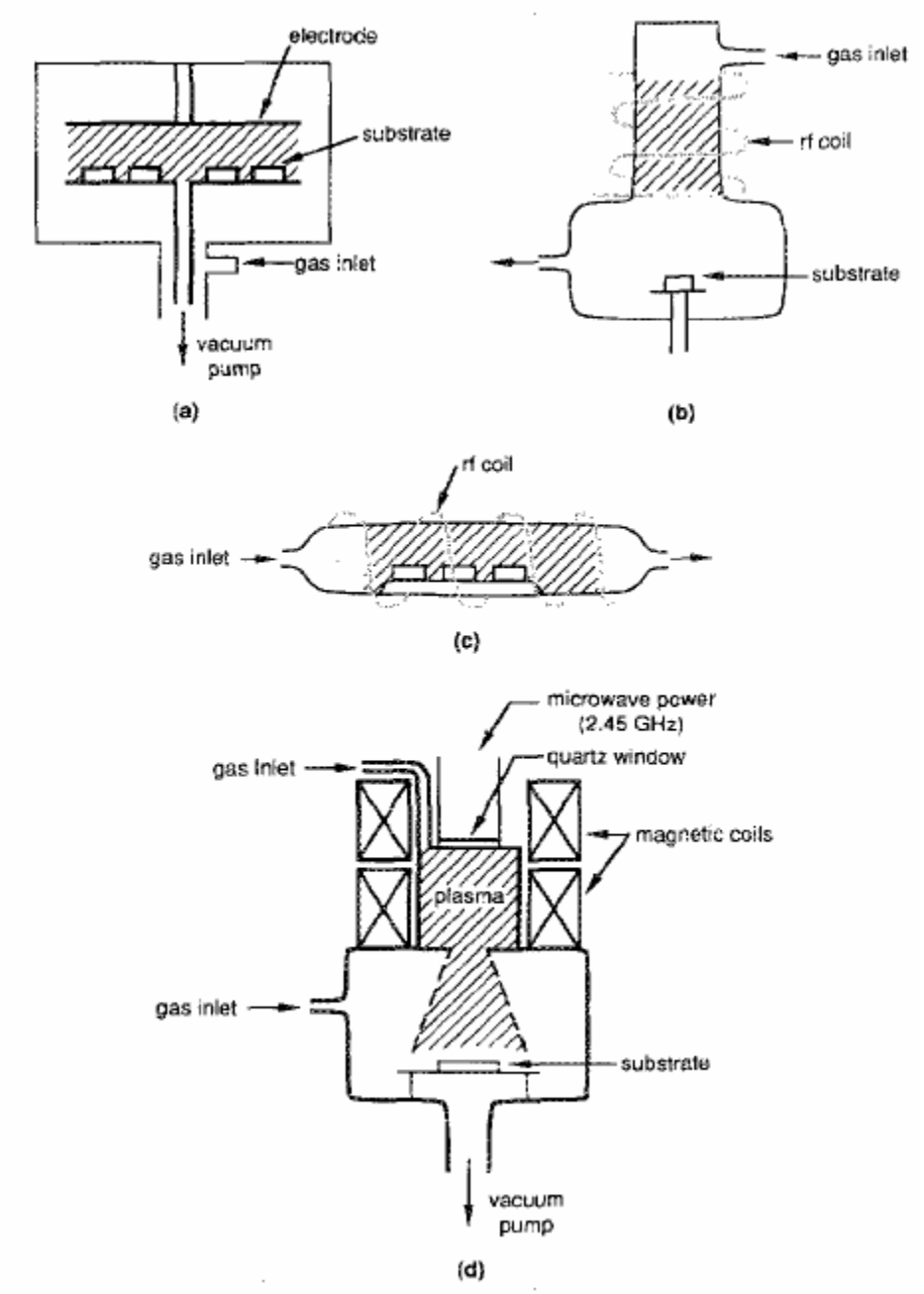

Figure 2.6 Various configurations of PECVD reactors [37].

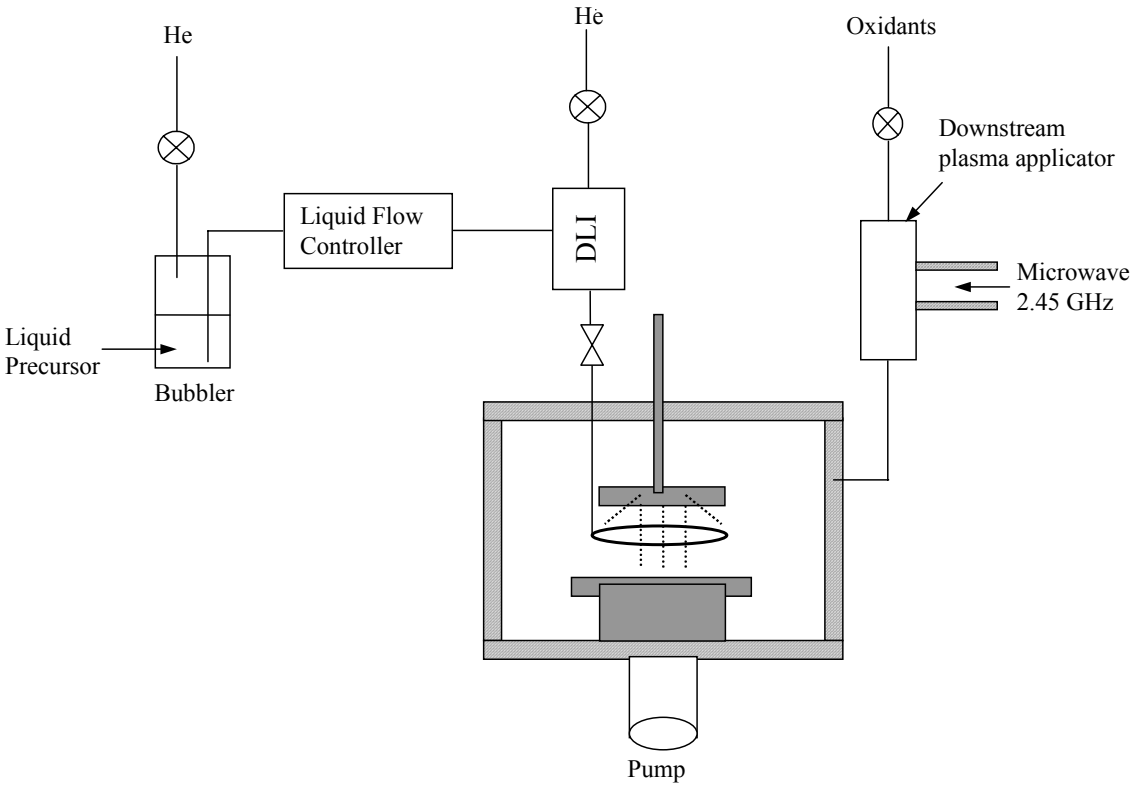

Figure 2.7 Schematic illustration of the PECVD system used in this thesis.

REFERENCE

1. Sherman, A., *Chemical vapor deposition for microelectronics: principles, technology, and applications*. 1987, Mill Road, NJ: Noyes Publications.
2. Cote, D.R., Nguyen, S.V., Cote, W.J., Pennington, S.L., Stamper, A.K., and Podlesnik, D.V., IBM Journal of Research and Development, 1995. **39:** p. 837.
3. Bean, K.E., Thin Solid Films, 1981. **83**: p. 173.
4. Rees, W.S., *CVD of nonmetals*. 1996, New York: VCH.
5. Jensen, K.F. and Kern, W., *Thin film process II*, ed. J. Vossen and W. Kern. 1991, Orlando, FL: Academic Press.
6. Jensen, K.F., *Chemical vapor deposition: principles and applications*, ed. M.L. Hitchman and K.F. Jensen. 1993, San Diego, CA: Academic Press Inc.
7. Stringfellow, G.B., J. Crystal Growth, 1986. p. **77**.
8. Adams, A.C., *VLSI Technology*, ed. S.M. Sze. 1983, Princeton, NJ: McGraw-Hill.
9. Mays, E.L., *Chemical vapor deposition and characterization of zirconium tin titanate as a high dielectric constant material for potential electronic applications*, in *Materials Science and Engineering*. 2003, Georgia Institute of Technology: Atlanta.
10. Powell, C.F., *Vapor Deposition*, ed. C.F. Powell, J.H. Oxley, and J.M. Blocher. 1966, New York: John Wiley & Sons, Inc.
11. Ritala, M., Kukli, K., Rahtu, A., Raisanen, P.I., Leskala, M., Sajavaara, T., and Keinonen, J., Science, 2000. **288**: p. 319.
12. Conley, J.F., Ono, Y., Tweet, D.J., and Solanki, R., Appl. Phys. Lett., 2004. **84**: p. 398.

13. Park, J., Park, B.K., Cho, M., Hwang, C.S., Oh, K., and Yang, D.Y., J. Electrochem. Soc., 2002. **149**: p. G89.

14. O'Sullivan, B.J., Hurley, P.K., O'Conner, E., Modreanu, M., Roussel, H., Jimenez, C., Dubourdieu, C., Audier, M., and Senateur, J.P., J. Electrochem. Soc., 2004. **2004**: p. G493.

15. Sayan, S., Aravamudhan, S., Busch, B.W., Schulte, W.H., Cosandey, F., Wilk, G.D., Gustafsson, T., and Garfunkel, E., J. Vac. Sci. Technol. A, 2002. **20**: p. 507.

16. Frank, M.M., Sayan, S., Dormann, S., Emge, T.J., Wielunski, L.S., Garfunkel, E., and Chabal, Y.J., Mater. Sci. Eng. B, 2004. **109**: p. 6.

17. Triyoso, D.H., Ramon, M., Hegde, R.I., Roan, D., Garcia, R., Baker, J., Wang, X.D., Fejes, P., B. E. White, J., and Tobin, P.J., J. Electrochem. Soc., 2005. **152**: p. G203.

18. Takahashi, K., Funakubo, H., Hino, S., Nakayama, M., Ohashi, N., Kiguchi, T., and Tokumitsu, E., J. Mater. Res., 2004. **19**: p. 584.

19. Ohshita, Y., Ogura, A., Hoshino, A., Hiiro, S., Suzuki, T., and Machida, H., Thin Solid Films, 2002. **406**: p. 215.

20. O'Connor, R., Hughes, G., Degraeve, R., Kaczer, B., and Kauerauf, T., Semicond. Sci. Technol., 2005. **20**: p. 68.

21. Schaeffer, J., Edwards, N.V., Liu, R., Roan, D., Hradsky, B., Gregory, R., Kulik, J., Duda, E., Contreras, L., Christiansen, J., Zollner, S., Tobin, P., Nguyen, B.Y., Nieh, R., Ramon, M., Rao, R., Hegde, R., Rai, R., Baker, J., and Voight, S., J. Electrochem. Soc., 2003. **2003**: p. F67.

22. Hendrix, B.C., Borovik, A.S., Xu, C., Roeder, J.F., Baum, T.H., Bevan, M.J., Visokay, M.R., Chambers, J.J., Rotondaro, A.L.P., Bu, H., and Colombo, L., Appl. Phys. Lett., 2002. **80**: p. 2362.

23. Song, M.K., Kang, S.W., and Rhee, S.W., Thin Solid Films, 2004. **450**: p. 272.

24. Smith, R.C., Ma, T., Hoilien, N., Tsung, L.Y., Bevan, M.J., Colombo, L., Roberts, J., Campbell, S.A., and Gladfelter, W., Adv. Mater. Opt. Electron., 2000. **10**: p. 105.

25. Williams, P.A., Roberts, J.L., Jones, A.C., Chalker, P.R., Tobin, N.L., Bickley, J.F., Davies, H.O., Smith, L.M., and Leedham, T.J., Chem. Vap. Deposition, 2002. **8**: p. 163.

26. Hess, D.W., IBM Journal of Research and Development, 1999. **43**: p. 127.

27. Choi, K.J., Kim, J.H., Yoon, S.G., and Shin, W.C., J. Vac. Sci. Technol. B, 2004. **22**: p. 1755.

28. Choi, K.J., Kim, J.H., and Yoon, S.G., J. Electrochem. Soc., 2004. **151**: p. G262.

29. Chen, P., Bhandari, H.B., and Klein, T.M., Appl. Phys. Lett., 2004. **85**: p. 1574.

30. Maiti, C.K., Dalapati, G.K., Chatterjee, S., Samanta, S.K., Varma, S., and Patil, S., Solid-State Electronics, 2004. **48**: p. 2235.

31. Zenasni, A., Raynaud, P., Sahli, S., Rebiai, S., and Segui, Y., Surface and Coatings Technology, 2003. **174-175**: p. 162.

32. Chapman, B.N., *Glow Discharge Processes*. 1980, New York: Wiley.

33. Sivaram, S., *Chemical vapor deposition: thermal and plasma deposition of electronic materials*. 1995, New York: Van Nostrand Reinhold.

34. Bell, A.T., Solid State Technol., 1978. **21**: p. 89.

35. Hess, D.W. and Graves, D.B., *Chemical vapor deposition: principles and applications*, ed. M.L. Hitchman and K.F. Jensen. 1993, San Diego, CA: Academic Press Inc.

36. Winters, H.F. *Plasma chemistry III*. in *Topics in current chemistry*. 1980. New York: Springer - Verlag.

37. Hess, D.W., J. Vac. Sci. Technol. A, 1990. **8**: p. 1677.

CHAPTER 3

COMPARISON OF HAFNIUM OXYNITRIDE FILMS DEPOSITED IN O_2 AND N_2O MOCVD

Introduction

As elaborated in the chapter 1, when the minimum feature size in complementary metal-oxide-semiconductor (CMOS) devices drops below 65 nm, the gate dielectric thickness will fall below 1.5 nm [1]. For the current gate material SiO_2, the leakage current of a film <1.5 nm will increase sufficiently to impair device operation. Thus, high dielectric constant (high-k) materials are being investigated as replacements for SiO_2 in CMOS devices in order to reduce this leakage. Because the dielectric constants of high-k materials (usually $\varepsilon > 10$) are larger than that of SiO_2 ($\varepsilon = 3.9$), the high-k gate layer can be physically thicker than a capacitively equivalent SiO_2 gate layer ($t_{high\text{-}k}/\varepsilon_{high\text{-}k} = t_{SiO2}/\varepsilon_{SiO2}$); as a result, the leakage current is reduced. Recently, a number of binary and ternary metal oxides have been studied as candidates for new gate dielectrics, including Al_2O_3 [2], ZrO_2 [3], HfO_2 [4-6] and (Zr, Sn, Ti)O_2 [7, 8].

Because of its high dielectric constant (15-25), large bandgap (5.68 eV) and thermal stability with silicon, attention has focused on HfO_2 based high-k materials. It has been demonstrated that HfO_2 is a promising gate dielectric material, although some limitations remain, such as inadequate barrier for contaminates, insufficient thermal stability and limited quality of the interface layer between HfO_2 and the silicon substrate. Recent studies have indicated that hafnium oxynitride films offer improved barrier properties, thermal stability and electrical performance relative to hafnium oxide films [9,

10]. Nitrided hafnium oxide layers have been obtained by ammonia annealing of deposited HfO_2 films [11], by the use of amide precursors (e.g., hafnium tetrakis-dimethylamide and hafnium tetrakis-diethylamide for deposition [12-16], or by incorporation of nitrogen-containing reactants such as NH_3 into CVD processes [17]. In addition, in order to improve the performance of hafnium based high-k films, post-deposition annealing is often used to reduce the defects in the films and interfaces. Usually, post-deposition annealing is performed in O_2 [18, 19], N_2 [20, 21], N_2/O_2 [22], forming gas [23, 24], deuterium [25] or NH_3 [11, 26]. But post-deposition annealing increases the complexity of microelectronic fabrication processes and facilities; it may also introduce other problems such as H contamination, EOT increase and crystallization by high-temperature annealing. Thus, thin film formation approaches with minimal limitations are desired in order to improve the performance of hafnium oxynitride films. Introduction of an oxidant other than O_2 into MOCVD processes may affect deposition rate, oxidation mechanism, and thus bonding and interfacial structures of as-deposited high-k films (i.e., without post-deposition annealing). At present, few reports exist concerning successful improvement of hafnium oxynitride films by changing the oxidizing environment during MOCVD. Previous investigations have shown that hafnium oxynitride films deposited using NO or N_2O at temperatures above 600 ºC contain higher N concentrations than films deposited with oxygen [27, 28]. However, the dielectric properties of nitrided HfO_2 films deposited from pure NO and N_2O have either not been reported [27], or have shown high electrical conductivity [28].

In the studies described in this chapter, nitrided HfO_2 films are deposited in a direct liquid injection MOCVD system with hafnium tetrakis-diethylamide (TDEAH) as

the precursor and N_2O as the oxidant. For comparison, O_2 is also used as an oxidant in this MOCVD system. The deposition temperatures range from 300 ºC to 410 ºC. Growth kinetics, bulk and interfacial film composition, morphology, and electrical properties of the films deposited from N_2O and O_2 are described and compared. To our knowledge, this work represents the first systematic study addressing the effects of oxidizing environment in hafnium oxynitride MOCVD.

Experimental

Film Deposition

All films were deposited on 4-inch p-type (100) silicon wafers with resistivity < 0.01 Ω/cm. Prior to deposition, silicon wafers were cleaned by a standard RCA sequence followed by a 30 sec dip in 1% HF solution. The RCA clean first invoked immersion in a 5:1:1 H_2O : 29 % NH_4OH : 30 % H_2O_2 solution for 5 min at 70-80 ^oC. After a de-ioinized (DI) water rinse and exposure to an aqueous 1 % HF solution for 30 sec, the wafers were immersed in a 6:1:1 H_2O : 30 % H_2O_2 : 37% HCl solution for 5-10 min at 70 ^oC. Following a rinse in DI water, the wafers were blown dry in nitrogen. Nitrided HfO_2 films were deposited in the direct liquid injection MOCVD system that is already described in detail in chapter 2. The hafnium precursor used for film deposition is hafnium tetrakis-diethylamide ($Hf(NC_2H_5)_4$, TDEAH). In a typical deposition, liquid precursor was transported to the evaporator with dry helium at a flow rate of 0.03 or 0.06 ml/min and evaporated at 95 ºC. The evaporated precursor was mixed with 200 sccm helium carrier gas and delivered to the reactor through a line heated to 105 ºC. Oxygen or nitrous oxide flowed into the chamber at the rate of 100 sccm through a separate line.

Reactor pressure was maintained at 2 Torr. Deposition temperatures ranged from 300 ºC to 410 ºC. Unless otherwise noted, the deposition time was 10 minutes.

Film Thickness Measurement

Film thickness was measured on a Woollam Variable Angle Spectroscopic Ellipsometer (VASE) with a spectral range from 700 nm to 1200 nm at an angle of 75°. Five spots on wafers were measured and averaged to yield the film thickness; locations of measured spots on wafers are shown in Figure 3.1.

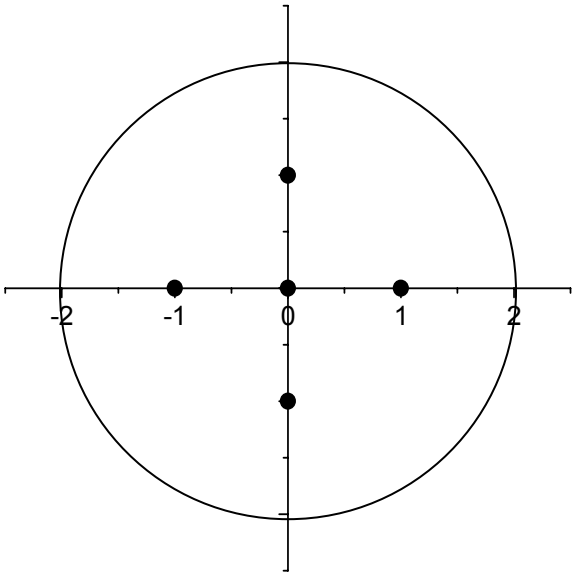

Figure 3.1 Locations of five measured spots on 4-inch wafers.

Composition and Interface Measurements

X-ray photoelectron spectroscopy (XPS) is currently one of the widely used surface analysis techniques. It can give information about composition and binding environment of surfaces.

As shown in Figure 3.2, in XPS measurements, the analyzed surface is irradiated by a monochromatic X-ray beam and a photon with energy of *hv* could interact with an electron in nucleus. After the electron obtains energy from photon, a photoelectron is ejected. The kinetic energy of the ejected electron (E_{KE}) can be expressed as:

$$E_{KE} = hv - E_B - \Phi_S \qquad (1)$$

Φ_S is the work function that is a small constant of the given spectrometer; E_B is the binding energy of the electron. The ejected electrons can come from core shells or from outer shells of nucleus. But in XPS, most attention is focused on electrons from core shells. Because the electronic binding energies for different elements are different, analyzing the kinetic energies of ejected photoelectrons can be used on elemental analysis. The concentrations of atoms giving out photoelectrons are estimated with considering the atomic mass, photoemission cross-section, electron attenuation length, and detection efficiency. The kinetic energies of photoelectrons are usually low so that their attenuation lengths are very short. Only electrons emitted from the surface area of materials can flow out of the surface and reach the detector, thus XPS can only provide the elemental information of top surface of films (about 7-10 nm). In addition, from equation (1), it shows that any change of binding energy will be reflected on the kinetic energy of photoelectrons. The change of bonding structure and environment of atoms leads to the shift of binding energy. Hence, based on the binding energy positions, the bonding structure of atoms can be analyzed.

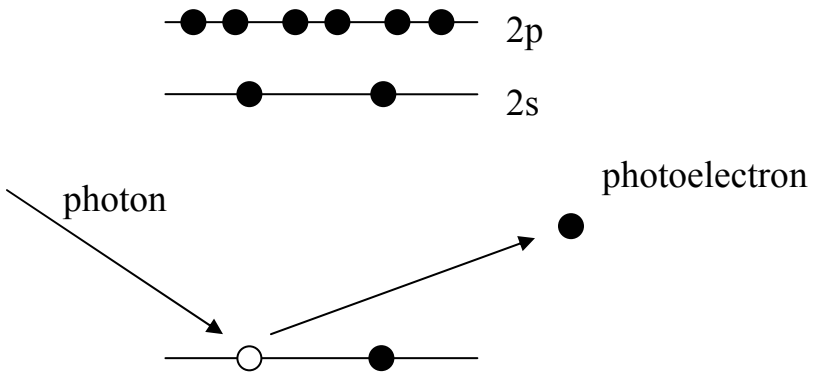

Figure 3.2 Schematic diagram of photoelectron emission processes.

Composition measurements of the films were performed on a PHI 1600/3057 X-ray Photoelectron Spectrometer (XPS) with a standard aluminum x-ray source. Typically, 60 seconds of sputtering was performed with an Ar ion gun at 2 keV and 20 mA prior to XPS measurements. For high resolution scans, pass energy was 23.50 eV, scan step was 0.025 eV and scan speed was 100 sec/step. For each sample, two spots on the film were measured and the atomic concentration of elements in each measured spot was calculated three times by the XPS data analyzer Multipak. The average of all the calculated concentrations was reported as the composition of the sample. The as-deposited films were thinned to allow interfacial XPS measurements by chemical etching with either 0.5% or 0.25% HF solutions.

Morphology Measurements

Due to inadequate sensitivity, conventional X-ray diffraction in the Bragg-Brentano geometry was not useful for the study of these thin films. Therefore, Grazing Incidence X-ray Diffraction (GIXRD) geometry was used to enhance diffraction intensity

and thus characterize the crystallinity of the deposited films. X-ray diffraction patterns were collected using a X-Pert MRD Panalytical Diffractometer; the experimental configuration is shown schematically in Figure 3.3. Use of a multiplayer parabolic mirror allowed the divergent incident X-ray beam to be converted into an intense monochromatic parallel beam. The parallel incident beam irradiates the sample at a grazing angle, with a fixed angle of incidence of 0.7 degrees, while a proportional detector scans over two theta, thereby collecting the X-ray diffraction pattern. In order to preserve the parallel beam geometry, a 0.27 degree parallel plate collimator and 0.04 rad. soller slits were inserted before the detector. The measurements were carried out using CuKα radiation.

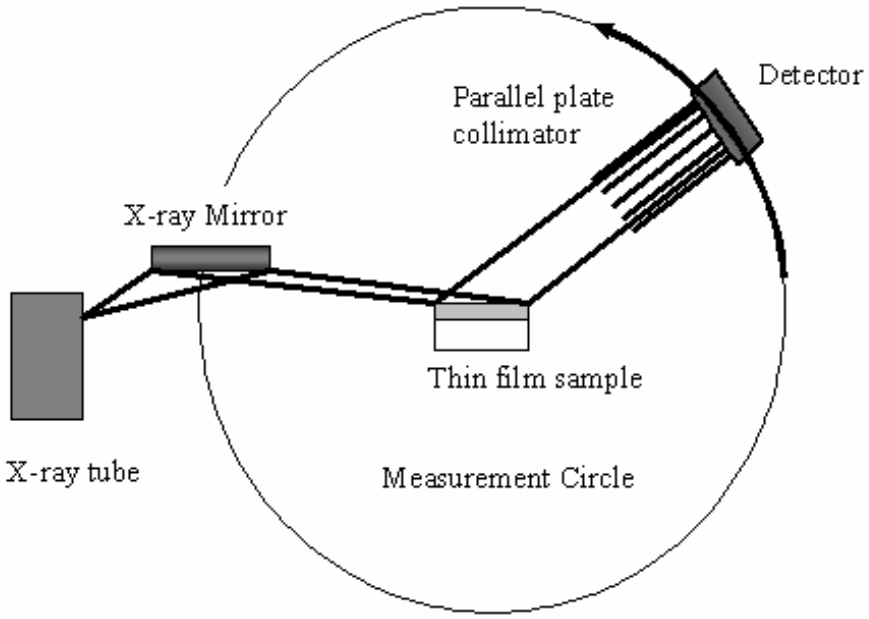

Figure 3.3 Schematic diagram of grazing incidence X-ray diffraction configuration.

Electrical Characterization

Electrical properties of HfO_2 films were measured using MIS capacitors. HfO_2 films were deposited onto p-type silicon wafers with low (< 0.01 Ohm-cm) resistivity. A blanket aluminum film of thickness ~ 300 nm was sputtered onto the wafer backside and circular platinum electrodes with 1.8 mm diameter (~200 nm thickness) were sputtered onto the HfO_2 films through a shadow mask. Capacitance-voltage (C-V) analyses were conducted on a Keithly 550 CV analyzer and current–voltage (I-V) analyses were performed with a Hewlett Packard 4156A Precision Semiconductor Analyzer. C-V measurements were performed at 100 kHz and the sweep voltage range was –5 V to +5 V. On each wafer, six electrodes were measured and the average was reported as the final result.

Thermal Stability

To determine if the films deposited by O_2 and N_2O MOCVD are stable to the high temperature processing that is typically used in microelectronic device and circuit fabrication, deposited films were annealed by rapid thermal processing (RTP) at 900 ºC under N_2 protection. During the RTP process, the temperature was raised to 900 ºC in 10 seconds and held at that temperature for 10 seconds; the furnace was then cooled down to room temperature in 2.5 minutes. The annealed films were characterized by GIXRD and their morphologies compared with those prior to annealing.

Results and Discussion

Deposition Kinetics

Deposition rates of nitrided HfO_2 films using TDEAH with either oxygen or nitrous oxide were obtained at four different temperatures: 300 ºC, 350 ºC, 390 ºC, and 410 ºC; deposition time was fixed at 10 minutes. Precursor, oxidant, and carrier gas flow rates for the depositions are listed in Table 3.1.

Thickness of these deposited films was measured by ellipsometry. For the same precursor flow rate, oxidant gas flow rate and deposition temperature, film deposition rates in oxygen are higher than those in nitrous oxide. In addition, for depositions in nitrous oxide, increasing precursor flow rates as well as increasing nitrous oxide flow rates increase the deposition rates. Deposition rates increase with substrate temperature in the range of 300 – 410 ºC, for both oxidants; Arrhenius plots of the HfO_2 film growth rate are shown in Figure 3.4. The linear relationship illustrates that over this temperature regime, film growth is controlled by precursor decomposition. Effective activation energies are 13.6 kcal/mol for O_2 and 9.9 kcal/mol for N_2O deposition. The differences observed can be partly attributed to the higher bond energy for oxygen (O-O: 119.2 kcal/mol) relative to nitrous oxide (N_2-O: 39.5 kcal/mol) although the gas phase chemistry of O_2 and N_2O is complicated [29, 30].

Table 3.1 Deposition parameters for the nitrided hafnium oxide films using oxygen and nitrous oxide.

Deposition serial #	Precursor flow rate ml/min	Oxidant gas	Helium sccm	Deposition Temp./ºC
HP1	0.06	100 sccm O_2	200	300
HP2	0.06	100 sccm O_2	200	350
HP3	0.06	100 sccm O_2	200	390
HP4	0.06	100 sccm O_2	200	410
HP5	0.06	100 sccm N_2O	200	390
HP6	0.03	100 sccm N_2O	200	300
HP7	0.03	100 sccm N_2O	200	350
HP8	0.03	100 sccm N_2O	200	390
HP9	0.03	100 sccm N_2O	200	410
HP10	0.03	200 sccm N_2O	100	390

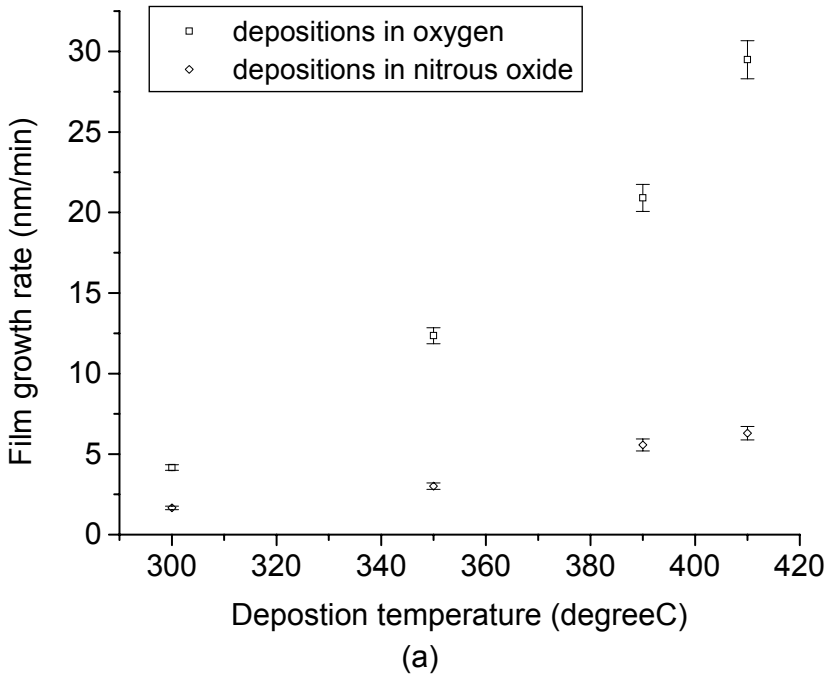

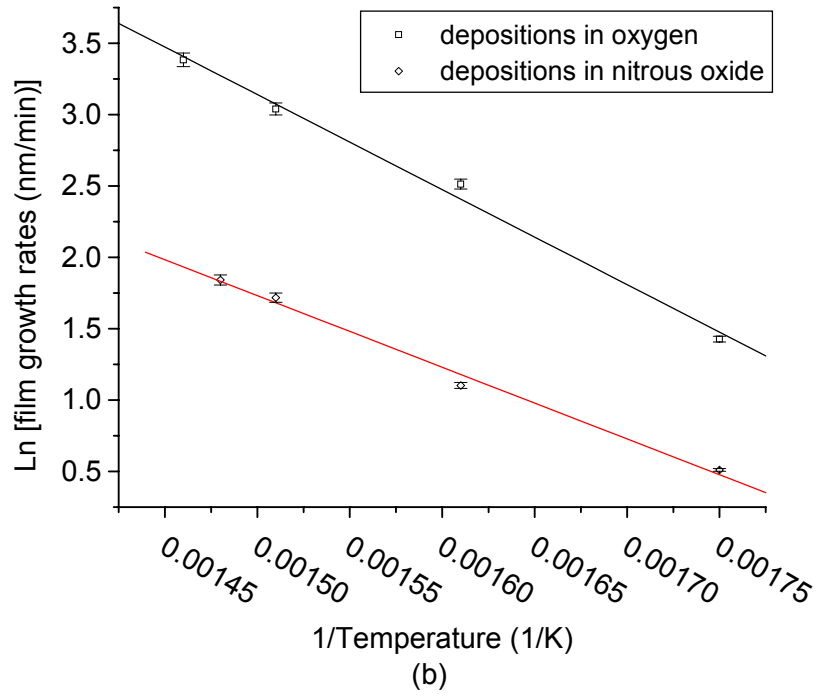

Figure 3.4 (a) Comparison of film growth rates in O_2 and N_2O at different temperatures.

(b) Arrhenius plot of nitrided HfO_2 films growth rates versus 1/T in O_2 and N_2O.

Morphology

Morphologies of deposited HfO_2 films were characterized by GIXRD measurements. Figure 3.5 shows GIXRD patterns of the nitrided HfO_2 films deposited in oxygen at substrate temperatures of 350 °C, 390 °C and 410 °C. It is obvious that films deposited in oxygen contain crystalline phases. Peak intensities were normalized to the maximum intensity diffraction peak for each pattern; Bragg reflection indices are noted on the figure. Although the cubic and tetragonal phases of HfO_2 films have similar GIXRD patterns, the observed peaks match the standard powder file of cubic phase (PDF reference code: 00-053-0560 Figure 3.7) better than those of the tetragonal phase. Peaks at 2 theta angles of 30.55 °, 35.47 °, 51.11 °, 60.71 °, 63.83 °, 74.78 °, 82.82 ° in the collected diffraction patterns correspond to the (111), (200), (220), (311), (222), (400), (331) diffractions of the cubic hafnium oxide phase respectively. Clearly, nitrided HfO_2 films deposited in oxygen have high crystalline phase content, even when the substrate temperature is as low as 350 °C. These conclusions are also in agreement with other studies that have reported cubic phase HfO_2 formation at low temperatures [31]. When the deposition temperature is lowered from 410 °C to 350 °C, an amorphous reflection peak around 32.0° – 33.5 ° appears. Therefore, the films deposited at 350 °C are more likely mixtures of cubic crystallites and amorphous phases. In addition, when the substrate temperature is increased from 350 °C to 410 °C, the full width half maximum (FWHM) of the peaks decreases, indicating that films deposited at higher temperatures contain larger crystallites.

Figure 3.6 shows the GIXRD patterns of nitrided HfO_2 films deposited from nitrous oxide. In each scan, a broad diffuse peak centered around 32^o can be observed, which demonstrates that the HfO_2 films deposited in nitrous oxide are amorphous to the detection limit of GIXRD (<2.0 nm crystallite size) at all deposition temperatures. These observations indicate that the oxygen source used for deposition is an important parameter in establishing the specific crystalline phase in HfO_2 films deposited within this particular temperature range.

Because of the bond energy in nitrous oxide (N_2-O: 39.5 kcal/mol) is smaller than that in oxygen (O-O: 119.2 kcal/mol), more oxygen radicals can be provided by nitrous oxide dissociation in the low temperature range employed in this study. Thermal reactions in both oxidants are shown below [32]:

In oxygen,

$$O_2 \rightarrow 2O$$

$$2O \rightarrow O_2$$

In nitrous oxide,

$$N_2O \rightarrow N_2 + O$$

$$O + O \rightarrow O_2$$

$$O + N_2O \rightarrow 2\ NO$$

$$O + N_2O \rightarrow N_2 + O_2$$

$$O + NO \rightarrow NO_2 + h\nu$$

$$NO_2 + N_2O \rightarrow N_2 + O_2 + NO$$

Although reactions in nitrous oxide seem complicated, at low temperatures, most of the products of thermal reactions are N_2, O_2, and O radicals [32]. It is believed that

oxygen radicals promote the formation of amorphous hafnium oxynitride films as result of two factors. First, oxygen radicals promote gas phase reactions so that more oxygen-containing film precursor can be produced. Film precursors adsorb onto the substrate surface and form films without leaving much time for surface diffusion; thus, deposited layers have little time to transform into ordered crystalline structures. Second, oxygen radicals have high sticking coefficients on silicon substrates, thereby inhibiting diffusion on the surface [33]. These two reasons probably account for the fact that films deposited in nitrous oxide are amorphous. The results have demonstrated that deposition using oxygen radicals is an efficient method to grow amorphous hafnium oxynitride, which is regarded as a poor glass forming material [34, 35].

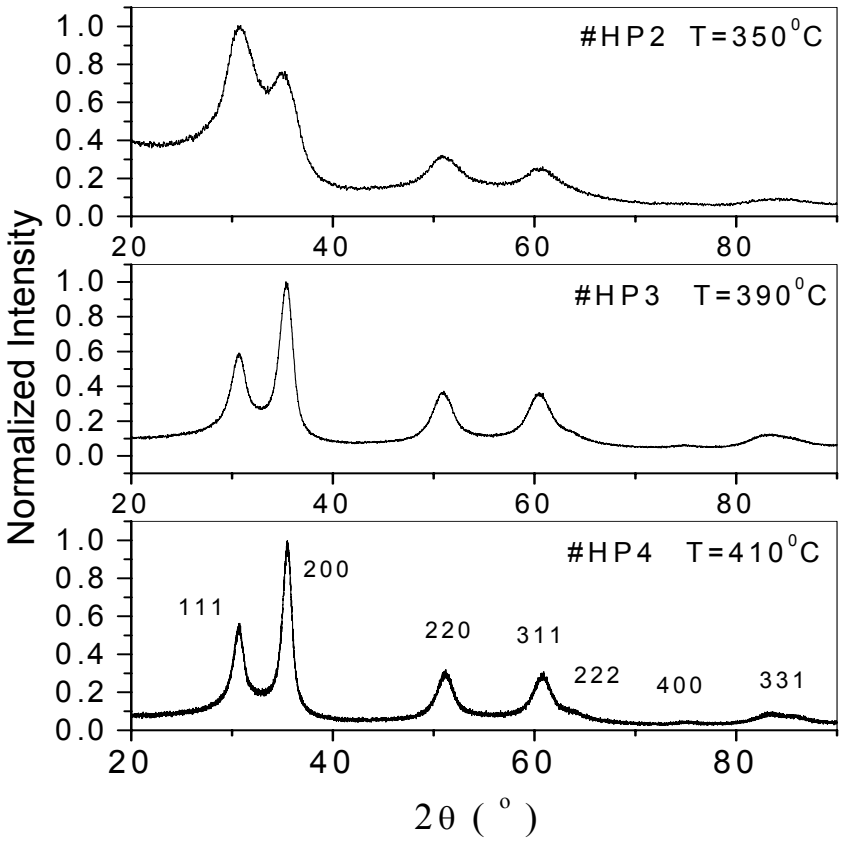

Figure 3.5 X-ray diffraction patterns of HfO_2 films deposited under O_2 atmosphere.

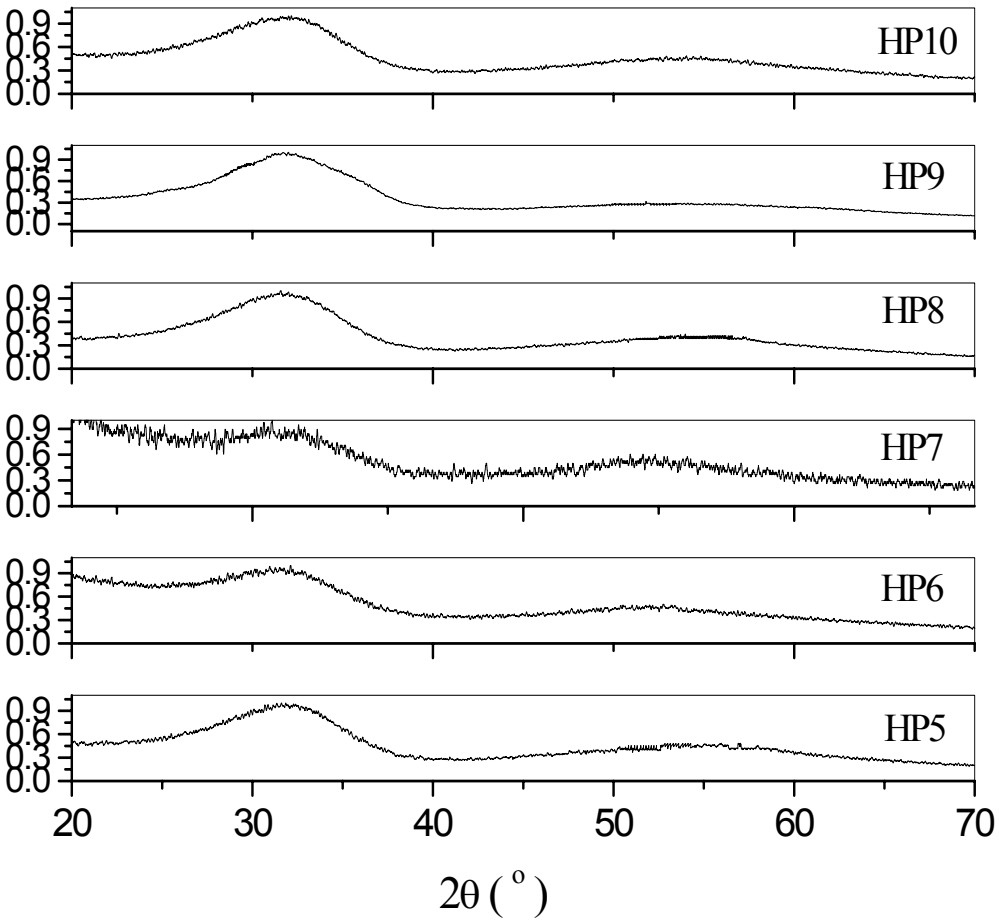

Figure 3.6 X-ray diffraction patterns of HfO_2 films deposited under N_2O atmosphere.

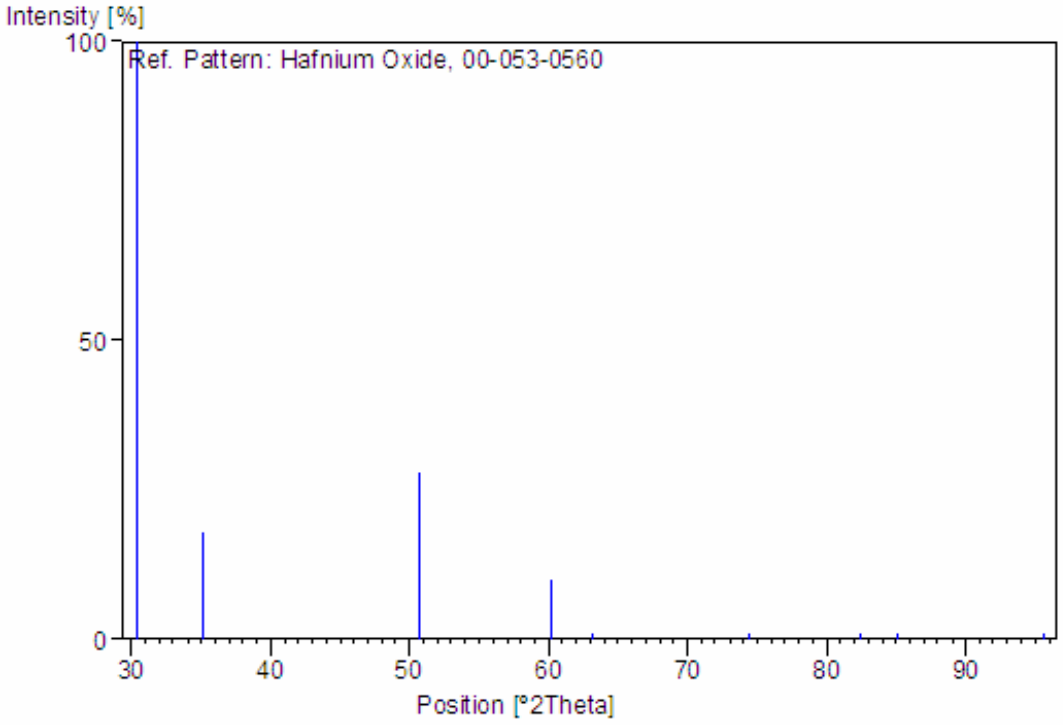

Figure 3.7 Stick pattern of cubic hafnium oxide crystals, PDF reference code: 00-053-0560.

Since amorphous dielectric films provide an improved barrier to dopant diffusion relative to that in polycrystalline films where diffusion occurs readily at crystallite grain boundaries, improved reliability of devices fabricated from amorphous films should result [36].

Composition and Interface Measurements

XPS survey spectra of nitrided HfO_2 films deposited in oxygen and nitrous oxide display a N1s peak at 392.0 eV, which confirms film nitridation [27, 28]. As reported previously [14], nitrogen in the films arises from the amide precursor. In addition, a C1s peak at 284.8 eV was detected in the XPS spectra of films deposited in both oxidants.

High-resolution XPS scans after 60 sec Ar ion sputtering have been used to estimate elemental film composition. The films consist of Hf, O, N and a small amount of C residue. Their atomic ratios are shown in Tables 3.2 and 3.3. For films deposited in oxygen, carbon concentrations are in the range of 2.5-4.5 at. %. Nitrogen concentrations for these films are in the range of 0.5-2.0 at. %. When the deposition temperature changes, the carbon content and nitrogen content have no obvious change within the error range of the measurement.

For films deposited using nitrous oxide, 3.0-6.5 at. % carbon is incorporated, which is higher than the amount of carbon incorporated into films deposited with oxygen as the oxidant gas. No obvious trend of carbon concentration with temperature is observed. For the N_2O-based films, nitrogen concentrations are 0.6-2.0 at. %, which is similar to those of the films deposited in oxygen. Furthermore, the N1s spectra also consist of Hf-N and N-C peaks. The N1s peak at 400.5 eV is also attributed to residual – $N(CH_3)_4$ ligands from the precursor.

Table 3.2 Atomic concentrations of films deposited by O_2 MOCVD.

Deposition Temp.(^oC)	O at.%	Hf at.%	N at.%	C at.%
300	65.31±1.1	30.81±0.5	1.04±0.3	2.84±1.1
350	62.46±1.1	33.05±0.5	1.63±0.8	2.86±0.9
390	61.9±1.1	32.15±0.4	1.53±0.5	4.42±0.8
410	62.49±0.5	33.89±0.5	0.69±0.4	2.93±0.6

Table 3.3 Atomic concentrations of films deposited by N_2O MOCVD.

Deposition Temp.(°C)	O at.%	Hf at.%	N at.%	C at.%
300	58.96±0.5	37.17±1.1	0.61±0.3	3.26±0.5
350	60.59±1.0	33.21±0.3	1.68±0.4	4.52±1.4
390	64.83±1.2	31.04±1.2	1.14±0.6	2.99±0.5
410	61.09±0.7	31.5±1.2	1.28±0.7	6.13±1.5

The O/Hf molar ratio of films deposited in O_2 and N_2O display no obvious differences; the ratio is ~2 for both films, as shown in Figure 3.8. Such observations indicate that the specific oxidizing environment (O_2 or N_2O) does not significantly change the oxygen content in the films.

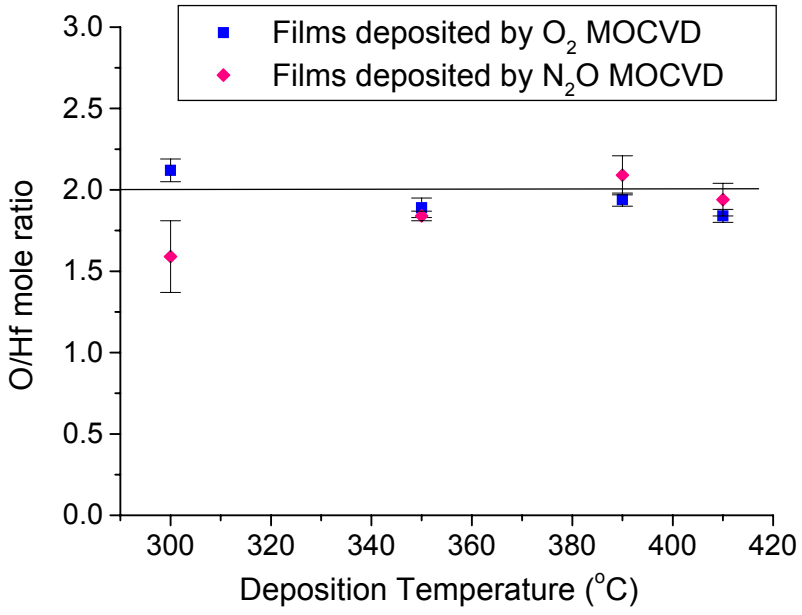

Figure 3.8 O/Hf molar ratio in hafnium oxynitride films deposited in oxygen and nitrous oxide. All films are deposited at 350 °C.

In order to characterize interfacial composition at the oxynitride film/silicon substrate, films were deposited using either oxygen or nitrous oxide with the same oxidation time (10 minutes) at 350 °C; the O_2-grown film had a thickness of 135 nm, while the N_2O-based film had a thickness of 36 nm. Both films were etched in dilute HF solutions to obtain solution etch rate data and to reduce their thickness for subsequent XPS studies of the interface with silicon. Because the densities of the two films are different, the film deposited in oxygen was etched in 0.5% HF solution while the film deposited in nitrous oxide was etched in 0.25% HF solution. Film thickness is plotted in Figure 3.9 as a function of solution etch time. The etch rate data clearly indicate that two layers with different composition/bonding structures are present in the deposited films. The top layers of the films have higher etch rates in HF solution than do the bottom layers. The estimated thickness of the bottom layer deposited in nitrous oxide is ~28% of the total film thickness, while the percentage is ~30% for the film deposited in oxygen. These data suggest that nitrous oxide- and oxygen-based depositions yield similar interfacial thickness, at least as measured by dilute HF etch rates. The etch rates of the film deposited in oxygen (in 0.5 % HF solution, 9.4 nm/min for the bulk and 0.6 nm/min for the interfacial layer) are lower than those of the film deposited in nitrous oxide (in 0.25 % HF solution, 45.3 nm/min for the bulk and 11.5 nm/min for the interfacial layer) although the oxygen-deposited film was etched in the HF solution with higher concentration. The lower each rate of films deposited with oxygen shows they have higher density than films deposited with nitrous oxide [37]. Such results are consistent

with the GIXRD studies described above, since it is believed that amorphous films etch more rapidly than do crystalline films.

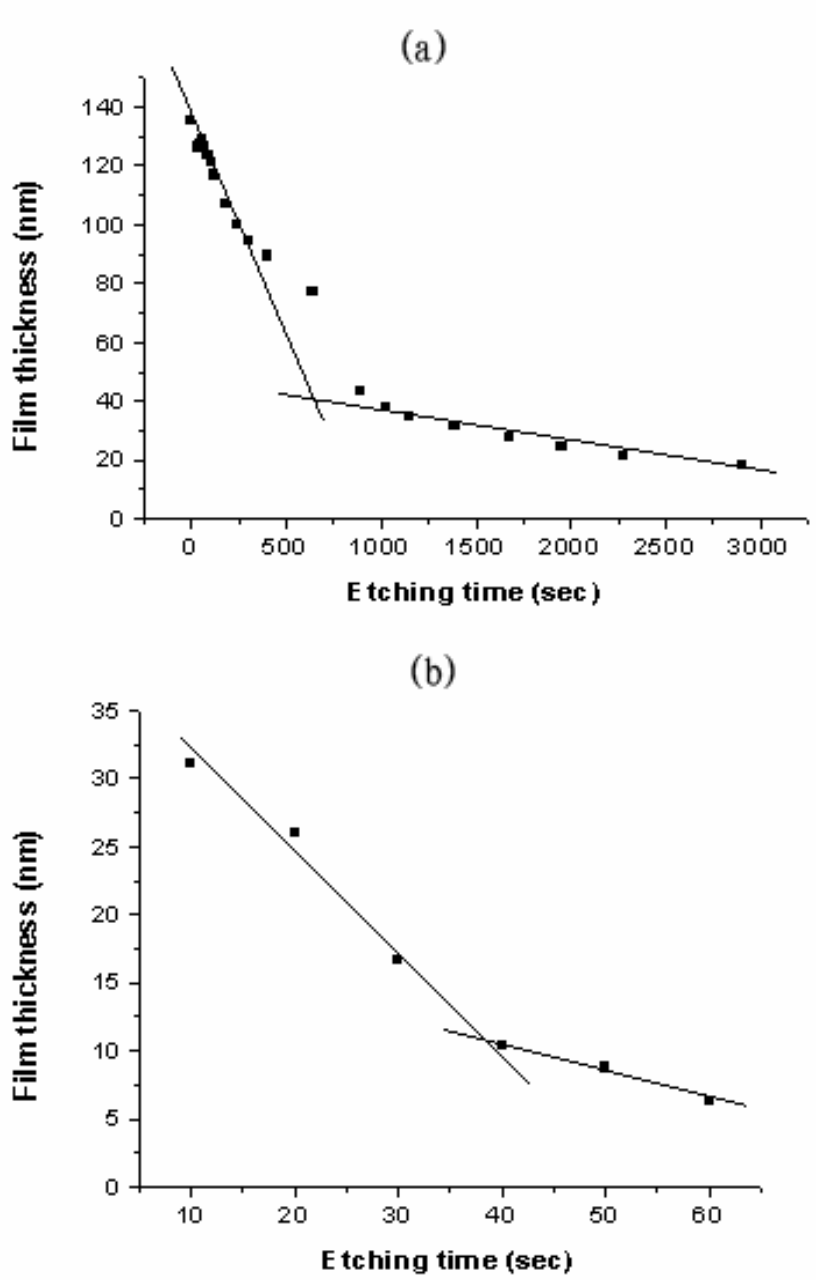

Figure 3.9 Film thickness vs etching time. (a) HfO_2 films deposited in oxygen and etched in 0.5% HF. (b) HfO_2 films deposited in nitrous oxide and etched in 0.25%HF.

After both films were etched to 6.7 ± 0.5 nm, XPS analyses were performed on the resulting films to characterize their interfaces with silicon; Figure 3.10 a, b show the Si 2p spectra for both films. Each Si 2p spectrum has two peaks with binding energies of 99.6 eV and 102.6 eV. The 99.6 eV peak is attributed to Si-Si bonds and the peak at 102.6 eV is associated with Si-O bonds (including Si-O-Si bonds and Si-O-Hf bonds) [13]. Hafnium atoms and nitrogen atoms are also detected in this interface layer. These results confirm that the interfacial layers in both films are nitrided hafnium silicate. The composition difference between the bulk and interfacial layers of the films partly accounts for the different etch rates in dilute HF solutions. Figures 3.11a and 3.11b compare the XPS N1s spectra of the bulk and interfacial regions of the two films. Figure 3.11a demonstrates that the nitrogen concentrations in the bulk regions of the two films are similar. However, the nitrogen concentration in the interfacial region of the film deposited in oxygen (9.30 at.%) is significantly higher than that in the bulk (1.87 at.%), while the nitrogen concentration in the interfacial region of the film deposited in nitrous oxide (1.62 at.%) is slightly reduced relative to that in the bulk (2.49 at.%), as Figures 3.11b and 3.12 show. Based on these results, the concentration of nitrogen accumulates at the film interface with silicon for films deposited in oxygen while for films deposited in nitrous oxide; the nitrogen concentration at the interface with silicon is reduced. Also, Hf4f peaks of the interfacial regions shift to higher binding energies compared to Hf4f peaks of the film bulk regions, as shown in Figure 3.13. For films deposited at 350 °C, Hf4f binding energies are 17.24 eV for the bulk of oxygen-deposited films, 17.48 eV for the interface of oxygen-deposited films; 17.24 eV for the bulk of nitrous oxide-deposited films, 17.96 eV for the interface of nitrous oxide-deposited films. These results indicate

that hafnium species in the interfacial layers are more completely oxidized than those in the bulk regions for both films. In addition, the results demonstrate that the interfacial regions of nitrous oxide- deposited films are more fully oxidized than the interfaces of oxygen-deposited films.

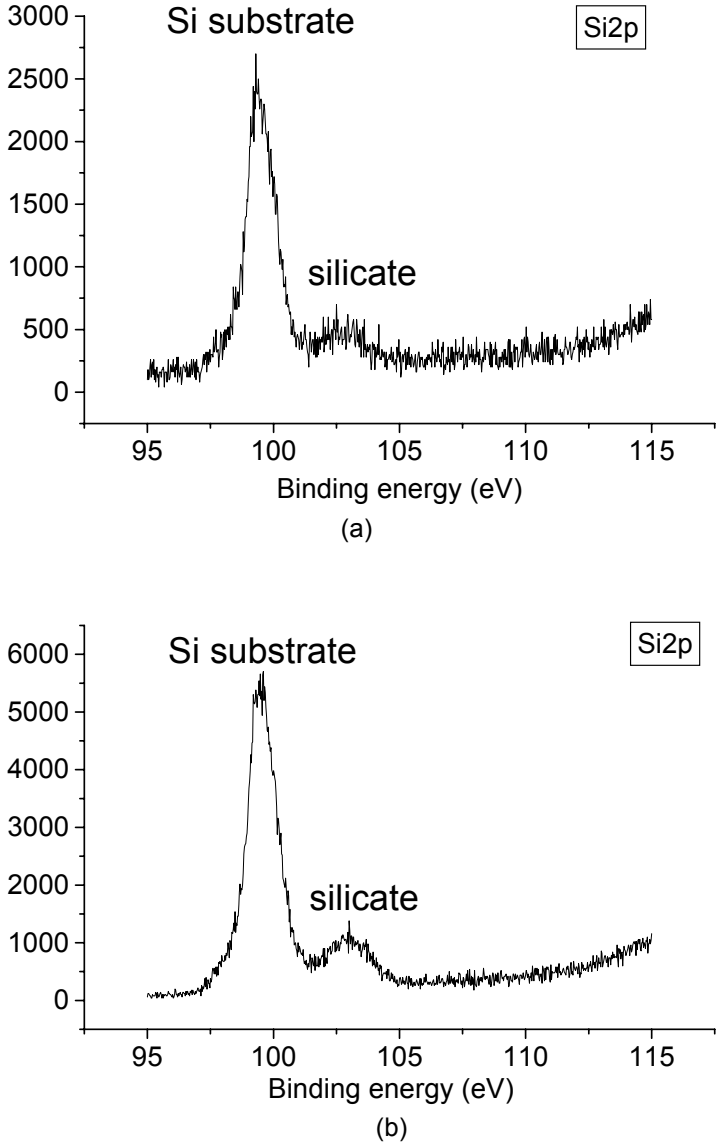

Figure 3.10 (a) XPS Si2p spectra of films deposited with oxygen; (b) XPS Si2p spectra of films deposited with nitrous oxide.

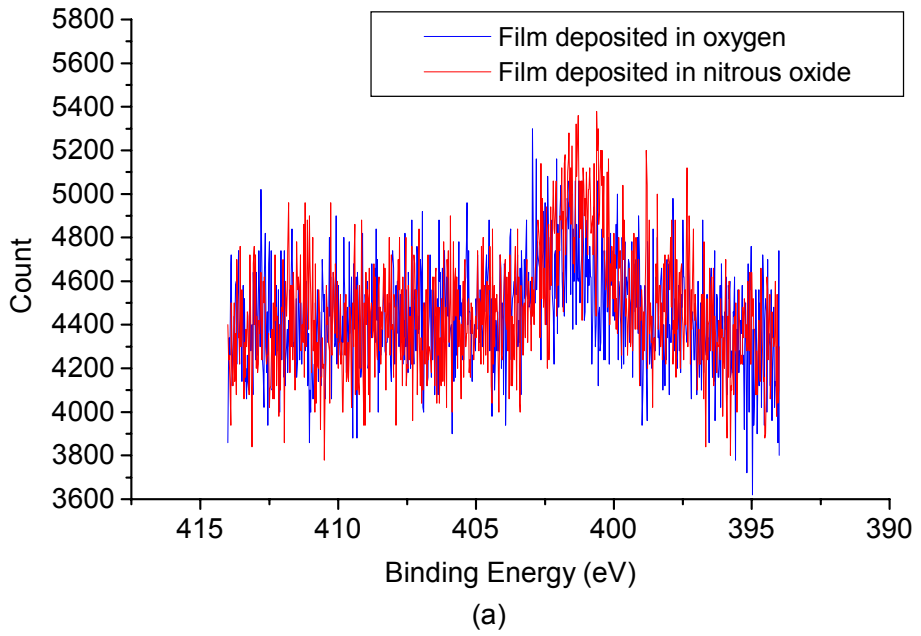

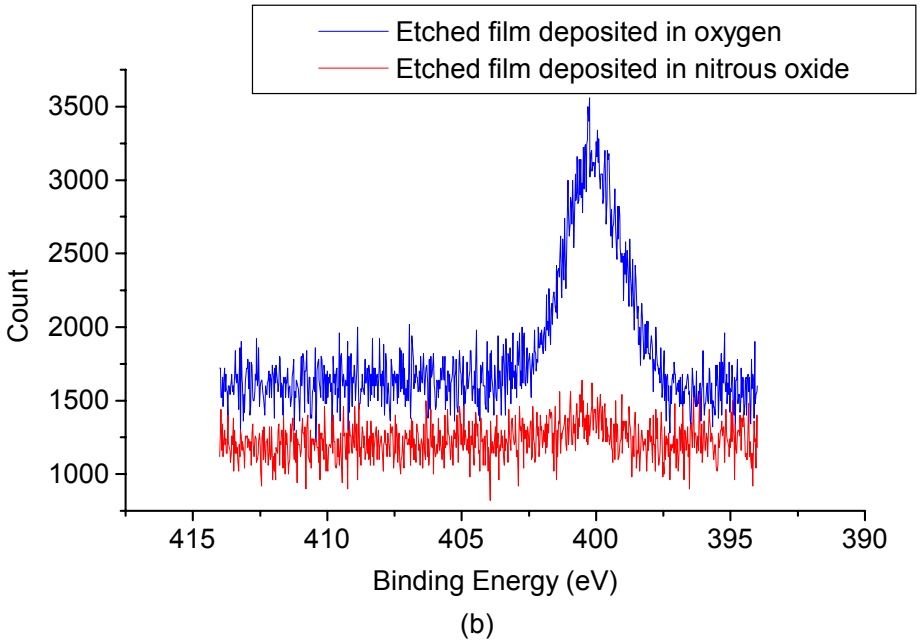

Figure 3.11 (a) XPS N 1s curves of the surfaces of as-deposited films. (b) XPS N 1s curves of the interfaces of the films that are exposed by HF etching.

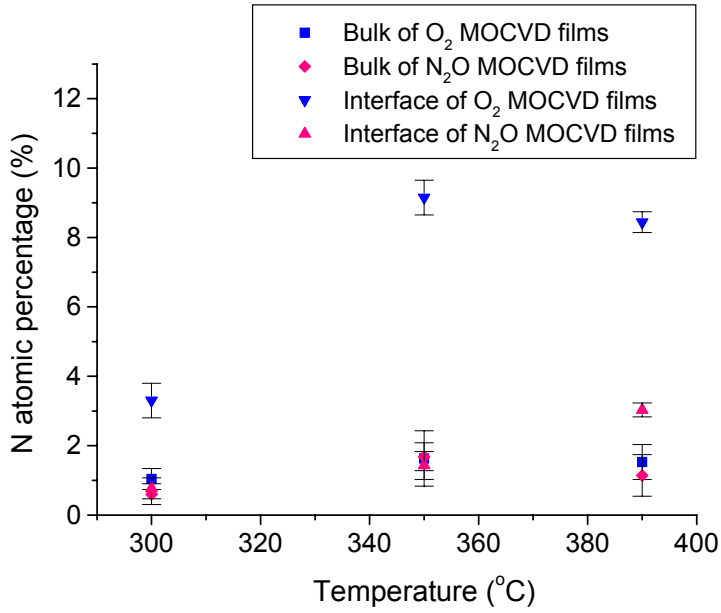

Figure 3.12 Comparison of N concentrations in films (bulk and interface) deposited in O_2 and N_2O.

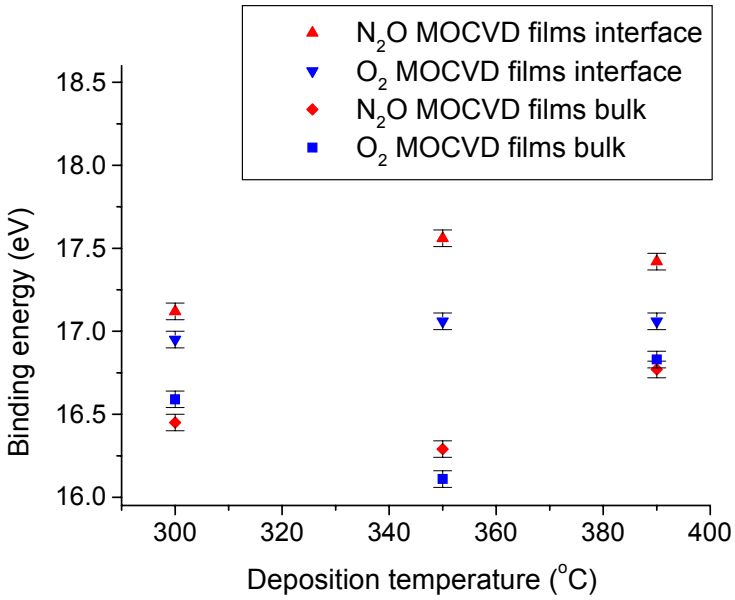

Figure 3.13 Comparison of XPS Hf4f7/2 peak positions at films (bulk and interface) deposited in O_2 and N_2O.

The different nitrogen profiles observed in the films deposited in the two oxidants can result from at least two considerations. In crystallized films, nitrogen atoms can readily diffuse along grain boundaries and accumulate at the interface between the high-k film and the silicon substrate [38]. Because hafnium oxide films deposited in nitrous oxide are amorphous based on GIXRD measurements, nitrogen atom diffusion is inhibited while crystalline films deposited in oxygen more readily permit nitrogen diffusion. Furthermore, because the N_2-O bond energy of nitrous oxide (39.5 kcal/mol) is substantially less than the O-O bond energy of oxygen (119.2 kcal/mol), more highly reactive oxygen species are available from nitrous oxide than from oxygen at the low temperatures involved in this study [29]. The higher concentration of reactive oxygen species thus results in more extensive replacement of nitrogen atoms in the bulk and especially in the interfacial region of nitrided hafnium oxide films with the silicon substrate [39, 40]. Higher concentration of reactive oxygen species also results in more completely oxidized hafnium species in the interfacial regions of films deposited in nitrous oxide.

For the above reasons, lower nitrogen concentrations exist at the interface of nitrous oxide-deposited films with silicon relative to those of films deposited in oxygen. In addition, these considerations can explain the slightly smaller nitrogen concentration in the bulk of nitrous oxide-deposited films compared to that in the bulk of oxygen-deposited films. Such results suggest that chemical vapor deposition with an amid precursor and nitrous oxide offers an alternate approach to the design of nitrided hafnium oxide films with desired nitrogen concentrations and distributions. Unlike post-annealing

nitridation techniques and oxygen-based depositions, nitrous oxide-assisted decomposition of amid precursors can introduce nitrogen atoms into the bulk of deposited films but keep the nitrogen concentration at the interface with silicon low. The specific nitrogen distribution is critical, since nitrogen atoms at the interface between high-k films and silicon substrates are believed to degrade the performance of electronic devices [38].

Electrical Properties

Accumulation capacitance measurements on metal-oxide-semiconductor capacitor structures using HfO_xN_y films yielded the dielectric constants listed in Table 3.4. Films deposited in oxygen have dielectric constants in the range of 20.0 to 25.0 while the dielectric constants of films deposited in nitrous oxide range between 15.0 and 19.0. The lower dielectric constants of films obtained from nitrous oxide result from the lower cystallinity of these films [16]; such conclusions are consistent with the XRD results that were discussed earlier in this chapter. Capacitance – voltage (CV) plots (Figures 3.14 and 3.15) indicate that the voltage range for the depletion region (voltage necessary to transition from inversion to accumulation) for films deposited in nitrous oxide is smaller than that for films deposited in oxygen; differences are more apparent for films deposited at lower temperatures. The average oxide charge concentrations of the films were determined from the flatband shift of high-frequency CV plots using $Q_{ox} = C_i \Delta V_{fb} / q$ [41, 42]; results are shown in Table 3.5. For these calculations, the Pt work function is 5.3 V, Si work function is 4.05, and boron doping density is $10^{19}/cm^3$. Clearly, films deposited from nitrous oxide have fewer interface traps than do films deposited in an oxygen environment. The combination of electrical properties, XRD data, and XPS results indicate that the difference in oxide charge densities of the HfO_xN_y films can be

explained by the different nitrogen concentrations and oxidation extent of hafnium at the interface of the films with silicon. Possible reasons for the improved electrical properties of films deposited from N_2O MOCVD will be discussed later in this chapter. Although increased nitrogen concentration may increase the dielectric constant of the high-k film, the accumulated nitrogen also introduces traps (states) at the interface and thus degrades the electrical performance of devices.

Table 3.4 Dielectric constants of the hafnium oxide films deposited in oxygen and nitrous oxide (error bar: ± 1.0).

Oxidant	300 °C	350 °C	390 °C	410 °C
O_2	21.7	22.3	20.1	24.2
N_2O	N/A	18.3	18.6	15.4

Table 3.5 Oxide charge densities of MIS structures from films deposited in oxygen or nitrous oxide at different temperatures (error bar: ± 2.0 e11).

Oxidant	Oxide charge density (/cm^2)		
	350 °C	390 °C	410 °C
Oxygen	3.51e12	7.22e11	5.11e11
Nitrous oxide	2.11e12	5.56e11	3.90e11

Current – voltage (IV) plots (Figures 3.16 and 3.17) and leakage currents measured at 0.2 MV/cm (Table 3.6) indicate that MIS structures of the films deposited from nitrous oxide have comparable or smaller current flow (leakage) than do films

deposited from oxygen at deposition temperatures below 400^{o}C. These data indicate that the amorphous structure and the lower nitrogen concentration in interfacial layers of hafnium oxynitride films obtained from deposition in nitrous oxide can reduce the leakage current of MIS capacitors.

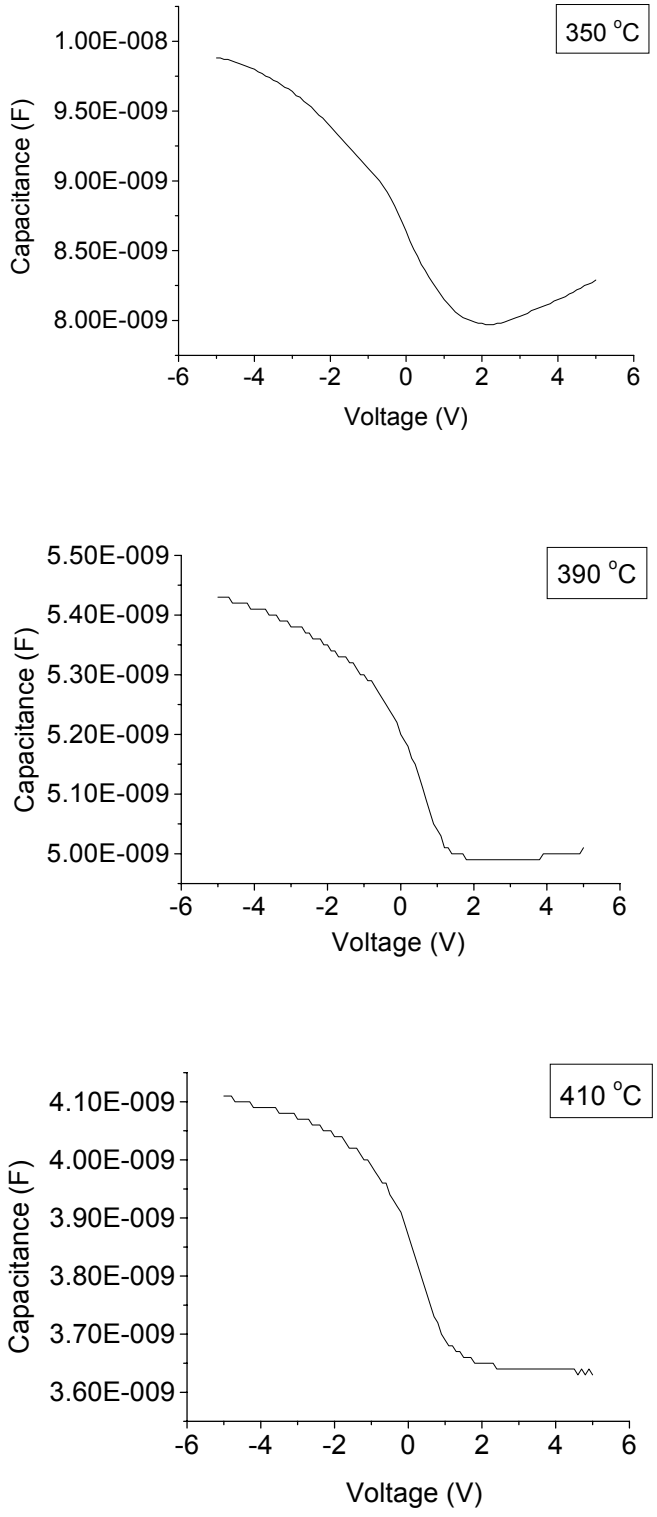

Figure 3.14 Capacitance – voltage curves of MIS capacitors from films deposited in oxygen; thicknesses of the films are 51 nm, 80 nm, 134 nm respectively.

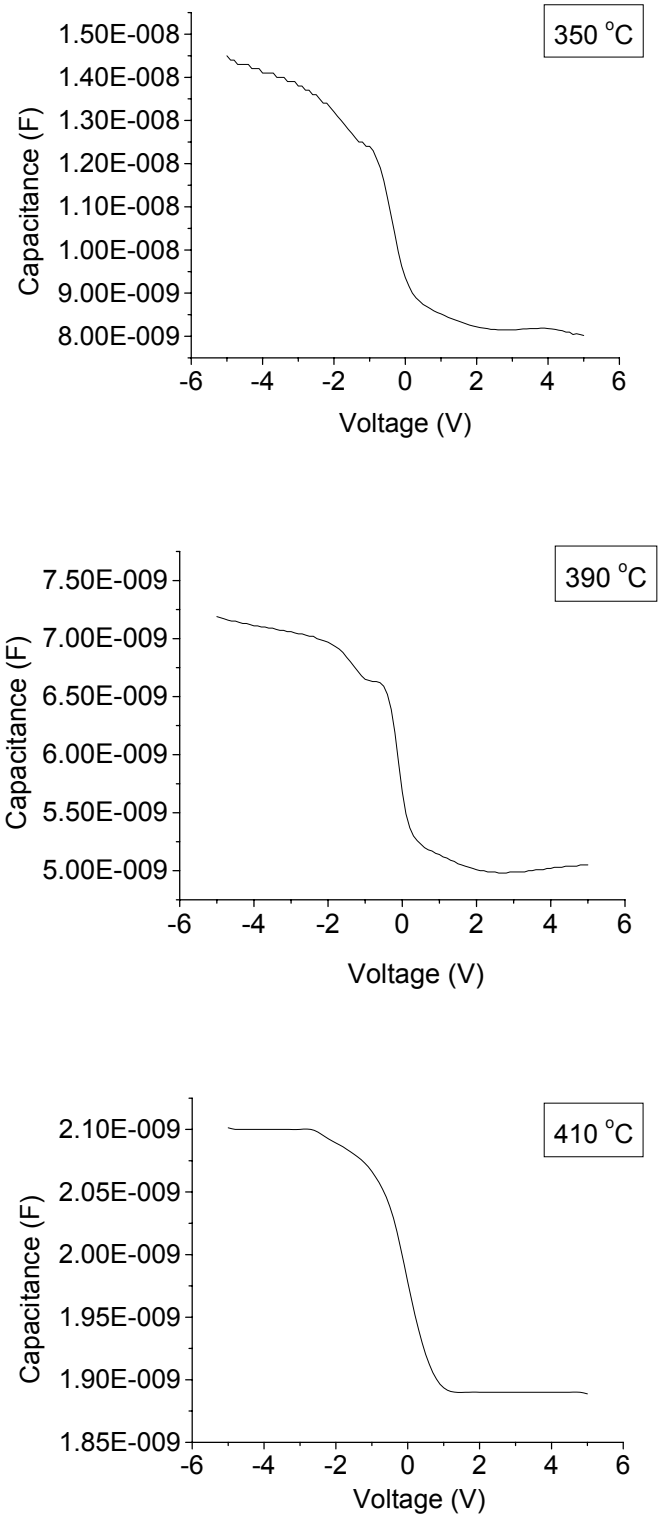

Figure 3.15 Capacitance – voltage curves of MIS capacitors from the films deposited in oxygen; thicknesses of the films are 29 nm, 54 nm, 123 nm respectively.

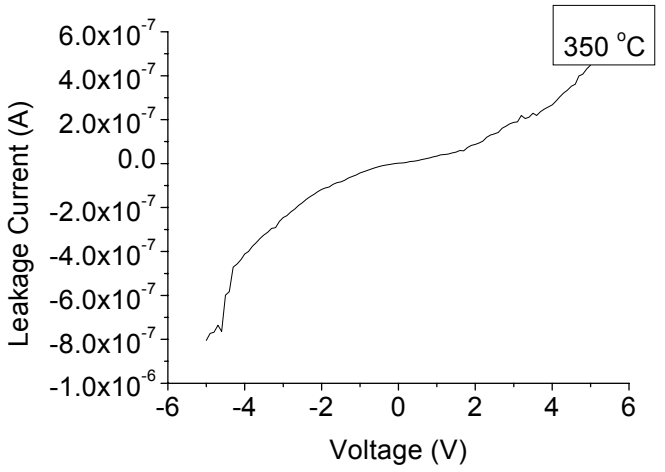

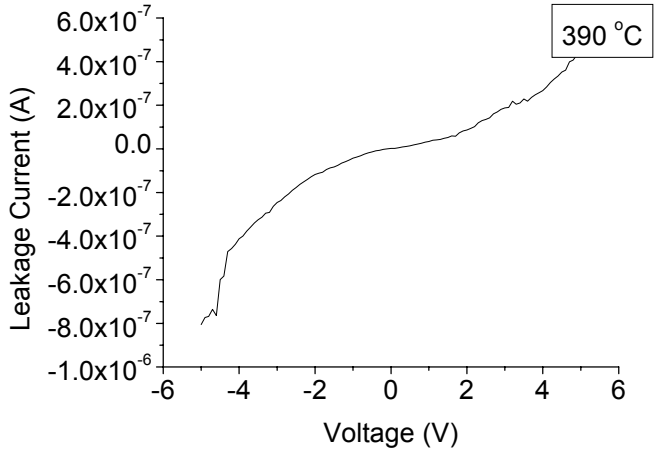

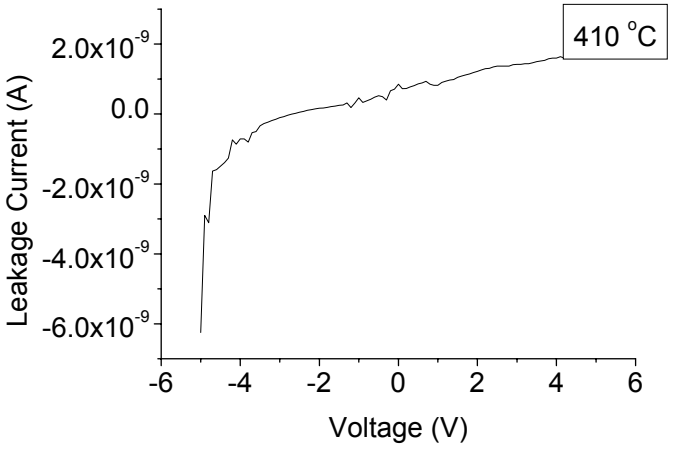

Figure 3.16 Leakage current – voltage curves of MIS capacitors from films deposited in oxygen.

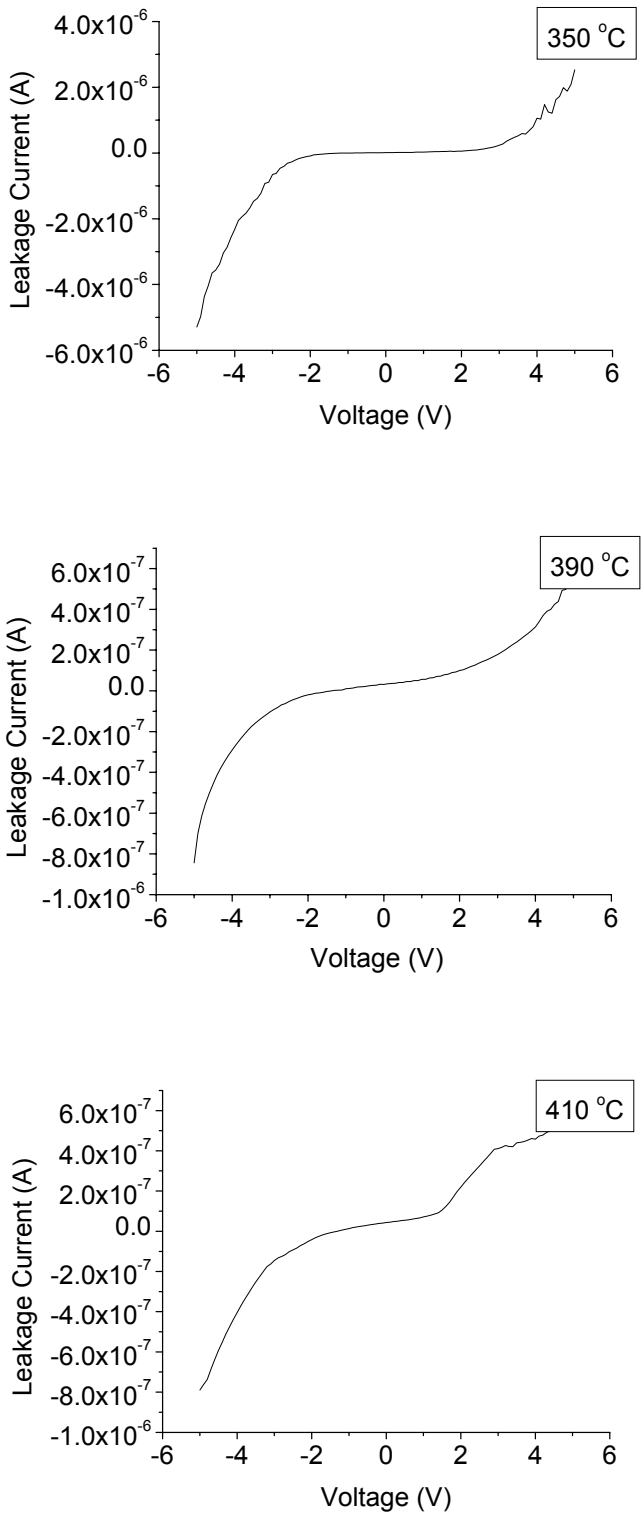

Figure 3.17 Leakage current – voltage curves of MIS capacitors from films deposited in nitrous oxide.

Table 3.6. Leakage current of MIS structures from films deposited in oxygen or nitrous oxide at different temperatures with an applied electric field of 0.2 MV/cm.

Oxidant	Leakage current at different temperatures (A/cm^2)		
	350 °C	390 °C	410 °C
Oxygen	1.90e-5	8.40e-7	6.25e-7
Nitrous oxide	4.35e-7	4.40e-7	8.54e-6

Thermal Stability

In order to determine the thermal stability of films deposited in oxygen and nitrous oxide, hafnium oxynitride films were annealed in nitrogen by rapid thermal processing (RTP) at 900 °C for 10 seconds. Figure 3.18 shows the GIXRD patterns of annealed films that had been deposited at 350 °C. For the film deposited with oxygen, the crystalline phase changes from cubic to monoclinic after high-temperature annealing. Previous studies have reported that the monoclinic phase is the most stable phase of hafnium oxide at temperatures below 1700 °C [43]. The phase of the film deposited from nitrous oxide becomes crystalline (from amorphous) after 900 °C RTP annealing; both monoclinic and tetragonal phases are detected by GIXRD (Figure 3.18 b). These results indicate that in order to maintain hafnium oxynitride films deposited in nitrous oxide amorphous, high temperature annealing during microelectronic processing sequences must be avoided.

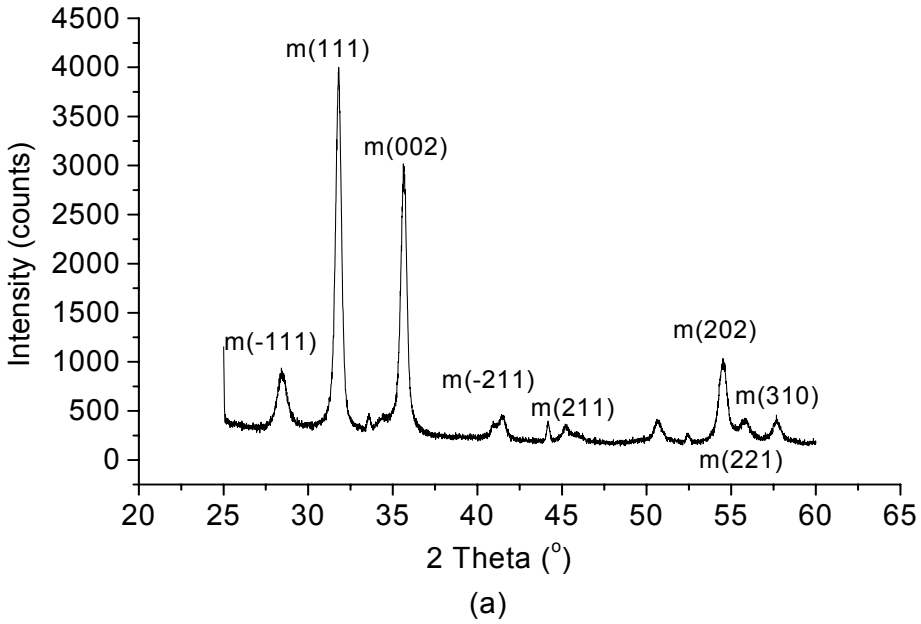

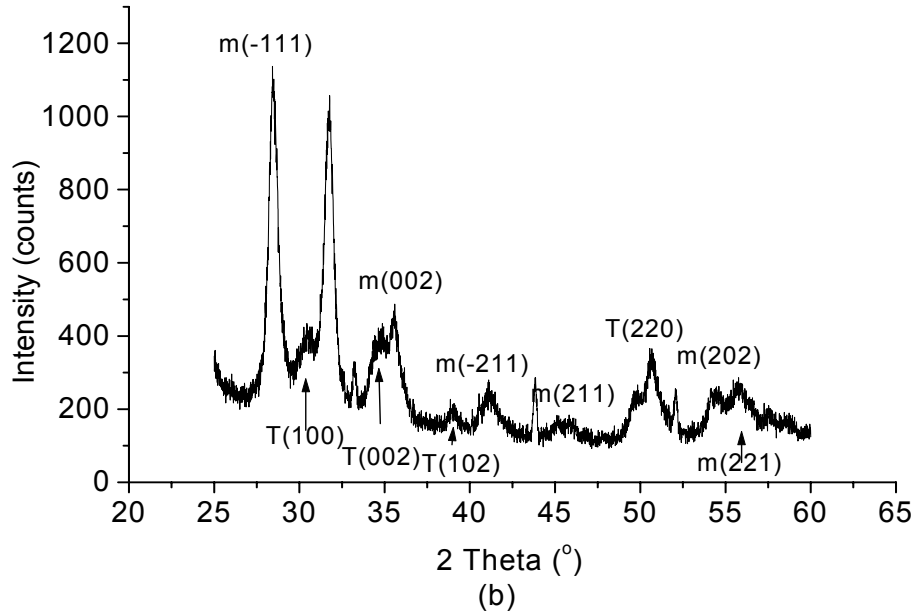

Figure 3.18 (a) GIXRD patterns of 900 °C RTP annealed films that had been deposited in oxygen; (b) GIXRD patterns of 900 °C RTP annealed films that had been deposited in nitrous oxide. Both films were deposited at 350 °C.

Reasons for Electrical Property Improvement of Films Deposited in N_2O

Since the early 1960s, defects present in silicon oxide gate dielectrics have been investigated intensively because an understanding of the origin of defects in gate dielectrics, especially at the SiO_2/Si interface, is essential to performance improvement of transistors [44-49]. For the SiO_2/Si interface, it is widely accepted that the defects present originate from a number of sources as illustrated in Figure 3.19 [50]:

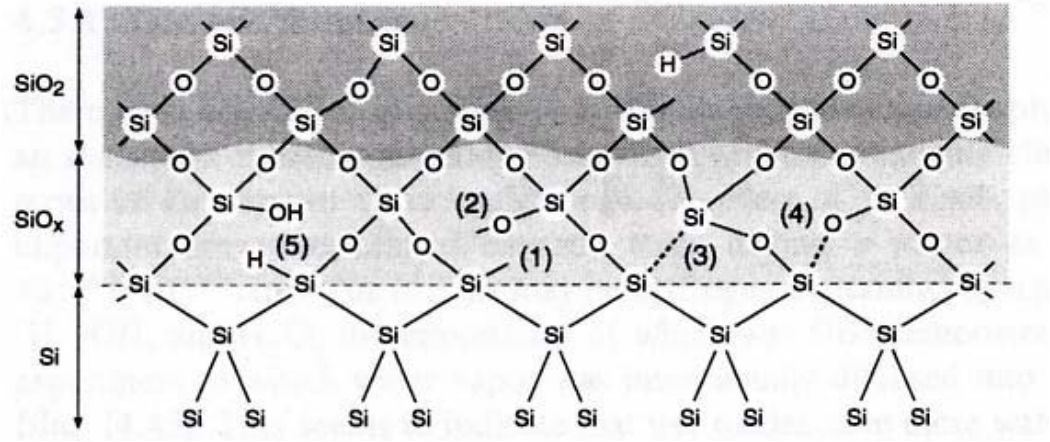

Figure 3.19 Schematic illustration of likely defect sources at the silicon oxide/silicon interface [50].

(1) Trivalent silicon, ≡ Si· : This defect is positively charged after capturing a hole or remains neutral when empty. It is believed to be one of the most common origins of interface states.

(2) Nonbridging oxygen, ≡ Si – O· : This defect forms when a Si - O bond is broken.

(3) Weak Si - Si bond: This defect is the source of trivalent silicon.

(4) Strained Si – O bond: This defect has a reduced energy for bond breakage.

(5) Hydrogen – containing species such as – H, - OH: These defects are formed by H_2O or other H sources upon reaction with trivalent silicon or nonbridging oxygen.

(6) Impurities, such as P, B, or metals.

In high-k oxides, defects include intrinsic defects in oxides and defects at the high-k oxide/Si interface. High-k oxides contain more intrinsic defects than silicon oxide because of their ionic bonding and high coordination number. The fluorite structure of hafnium oxide is shown in Figure 3.20 [51]. Cations are arranged in the face-center-cubic (fcc) structure and anions are located at the tetragonal sites between cations. Cations have a coordination number of 8 and anions have a coordination number of 4. Unlike silicon oxide, defects in high-k oxides (such as broken bonds because of high strain stress) are difficult to eliminate by bond re-formation that causes a relaxation of the bonding network. The origins of intrinsic defects in high-k oxides are usually oxygen vacancies and oxygen interstitials.

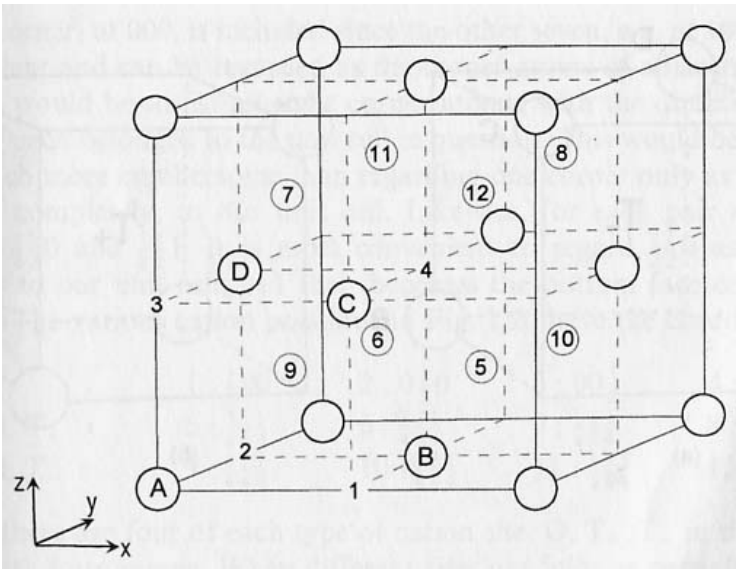

Figure 3.20 Fluorite structure of hafnium oxide. Hafnium cations are at positions such as A, B, C, D; oxygen anions are at positions such as 5-12 [51].

For high-k oxide/Si interfaces, some defects are similar to those at silicon oxide/ silicon interface such as ≡ Si · and ≡ Si – O · because the interface is essentially a mixture of metal oxide and silicon oxide. At the ideal high-k/Si interface, theoretical calculations using local density approximation (LDA) have shown that the most stable ZrO_2/Si interface structure contains threefold coordinated oxygen atoms (represented by O_3), as shown in Figure 3.21 [52]. Half of the oxygen atoms are bonded to two silicon atoms and one zirconium atom, the other half are bonded to two zirconium atoms and one silicon atom. Oxygen vacancies that result from the loss of threefold coordinated oxygen atoms (V_3) cause the films to be metallic. Because of the similarity between zirconium and hafnium, it is believed that the hafnium oxide/silicon interface has similar chemical and physical structures and thus electrical properties. By density functional theory (DFT) calculations, it has been shown that electrons can be removed from V_3 oxygen vacancies

in hafnium oxide films to form stable V_3^+ or V_3^{2+} defects [53, 54]. Electron affinities of oxygen vacancy defects are shown in a schematic energy diagram Figure 3.22. From this diagram, it can be seen that electrons may tunnel from the silicon conduction band into these defect levels (vacancies) in hafnium oxide or hafnium oxynitride films and degrade the performance of transistors.

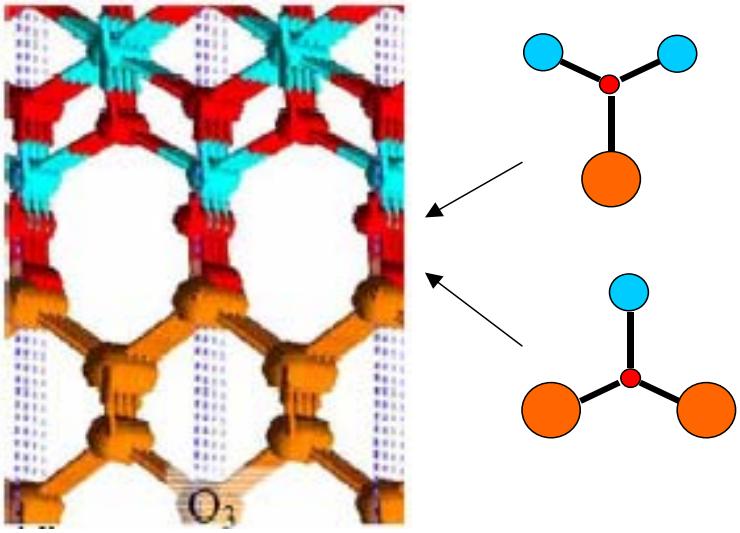

Figure 3.21 Atomic structure of stable zirconium oxide/silicon interface that is similar to hafnium oxide/silicon interface. Red: oxygen, blue: zirconium, yellow: silicon. Two kinds of threefold coordinated oxygen atoms at the interface are shown at the right side [52].

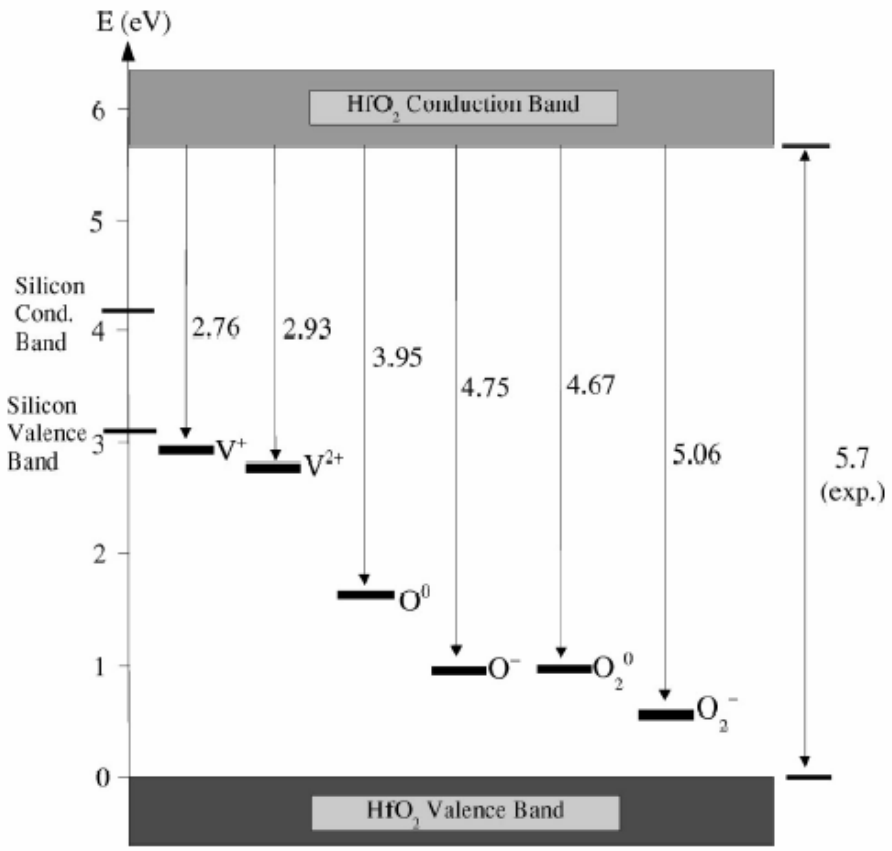

Figure 3.22 Schematic energy level diagram of various defects in hafnium oxide [54].

By density functional theory (DFT) calculations [54], the incorporation of atomic oxygen into hafnium oxide is believed to be energetically favored and thus able to remove intrinsic oxygen vacancies in hafnium oxide films. In addition, previous studies have shown that oxygen radicals can remove the defects at the silicon oxide/silicon surface such as ≡ Si – O ·, – H, and – OH [55-57]. Such theoretical and experimental results are consistent with the above assumption that oxygen radicals from the dissociation of nitrous oxide are the reason for improved electrical properties of films deposited by N_2O MOCVD.

Conclusions

Nitrided hafnium oxide films were deposited using either oxygen or nitrous oxide as the oxidant by direct liquid injection MOCVD. Deposition kinetics, crystallinity, chemical composition, bonding structure, and dielectric properties are compared. Depositions in oxygen display an activation energy of ~13.6 kcal/mol while the activation energy for depositions in nitrous oxide is ~9.9 kcal/mol. GIXRD results illustrate that nitrided hafnium oxide films obtained from nitrous oxide are amorphous while the films deposited in oxygen are mixtures of amorphous and cubic phases. XPS measurements demonstrate that the nitrogen concentration in the films obtained from oxygen is 0.5-2 % and the nitrogen concentration in the films deposited from nitrous oxide is 0.6-2 %. Both films contain hafnium silicate interfacial layers of equivalent thickness. Nitrogen content at the interface with silicon of films deposited in nitrous oxide is much smaller than that at the interface of films deposited in oxygen. The amorphous structure of nitrous oxide deposited films appears to inhibit the diffusion of nitrogen atoms through the growing films and thus reduce the nitrogen concentration at the silicon interface. Variations in dielectric constant of the films (20-25 for films deposited in oxygen, 15-19 for films deposited in nitrous oxide) result from the different phases and nitrogen content present. Lower nitrogen content and more completely oxidized hafnium species in the interfacial region of films deposited in nitrous oxide result in fewer interface traps and improved electrical properties of the films. These results indicate that chemical vapor deposition using an amide precursor and nitrous oxide in a liquid injection system is a promising approach to engineer the nitrogen content of nitrided hafnium oxide films.

REFERENCE

1. Wilk, G., Wallace, R., and Anthony, J., J. Appl. Phys., 2001. **89**: p. 5243.
2. Gusev, E.P., Copel, M., Cartier, E., Baumvol, I.J.R., Krug, C., and Gribelyuk, M.A., Appl. Phys. Lett., 2000. **76**: p. 176.
3. Houssa, M., Afanas'eV, V.V., Stesmans, A., and Heyns, M.M., Appl. Phys. Lett., 2000. **77**: p. 1885.
4. Lee, B.H., Kang, L., Nieh, R., Qi, W., and Lee, J.C., Appl. Phys. Lett., 2000. **76**: p. 1926.
5. Campbell, S.A., Ma, T.Z., Smith, R., Gladfelter, W.L., and Chen, F., Microelectron. Eng., 2001. **59**: p. 361.
6. Choi, K.J., Shin, W.C., and Yoon, S.G., J. Electrochem. Soc., 2002. **149**: p. F18.
7. Senzaki, Y., Alers, G., Hochberg, A., Roberts, D., Norman, J.T., Fleming, R., and Krautter, H., Electrochem. Solid State Lett., 2000. **3**: p. 435.
8. Mays, E.L., Hess, D.W., and Jr., W.S.R., Journal of Crystal Growth, 2004. **261**: p. 309.
9. Miotti, L., Bastos, K.P., Pezzi, R.P., Soares, G.V., Driemeier, C., Rosa, E.B.O.d., Baumvol, I.J.R., and Morais, J., Phys. Stat. Sol. (A), 2004. **201**: p. 870.
10. Nabatame, T., Iwamoto, K., Yamamoto, K., Tominaga, K., Hisamatsu, H., Ohno, M., Akiyama, K., Ikeda, M., Nishimura, T., Ota, H., Horikawa, T., and Toriumi, A., J. Vac. Sci. Technol. B, 2004. **22**: p. 2128.
11. Akbar, M.S., Cho, H.J., Choi, R., Kang, C.S., Choi, C.H., Rhee, S.J., Kim, Y.H., and Lee, J.C., IEEE Electron Dev. Lett., 2004. **25**: p. 465.

12. Ohshita, Y., Ogura, A., Hoshino, A., Hiiro, S., Suzuki, T., and Machida, H., Thin Solid Films, 2002. **406**: p. 215.

13. Schaeffer, J., Edwards, N.V., Liu, R., Roan, D., Hradsky, B., Gregory, R., Kulik, J., Duda, E., Contreras, L., Christiansen, J., Zollner, S., Tobin, P., Nguyen, B.Y., Nieh, R., Ramon, M., Rao, R., Hegde, R., Rai, R., Baker, J., and Voight, S., J. Electrochem. Soc., 2003. **150**: p. F67.

14. Takahashi, K., Nakayama, M., Yokoyama, S., Kimura, T., Tokumitsu, E., and Funakubo, H., Appl. Surf. Sci., 2003. **216**: p. 296.

15. Williams, P.A., Jones, A.C., Tobin, N.L., Chalker, P.R., Taylor, S., Marshall, P.A., Bickley, J.F., Smith, L.M., Davies, H.O., and Critchlow, G.W., Chem. Vap. Deposition, 2003. **9**: p. 309.

16. Lo, W., Kamath, A., Kher, S., Metzner, C., Wen, J., and Chen, Z., J. Mater. Res., 2004. **19**: p. 1775.

17. Choi, C.H., Jeon, T.S., Clark, R., and Kwong, D.L., IEEE Electron Dev. Lett., 2003. **24**: p. 215.

18. Bastos, K.P., Morais, J., Miotti, L., Soares, G.V., Pezzi, R.P., Silva, R.C.G.d., Boudinov, H., Baumvol, I.J.R., Hegde, R.I., Tseng, H.H., and Tobin, P.J., J. Electrochem. Soc., 2004. **151**: p. F153.

19. Bastos, K.P., Morais, J., Miotti, L., Pezzi, R.P., Soares, G.V., Baumvol, I.J.R., Hegde, R.I., Tseng, H.H., and Tobin, P.J., Appl. Phys. Lett., 2002. **81**: p. 1669.

20. Petry, J., Richard, O., Vandervorst, W., Conard, T., Chen, J., and Cosnier, V., J. Vac. Sci. Technol. A, 2003. **21**: p. 1482.

21. Wang, J.C., Hung, Y.P., Lee, C.L., and Lei, T.F., J. Electrochem. Soc., 2004. **151**: p. F17.

22. Chang, K.M., Yang, W.C., Chen, C.F., and Hung, B.F., J. Electrochem. Soc., 2004. **151**: p. F118.

23. Lay, T.S., Liao, Y.Y., Liu, W.D., Lai, Y.H., Hung, W.H., Kwo, J., Hong, M., and Mannaerts, J.P., Solid-State Electro., 2003. **47**: p. 1021.

24. Zhang, Z., Li, M., and Campbell, S.A., IEEE Electron Dev. Lett., 2005. **26**: p. 20.

25. Kim, I., Han, S.K., and Osburn, C.M., J. Electrochem. Soc., 2004. **151**: p. F22.

26. Yang, C.W., Fang, Y.K., Lin, C.S., Tsair, Y.S., Chen, S.M., Yang, W.D., Wang, M.F., Cheng, J.Y., Chen, C.H., Yao, L.G., Chen, S.C., and Liang, M.S., Electron. Lett., 2003. **39**: p. 21.

27. Lee, M., Lu, Z.H., Ng, W.T., Landheer, D., Wu, X., and Moisa, S., Appl. Phys. Lett., 2003. **83**: p. 2638.

28. Zhao, C., Elshocht, S.V., Conard, T., Xu, Z., Richard, O., Caymax, M., Gendt, S.D., and Heyns, M., Proceeding – Electrochemical Society, 2003. **22**: p. 101.

29. Song, M.K., Kang, S.W., and Rhee, S.W., Thin Solid Films, 2004. **450**: p. 272.

30. Xie, L., Zhao, Y., and White, M.H., Solid-State Electronics, 2004. **48**: p. 2071.

31. Elshocht, S.V., Baklanov, M., Brijs, B., Carter, R., Caymax, M., Carbonell, L., Claes, M., Conard, T., Cosnier, V., Cate, L., Gendt, S.D., Kluth, J., Pique, D., Richard, O., Vanhaeren, D., Vereecke, G., Witters, T., Zhao, C., and Heyns, M., J. Electrochem. Soc., 2004. **151**: p. F228.

32. Ellis, K.A. and Buhrman, R.A., Appl. Phys. Lett., 1996. **68**: p. 1696.

33. Winters, H.F. *Plasma Chemistry III*. in *Topics in Current Chemistry*. 1980. New York: Springer-Verlag.

34. Lucovsky, G. and Phillips, J.C., Microelectron. Reliability, 2005. **45**: p. 770.

35. Lucovsky, G., J. Vac. Sci. Technol. A, 2001. **19**: p. 1553.

36. Robertson, J., Eur. Phy. J. Appl. Phys., 2004. **28**: p. 265.

37. Chen, J., Yoo, W.J., Chan, D.S.H., and Kwong, D.L., Electrochem. Solid State Lett., 2004. **7**: p. F18.

38. Lee, C., Choi, J., Cho, M., Park, J., Hwang, C.S., Kim, H.J., and Jeong, J., J. Vac. Sci. Technol. B, 2004. **22**: p. 1838.

39. Khandelwal, A., Smith, B.C., and Lamb, H.H., J. App. Phys., 2001. **90**: p. 3100.

40. Chen, P., Bhandari, H.B., and Klein, T.M., Appl. Phys. Lett., 2004. **85**: p. 1574.

41. Koukab, A., Bath, A., and Losson, E., Solid-State Electro., 1997. **41**: p. 635.

42. Zeghbroeck, B.V., *Principles of Semiconductor Devices*. 2004, http://ece-www.colorado.edu/~bart/book.

43. Wang, J., Li, H.P., and Stevens, R., J. Mater. Sci., 1992. **27**: p. 5397.

44. Deal, B.E., Sklar, M., Grove, A.S., and Snow, E.H., J. Electrochem. Soc.: Solid State Science, 1967. **114**: p. 267.

45. Deal, B.E., Snow, E.H., and Grove, A.S., SCP and Solid State Technology, 1966(11): p. 28.

46. Phillips, W.E., Koyama, R.Y., and Buehler, M.G., J. Electrochem. Soc.: Solid State Science and Technology, 1979. **126**: p. 1979.

47. Montillo, F. and Balk, P., J. Electrochem. Soc.: Solid State Science, 1971. **118**: p. 1463.

48. Ginzburg, L.P., Journal of Non-Crystalline Solids, 1994. **1994**: p. 164.

49. Warren, W.L., Vanheusden, K., Fleetwood, D.M., Schwank, J.R., Shaneyfelt, M.R., and Winokur, P.S., IEEE Transactions on Nuclear Science, 1996. **43**: p. 2617.

50. Hori, T., *Gate dielectrics and MOS ULSIs: principles, technologies, and applications*. 1997, Springer.

51. West, A.R., *Basic Solid Sate Chemistry*. 1999, West Sussex, England: John Wiley & Sons, Ltd.

52. Robertson, J., Solid-State Electro., 2005. **49**: p. 283.

53. Foster, A.S., Sulimov, V.B., Gejo, F.L., Shluger, A.L., and Nieminen, R.M., Phys. Rev. B, 2001. **64**: p. 224108.

54. Foster, A.S., Gejo, F.L., Shluger, A.L., and Nieminen, R.M., Phys. Rev. B, 2002. **65**: p. 174117.

55. Chu, T.Y., Ting, W., Ahn, J.H., Lin, S., and Kwong, D.L., Appl. Phys. Lett., 1991. **59**: p. 1412.

56. Watanabe, K. and Tatsumi, T., Appl. Phys. Lett., 2000. **76**: p. 2940.

57. Kim, S.S., Stephena, D.J., Lucovsky, G., Fountain, G.G., and Markunas, R.J., J. Vac. Sci. Technol. A, 1990. **8**: p. 2039.

CHAPTER 4

EFFECT OF OXIDANT ON DOWNSTREAM MICROWAVE PLASMA ENHANCED CHEMICAL VAPOR DEPOSITION (PECVD) OF HAFNIUM OXYNITRIDE FILMS

Introduction

The previous studies have demonstrated that the specific oxidant used for direct liquid injection MOCVD hafnium oxynitride film deposition causes substantial variations of the morphology, nitrogen distribution and electrical properties of the films. From the previous studies, it is concluded that oxygen radicals and nitrogen species in the deposition environment are important factors that establish the structure and properties of deposited hafnium oxynitride films. In order to enhance radical concentrations in low temperature deposition and further clarify the effects of oxygen radicals and nitrogen species on the deposition and properties of hafnium oxynitride films, plasma excitation can be employed to allow low deposition temperatures. In fact, plasmas have already been widely used to anneal and deposit silicon oxide dielectric and high-k films (HfO_2, ZrO_2, Y_2O_3 etc) [1-22]. However, as Table 4.1 shows, little research on the plasma enhanced chemical vapor deposition (CVD) or atomic layer deposition (ALD) of hafnium oxide/oxynitride have been reported and few of these studies use remote plasma configurations despite the fact that hafnium oxide/oxynitride is currently regarded as one of the most promising candidates for a high-k gate insulator in MOS devices/circuits.

More effort on this topic is needed to understand the effects of plasma on high-k film deposition rates and film properties and possibly to develop novel processing techniques.

In this chapter, a downstream microwave plasma system is used to deposit hafnium oxynitride films with different oxidants. The effects of oxygen atoms and nitrogen species on the structures and properties of hafnium oxynitride films are studied. Compared with direct plasma enhanced chemical vapor deposition [23], downstream microwave plasma enhanced CVD (PECVD) has several advantages: (1) most electrons and ions recombine by wall collisions prior to reaching the substrate surface thereby reducing surface charging; (2) downstream plasmas can avoid or minimize direct ion and electron bombardment and thus radiation damage to the deposited films; (3) high power levels can be applied to the microwave plasma to obtain a high flux of reactive radicals without sputtering or etching the growing film. Microwave plasma activated O_2, O_2/He, N_2O, and N_2O/N_2 are employed as the oxidants in hafnium oxynitride deposition; oxidant effects on the deposition kinetics, film morphology, interface composition and electrical properties of the PECVD deposited films are discussed.

Table 4.1 Summary of previous studies on plasma enhanced CVD of hafnium oxide/hafnium oxynitride films

Reference	Material	Reactor type	Precursor and oxidant	Deposition temperature (^{o}C)	Comments
[24]	HfO_2, $HfSi_xO_y$	Inductively coupled rf remote plasma, 50 W	$Hf[OC(CH_3)_3]_4$ O_2, N_2O	275 - 425	Monoclinic phase films obtained
[25]	HfOxNy	Inductively coupled rf remote plasma, 50 W	$Hf[OC(CH_3)_3]_4$ He/O_2, He/N_2O	390	Nitrogen atoms incorporated, no further details
[26]	HfOxNy	Capacitively coupled rf plasma, 40 W	$Hf[OC(CH_3)_3]_4$, N_2	300	Nitrogen atoms incorporated increased crystallization temperature 200 ^{o}C
[27]	HfO_2	Parallel plates reactor, 20 W	$Hf[OC(CH_3)_3]_4$, Ar/O_2	250	Monoclinic phase films obtained
[28]	HfO_2	Microwave ECR ALD reactor, 2.5 kW	$Hf[OC(CH_3)_3]_4$, O_2	250	Hf-O-H in films reduced; rough surface

Experimental

Deposition

The downstream microwave plasma enhanced CVD system is a modification of an MOCVD reactor with a direct liquid injection (DLI) system that has been described previously [29]. A schematic of the modified PECVD system has been shown in Chapter 2. Oxidants flow through the downstream microwave plasma applicator where they are dissociated prior to introduction into the reactor chamber. A 90° bend in the transport tube ensures that most ions and electrons generated are eliminated by wall recombination or collisions.

P-type silicon wafers (resistivity < 0.01 Ω/cm, <100> orientation) were used as substrates. Before being loaded into the reactor, wafers were cleaned by a standard RCA sequence followed by a 30 sec dip in 1% HF solution. The RCA clean comprised immersion in a 5:1:1 H_2O : 29 % NH_4OH : 30 % H_2O_2 solution for 5 min at 70-80 ^oC followed by a de-ioinized (DI) water rinse and exposure to an aqueous 1 % HF solution for 30 sec; the wafers were then immersed in a 6:1:1 H_2O : 30 % H_2O_2 : 37% HCl solution for 5-10 min at 70 ^oC. Following a rinse in DI water and another 30 sec dip in 1% HF solution, the wafers were blown dry in nitrogen. The hafnium precursor employed is hafnium tetrakis-diethylamide ($Hf(NC_2H_5)_4$, TDEAH) which has a low decomposition temperature (~120 ^oC) and a high vapor pressure (7.5 Torr at 80 ^oC). During deposition, liquid precursor was transported to the evaporator with dry helium at a flow rate of 0.03 ml/min and evaporated at 95 ºC. The evaporated precursor was mixed with 200 sccm helium carrier gas and delivered to the reactor through a line heated to 105 ºC. Oxidants flowed into the chamber through the downstream microwave plasma applicator at the rate

of 100 sccm. The oxidants studied were oxygen, an oxygen/helium mixture, nitrous oxide, and a nitrous oxide/nitrogen mixture. The ratios of oxygen/helium and nitrous oxide/nitrogen mixtures were changed from 100 sccm/0 sccm to 10 sccm/90 sccm but the flow rate of all oxidant mixtures was 100 sccm. Reactor pressure was maintained at 2 Torr. Deposition temperatures ranged from 250 ºC to 390 ºC. The deposition time was 10 minutes. For comparison, MOCVD was performed on the same configuration without applying microwave power.

Film Thickness Measurement

A Woollam Variable Angle Spectroscopic Ellipsometer (VASE) was used for film thickness measurements. The spectral range was from 700 nm to 1200 nm at an angle of 75°.

Crystallinity Measurements

X-ray diffraction patterns were collected on an X-Pert MRD Panalytical Diffractometer; the experimental configuration has been discussed previously. A Grazing Incidence X-ray Diffraction (GIXRD) geometry was used to enhance the diffraction intensity for crystallinity characterization of the deposited thin films. Use of a multiplayer parabolic mirror allowed the divergent incident X-ray beam to be converted into an intense monochromatic parallel beam. The parallel incident beam irradiated the sample at a grazing angle fixed at 1.0°, while a proportional detector scanned over 2θ. In order to preserve the parallel beam geometry, a 0.27 degrees parallel plate collimator and a 0.04 rad. soller slits were inserted before the detector. The measurements were carried out using CuKα radiation.

Composition and Interface Measurements

Composition measurements of the films were performed on a PHI 1600/3057 X-ray Photoelectron Spectrometer (XPS) with a standard aluminum x-ray source. For high-resolution scans, the pass energy was 46.95 eV, step size was 0.025 eV, and the scan time for each step was 100 sec. Typically, 30 seconds of sputtering was performed with an Ar ion gun at 2 KeV and 20 mA prior to XPS measurements. To perform the interfacial composition and bonding measurements, the as-deposited films were etched in 0.25% HF solutions to less than 10 nm in thickness.

Electrical Characterization

Electrical properties of the hafnium oxynitride films were measured using MIS capacitor structures. Films were deposited onto p-type (100) silicon wafers with low (< 0.01 ohm-cm) resistivity. A blanket aluminum film with thickness ~ 300 nm was sputtered onto the wafer backside and circular platinum electrodes with 1.8 mm diameter (~200 nm thickness) were sputtered onto the hafnium oxynitride films through a shadow mask. Capacitance-voltage (C-V) analyses were conducted on a Keithly 550 CV analyzer and current–voltage (I-V) analyses were performed with a Hewlett Packard 4156A Precision Semiconductor Analyzer. C-V measurements were performed at 100 kHz and the sweep voltage range was -5 V to +5 V.

Thermal Stability

To determine if the films deposited by O_2 and N_2O MOCVD are thermally stable to the temperatures typically used in microelectronic device fabrication, deposited films were annealed by rapid thermal processing (RTP) at 900 ºC under N_2 protection. During the RTP process, the temperature was raised to 900 ºC in 10 seconds and held at that

temperature for 10 seconds; the furnace was then cooled down to room temperature in 2.5 minutes. The annealed films were characterized by GIXRD and their morphologies compared with those of samples prior to annealing.

Results and Discussion

Deposition Rate

Effect of Deposition Temperature

With the precursor flow rate at 0.03 ml/min, the helium carrier gas flow rate 200 sccm, the oxidant (O_2 or N_2O) flow rate 100 sccm, and the microwave power 450 watts, downstream microwave plasma enhanced depositions were performed at four temperatures: 250 ºC, 300 ºC, 350 ºC, 390 ºC. The deposition rates change with temperature as shown in Figure 4.1.

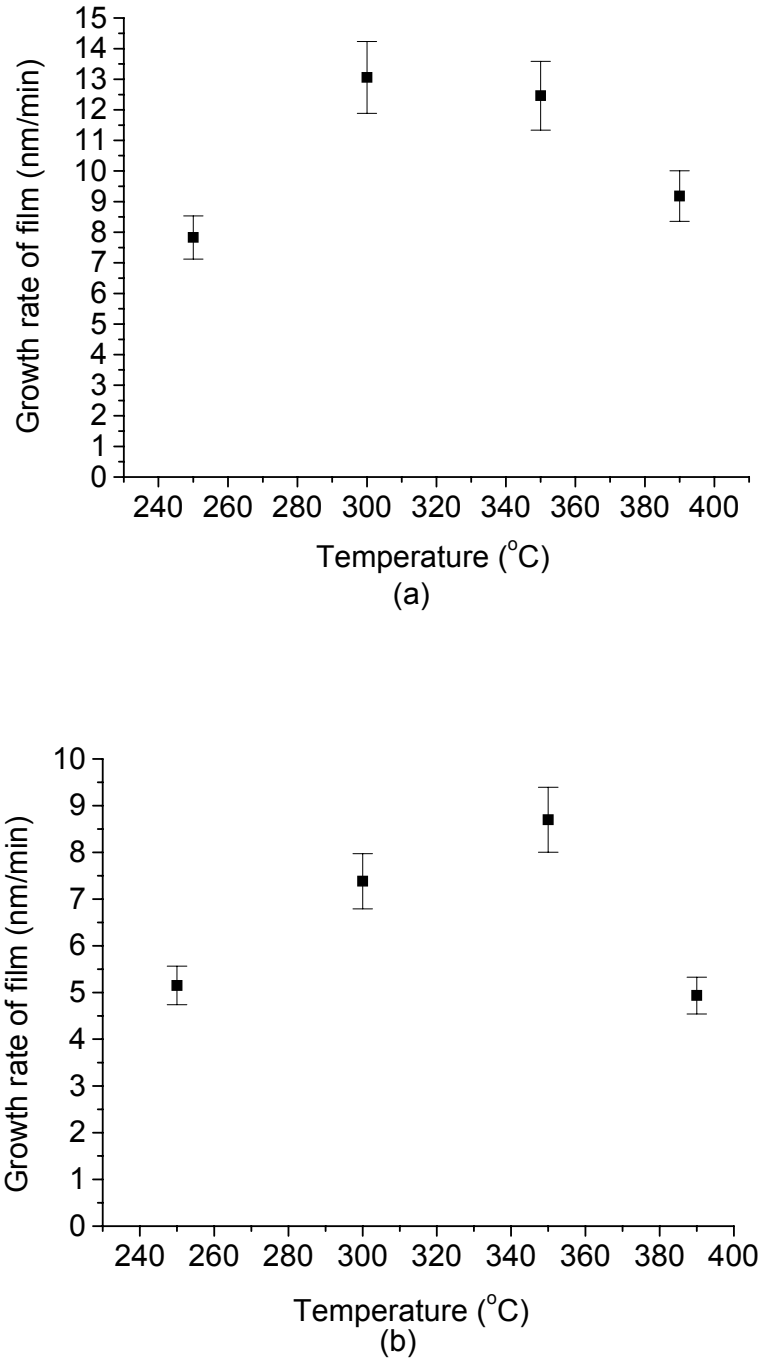

Figure 4.1 Plots of deposition rates vs temperatures for (a) O_2 PECVD and (b) N_2O PECVD.

For O_2 plasma deposited films, deposition rates increase with temperature when the temperature is below 300 ºC; above 300 ºC, deposition rates fall with increasing temperature. Deposition rates for PECVD depend on three individual processes [30]: the generation rate of short lifetime reactant species formed by gas phase thermal or plasma activation ($TDEAH^*$), adsorption/desorption of reactant species on the substrate surface, and surface reaction. These processes can be expressed as:

TDEAH + heat or radicals (O^*, O_2^* et c) $\rightarrow$ $TDEAH^*$ (activation)

$TDEAH^* \leftrightarrow$ TDEAH(s) (adsorption/desorption)

O^*, O_2^* et c $\leftrightarrow$ O(s), O_2(s), et c

TDEAH(s) + O(s), O_2(s), et c + heat $\rightarrow$ Hafnium oxynitride (surface reaction)

In a parallel plate plasma reactor or a microwave plasma reactor configuration with line-of-sight between the plasma source and the substrate (i.e., with no sharp bends in the connecting tubing), electron impact reactions produce O^*, O_2^*, O^-, O^+, O_2^+ and electrons by reactions such as [31]:

$$e + O_2 \rightarrow O_2^* + e$$

$$e + O_2 \rightarrow O^- + O^+ + e$$

$$e + O_2 \rightarrow 2\,O + e$$

$$e + O_2 \rightarrow O_2^+ + 2e$$

$$e + O_2 \rightarrow O + O^+ + 2e$$

$$e + O \rightarrow O^* + e$$

However, in a downstream plasma reactor, few if any ions or electrons can be introduced into the reaction chamber because of recombination reactions. Only O^* and O_2^* are the activated short lifetime reactant species introduced into the chamber.

In general, gas phase reactive species generation rates, surface reaction rates and desorption rates of the intermediate species on the substrate surface increase with temperature. The net effect of the competing processes determines the deposition rate. As indicated in Figure 4.1a, at low temperatures, the surface reaction process dominates the overall deposition rate so that the net deposition rate increases with temperature. When the deposition temperature is higher than 300 ºC, adsorption/desorption rates dominate the net deposition rate so that in the high-temperature regime, increasing temperatures lead to higher desorption rates and thus lower film deposition rates. That is, the effective activation energy in the high temperature region is negative. Compared with MOCVD results [32, 33], the deposition rates with PECVD are higher and the negative activation energy region appears at much lower temperature. Such comparisons indicate that the microwave plasma assists dissociation of oxygen and thus the generation of the intermediate species and surface reactions [34]. That is, the plasma supplies energy for bond breaking that otherwise would be supplied by thermal means.

As shown in Figure 4.1b, the deposition rate versus temperature for N_2O plasma enhanced deposition of hafnium oxynitride films displays similar trends to that of O_2 plasma enhanced depositions, although the negative activation energy region occurs at slightly higher temperature (> 350 ºC). Such results from depositions with plasma-activated/dissociated N_2O as the oxidant species can be explained by the similar way to that used for depositions with O_2 plasma although the plasma dissociated N_2O atmosphere may contain activated nitrogen species [35, 36]. The following simplified set of elementary reactions is representative of the N_2O plasma chemistry [35, 37, 38]:

$$e + N_2O \rightarrow N_2 + O + e$$

$$O + e \rightarrow O^* + e$$

$$N_2O + O^* \rightarrow 2NO$$

$$N_2O + O^* \rightarrow N_2 + O_2$$

$$O + O \rightarrow O_2$$

$$e + O_2 \rightarrow O_2^* + e$$

$$e + N_2 \rightarrow N_2^* + e$$

$$e + NO \rightarrow NO^* + e$$

In the downstream plasma system, only neutral molecules and radicals are introduced into the deposition chamber.

Effects of Microwave Power

Figure 4.2 shows the trends of O_2 plasma- and N_2O plasma-enhanced deposition rates upon variation of microwave power between 150 W and 450 W. From the figure, it can be concluded that deposition rates do not change significantly with microwave power over the range investigated. These observations suggest that the concentration of oxygen radicals does not increase substantially with microwave power in the range of 150 - 450 W with the other deposition conditions unchanged.

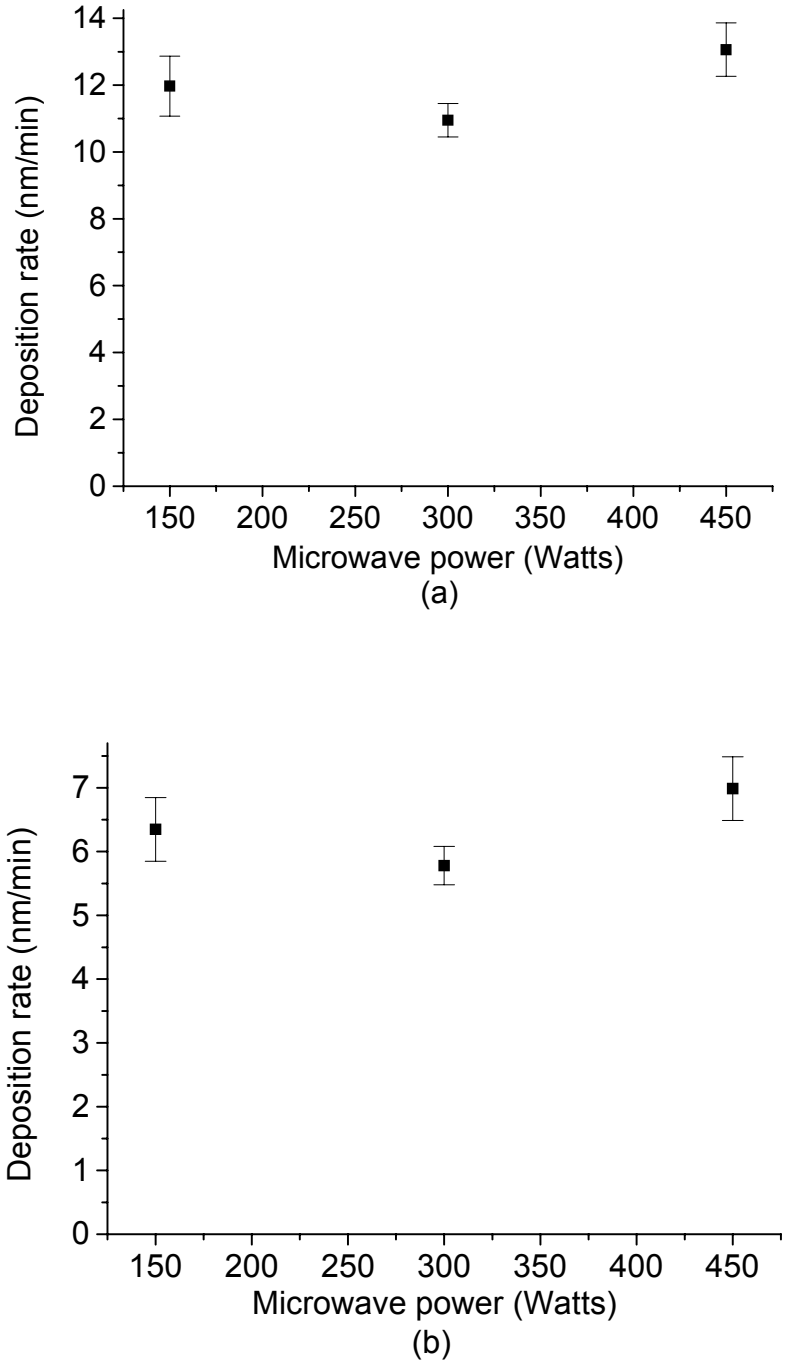

Figure 4.2 Deposition rate vs microwave power for (a) O_2 PECVD and (b) N_2O PECVD. Temperatures are 300 ^oC and 390 ^oC for (a) and (b) respectively.

Effects of O_2/He Ratio or N_2O/N_2 Ratio

When the O_2/He ratio or N_2O/N_2 ratio changes from 100/0 to 10/90 while other parameters remain constant (substrate temperature 350 ºC, oxidant gas mixture flow rate 100 sccm, He carrier gas flow rate 200 sccm, precursor flow rate 0.03 ml/min, chamber pressure 2 Torr, microwave power 450 Watts), film deposition rates decrease as shown in Figure 4.3. The reduction in deposition rate occurs because of the reduced concentration of oxygen radicals introduced into the chamber.

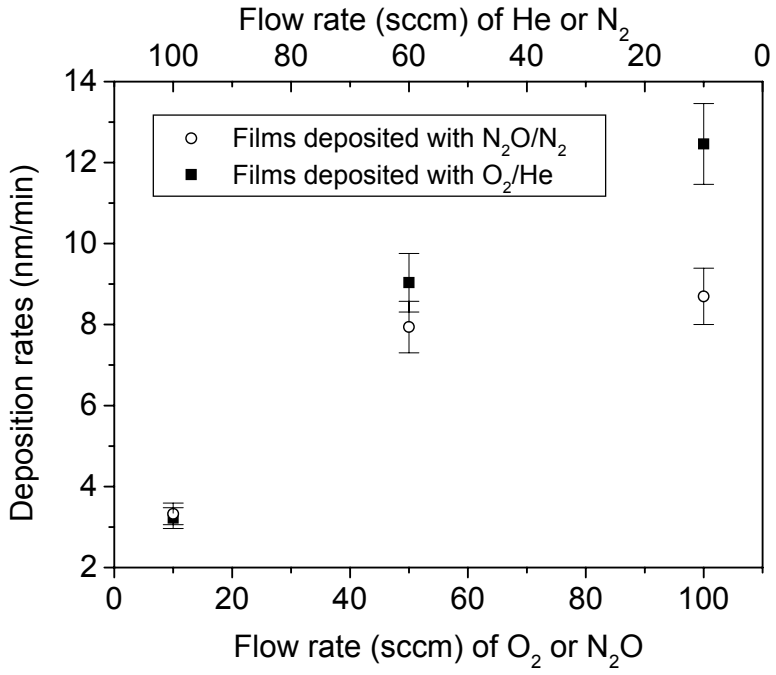

Figure 4.3 Deposition rate vs O_2/He ratio or N_2O/N_2 ratio. Temperature is fixed at 350 ^oC.

Film Morphology

Morphologies of the PECVD films deposited in different oxidants have been investigated by GIXRD at an incident angle of 1º; GIXRD patterns are shown in Figure 4.4 and 4.5. GIXRD measurements on all films deposited in O_2 plasmas, N_2O plasmas,

O_2/He plasmas and N_2O/N_2 plasmas indicate amorphous morphologies. There is a broad reflection ~32^o in all GIXRD patterns, which demonstrates that the hafnium oxynitride films deposited by downstream microwave plasma-assisted deposition are amorphous to the detection limit of GIXRD (<2.0 nm crystallite size) within the deposition temperature range of 250 ºC – 390 ºC. Although the film compositions (both bulk and interface) vary in a small range (discussed in the next section) with different O_2/He or N_2O/N_2 ratios, all films are amorphous.

For comparison, hafnium oxynitride films deposited by MOCVD with oxygen as the oxidant are amorphous; a typical GIXRD pattern is shown in Figure 4.6. All deposition parameters for the MOCVD process were the same as those of the PECVD process except that no microwave power was applied. We have previously shown that the hafnium oxynitride GIXRD pattern shown in Figure 4.6 is characteristic of the cubic phase [32]; Bragg reflection indices are shown in the figure. These results illustrate that the PECVD favors the formation of amorphous hafnium oxynitride films, as desired for IC devices due to the resulting improved dopant diffusion barrier properties [39].

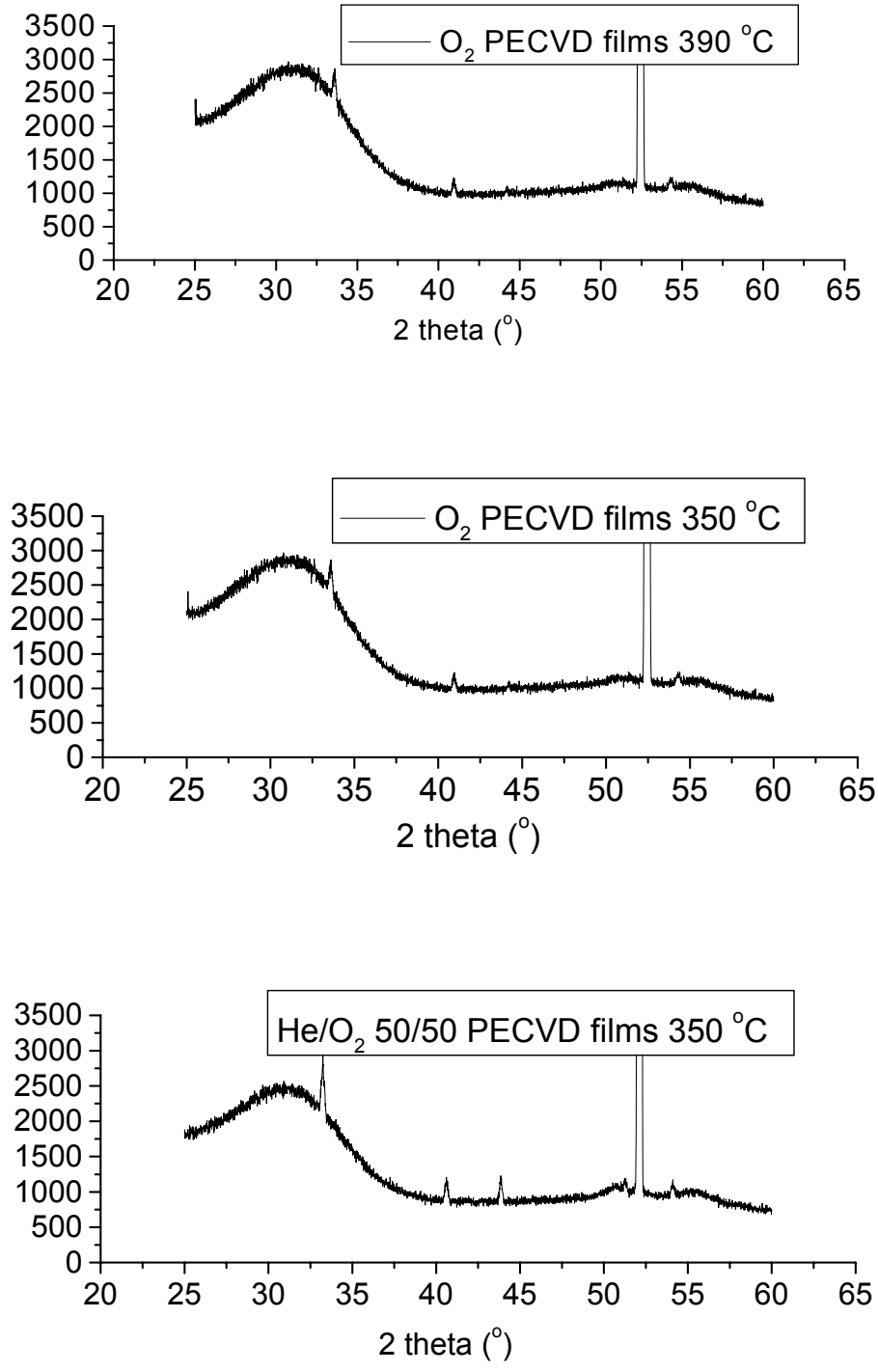

Figure 4.4 GIXRD patterns of hafnium oxynitride films deposited by PECVD in O_2 and O_2/He.

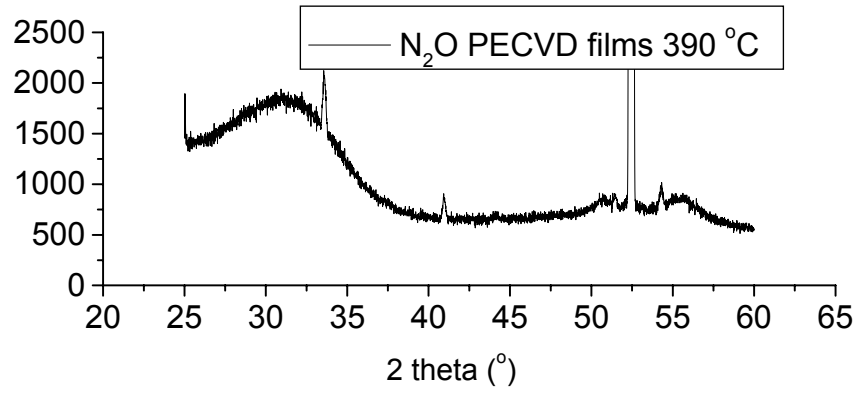

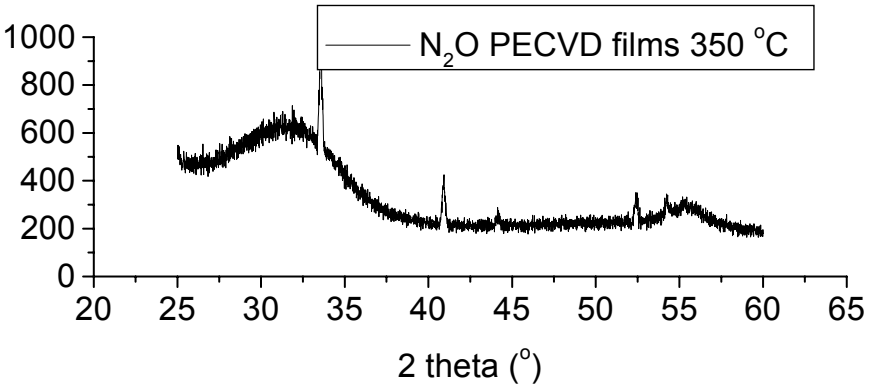

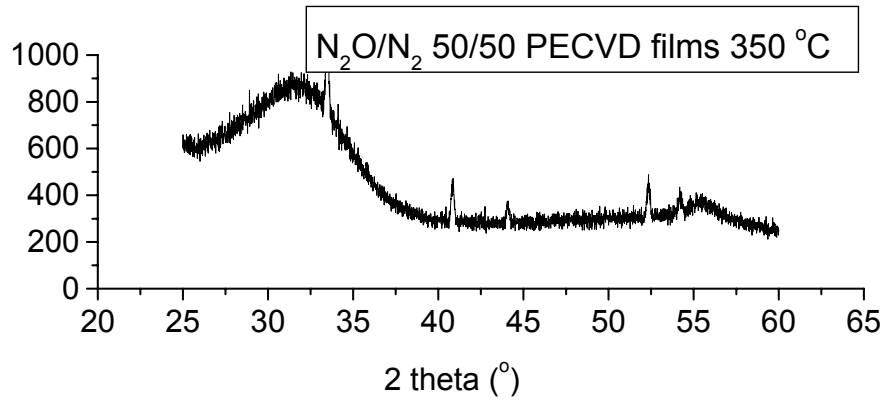

Figure 4.5 GIXRD patterns of hafnium oxynitride films deposited by PECVD in N_2O and N_2O/ N_2.

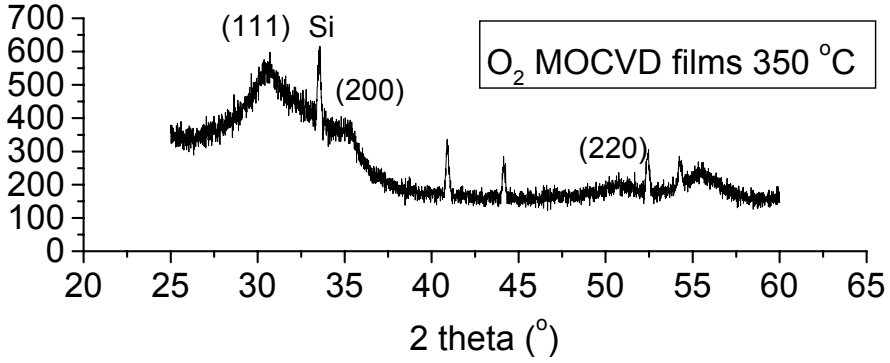

Figure 4.6 GIXRD pattern of the film deposited by O_2 MOCVD.

There are two primary reasons for the formation of amorphous films by PECVD; these relate to two important steps in the PECVD process as shown in Figure 4.7. First, as discussed in the deposition rate section, the application of a downstream microwave plasma increases the activated oxidant metastable concentration and thus accelerates gas phase reactions of precursors. Because of the large concentration of oxygen radicals present, intermediate species ($TDEAH^*$) produced by the gas phase reactions contain more oxidized moieties such as HfO, and Hf_2O_3-like species. The highly oxidized HfO or Hf_2O_3-like species can form a hafnium oxide network rapidly at the substrate surface, thereby minimizing the time for surface diffusion and crystallization [23][40]. Secondly, the plasma activated free radicals have large sticking coefficient on the substrate surface so that surface diffusion is again inhibited and nucleation/growth of crystallites is diminished [41].

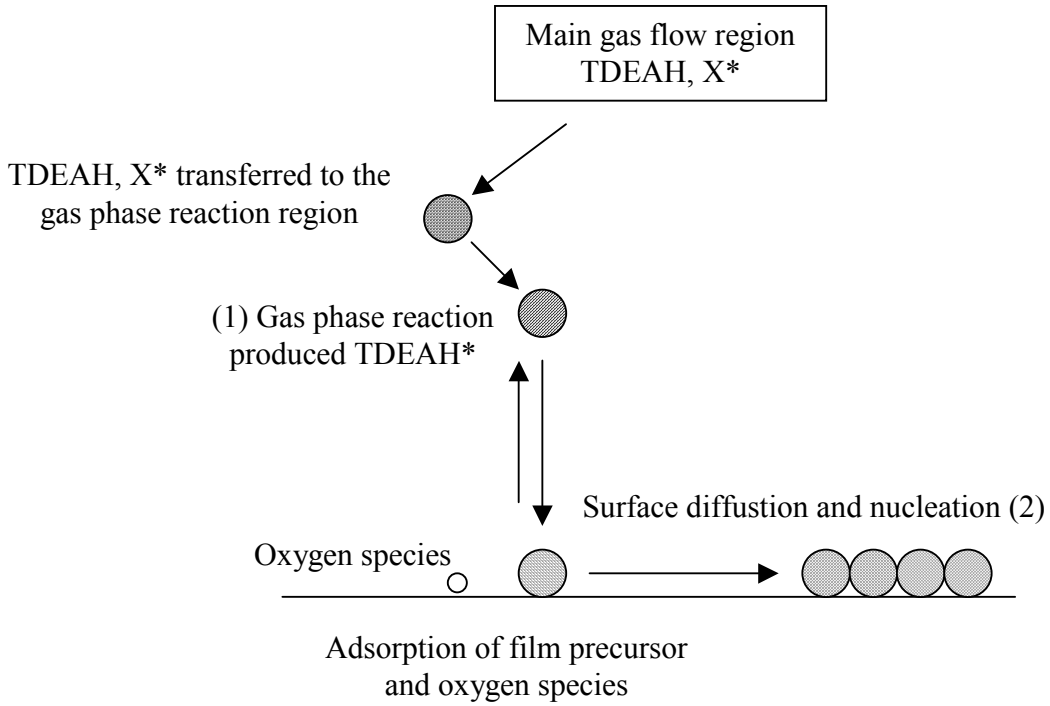

Figure 4.7 Process scheme in PECVD.

Film Composition

Bulk Composition

The bulk composition of films deposited by PECVD in different oxidants has been characterized by XPS. The atomic percentages of all elements are obtained after 30 sec of Ar ion sputtering at 2 KeV and 20 mA. Figure 4.8 shows the O/Hf ratios in films deposited by O_2 or N_2O PECVD at different temperatures. All films formed by PECVD have an O/Hf ratio of at least 2.2 (range of 2.2-2.7) while all films formed by O_2 MOCVD have an O/Hf ratio of essentially 2.0 (range 1.6 – 2.1). Apparently, films deposited by PECVD have a higher than stoichiometric amount of oxygen. The extra oxygen atoms are believed to be incorporated into the oxide structure as interstitials [34].

As Figure 4.9 indicates, there are many interstitial sites in fluorite lattice for the incorporation of excess oxygen [42]. Because it is easier for oxygen atoms than oxygen molecules to be incorporated as interstitial atoms [43], plasma enhanced dissociation of oxygen and nitrous oxide can promote the incorporation of interstitial atoms. After the incorporation of interstitials atoms, the ordered lattice of fluorites will be distorted, which can assist to explain the formation of amorphous films deposited by PECVD.

Because the distance between hafnium atoms and interstitial oxygen atoms is different from the normal Hf – O bond length, bonding environments for both O and Hf atoms in non-stoichiometric films are more varied. That is, as shown in Tables 4.2 and 4.3, the O1s peaks and Hf4f peaks in XPS spectra of films from PECVD are broadened relative to those in spectra of films from O_2 MOCVD; these results suggest the presence of interstitial oxygen atoms [44]. The full width at half maximum (FWHM) broadening is reduced at higher temperatures, which indicates that the interstitial oxygen atom concentration is reduced or is more uniformly distributed at high temperatures.

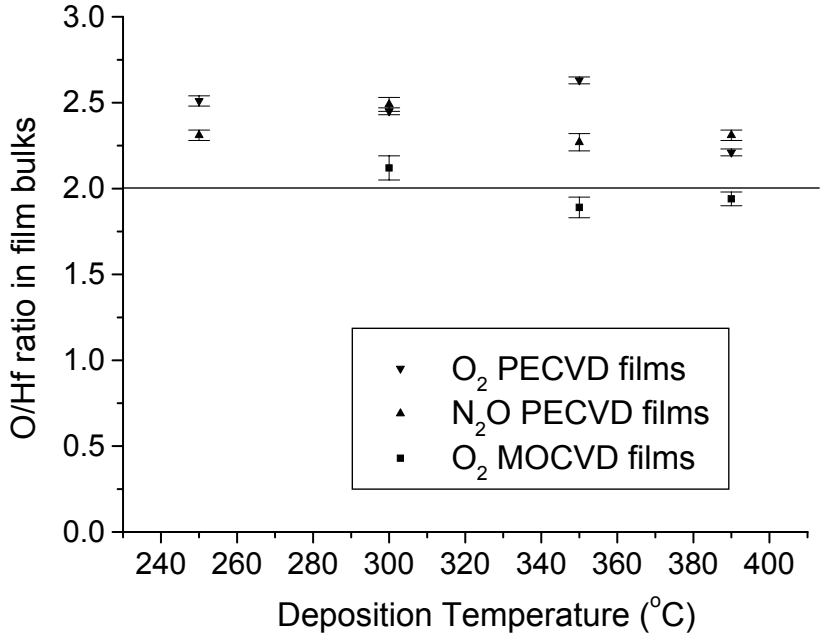

Figure 4.8 O/Hf ratio in hafnium oxynitride films deposited at different temperatures and in different oxidants.

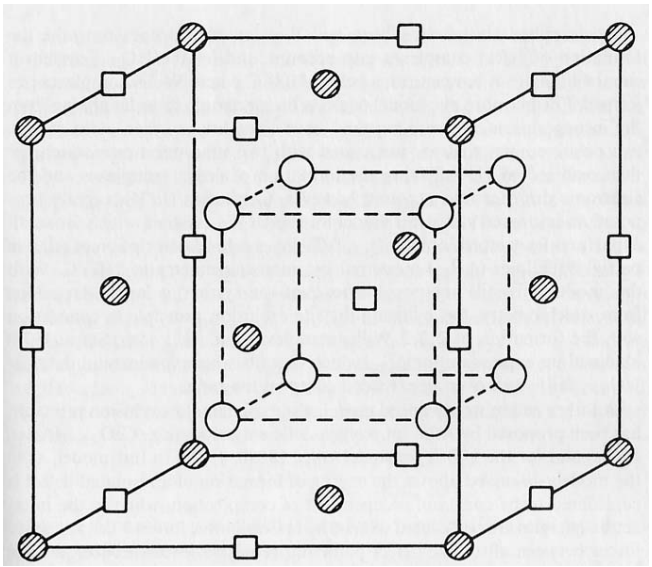

Figure 4.9 Interstitial sites (represented by empty squares) in fluorite lattice of HfO_2 available for incorporation of excess oxygen. Solid circles represent hafnium sites; open circles represent oxygen sites [42].

Table 4.2 FWHM of XPS O1s peaks for as-deposited films (bulks) deposited in O_2 MOCVD, O_2 PECVD and N_2O PECVD at different temperatures.

Temperature (^oC)	250	300	350	390
O_2 MOCVD	N/A	1.57 eV	1.72 eV	1.62 eV
O_2 PECVD	2.49 eV	1.96 eV	1.81 eV	1.67 eV
N_2O PECVD	2.58 eV	2.43 eV	2.39 eV	2.05 eV

Table 4.3 FWHM of XPS Hf4f (combination of Hf4f5/2 and Hf4f7/2) peaks for as-deposited films (bulks) deposited in O_2 MOCVD, O_2 PECVD and N_2O PECVD at different temperatures.

Temperature (^oC)	250	300	350	390
O_2 MOCVD	N/A	2.86 eV	3.05 eV	2.96 eV
O_2 PECVD	3.44 eV	3.1 eV	3.08 eV	2.97 eV
N_2O PECVD	3.58 eV	3.21 eV	3.39 eV	3.22 eV

Additional confirmation of these conclusions is obtained from the Hf4f peak positions in the XPS spectra. As shown in Figure 4.10, XPS Hf4f peaks consist of Hf4f5/2 and Hf4f7/2 peaks. Each of the Hf4f5/2 and Hf4f7/2 peaks can be deconvoluted into two peaks. For films deposited by PECVD (Figure 4.10), the overlap of Hf4f5/2 and Hf4f7/2 peaks is significant; this result is consistent with significant concentration of Hf-O (interstitial) bonds in deposited films.

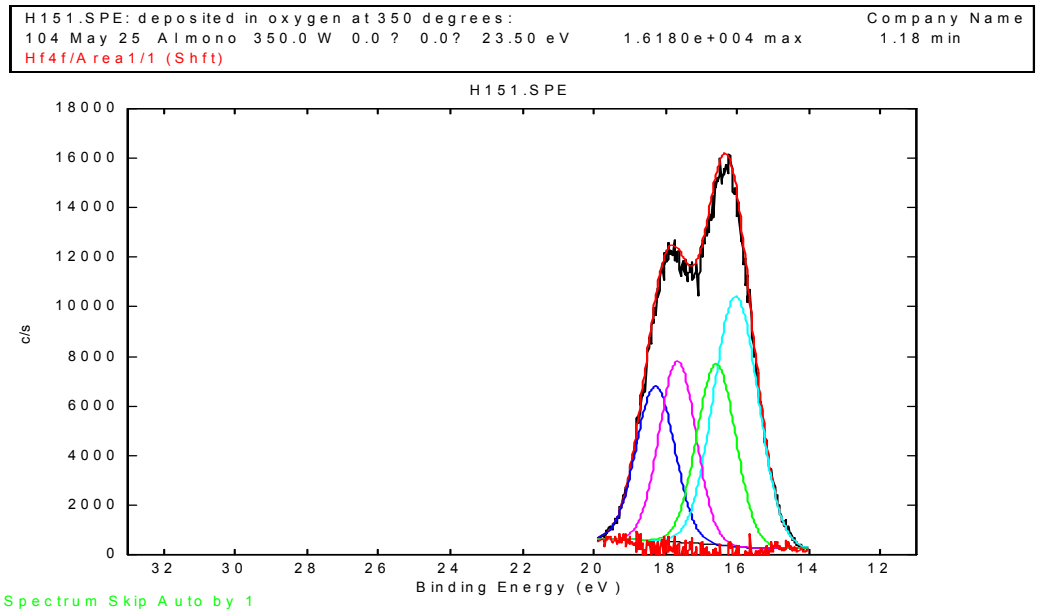

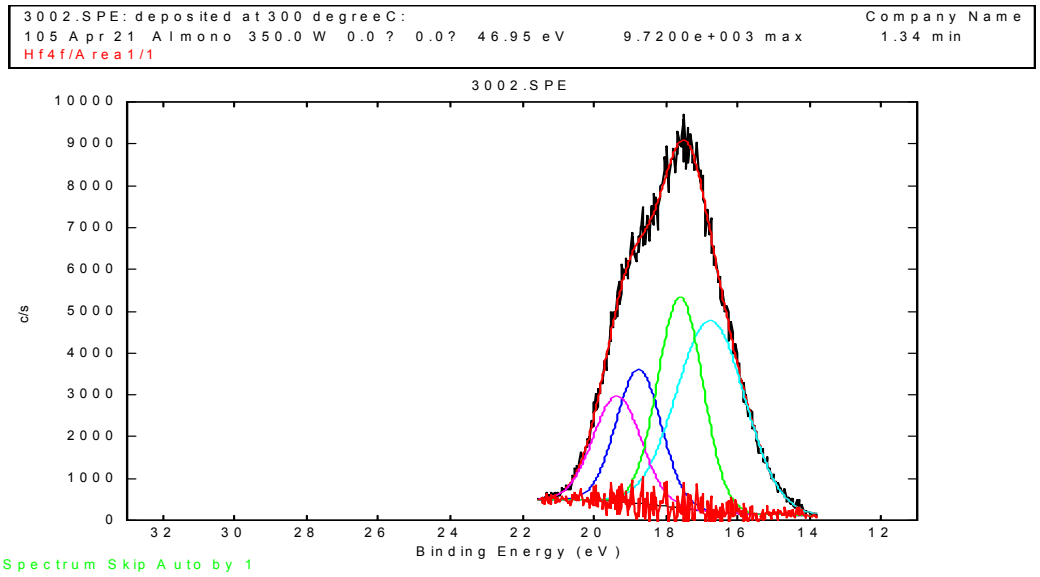

Figure 4.10 Deconvoluted Hf4f peaks in films from O_2 MOCVD (top) and O_2 PECVD (bottom).

The positions of deconvoluted peaks are listed in Table 4.4. For films deposited by PECVD, all peaks shift to higher binding energy compared to the analogous peaks in films from MOCVD. The shifts can also be attributed to the interstitial oxygen atoms. The shift is more significant for films deposited by N_2O PECVD, indicating that N_2O PECVD can introduce more interstitial oxygen atoms into deposited films than can O_2 PECVD.

Table 4.4 Deconvoluted XPS Hf4f peak positions in films deposited from O_2 MOCVD, O_2 PECVD and N_2O PECVD.

Band position	Band 1 (eV)	Band 2 (eV)	Band 3 (eV)	Band 4 (eV)
O_2 MOCVD	18.28	17.66	16.58	16.03
O_2 PECVD	18.57	18.02	17.03	16.21
N_2O PECVD	19.35	18.75	17.59	16.75

The nitrogen content of these films is shown as a function of deposition temperature in Figure 4.11; apparently little variation (0.5-1.5 atomic %) is observed under the conditions investigated.

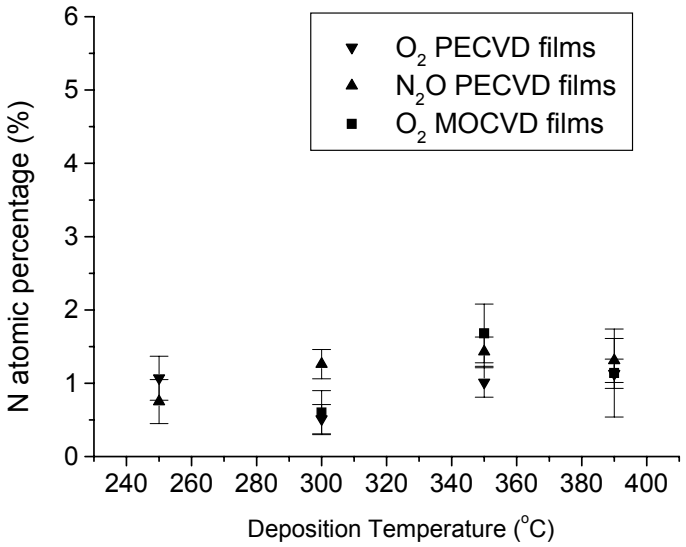

Figure 4.11 N atomic percentages in as-deposited films (bulk) deposited at different temperatures.

For the films deposited by O_2/He and N_2O/N_2 PECVD, reducing the O_2/He ratio or N_2O/N_2 ratio slightly reduces the O/Hf ratio in deposited films although the ratio remains larger than two. The XPS results indicate that the plasma-activated oxidants promote the incorporation of oxygen atoms into the deposited hafnium oxynitride films, which is consistent with previous studies [45]. A change in the deposition temperature can alter the oxygen amount incorporated or the distribution.

Hafnium Oxynitride/Silicon Interface Composition

In order to characterize the composition of hafnium oxynitride/silicon interfaces by XPS, as-deposited films are etched in 0.25 % HF solutions until the thickness of the etched films is ~7-8 nm. The films deposited by O_2 or N_2O PECVD at 350 ^oC have etch rates of 33 nm/min or 25 nm/min respectively, which are much higher than the etch rates

of crystalline films [20] because of their amorphous nature. The thickness profiles that results from etching are shown in Figure 4.12.

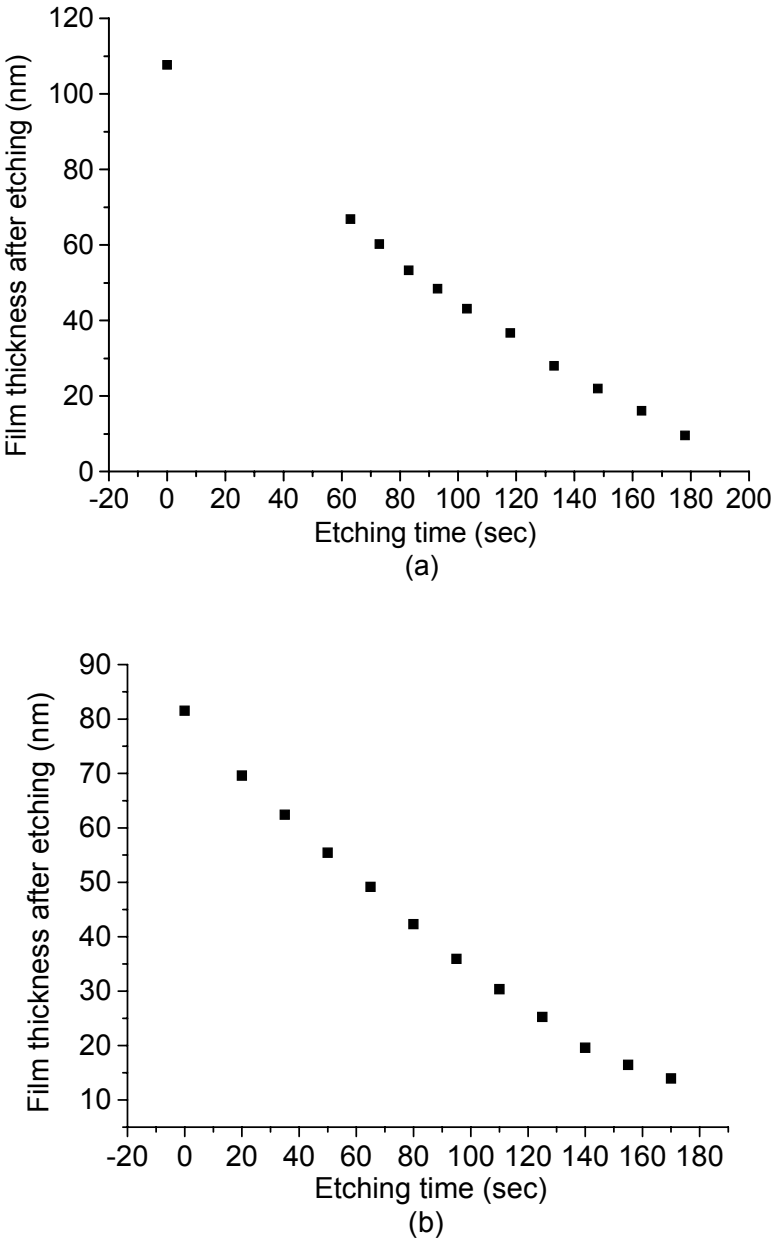

Figure 4.12 Etching profiles of films deposited by O_2 PECVD (a) and N_2O PECVD (b). Films were etched in a 0.25% HF solution.

XPS spectra of the etched films show that the interface compositions of all films deposited by PECVD are HfSixOyNz. As Figure 4.13 shows, the nitrogen atomic percentages of film interfaces are in the range of 1.5 % - 5.5 %, which is higher than that in the film bulk. These results indicate that nitrogen atoms accumulate at the interface between the hafnium oxynitride films and the silicon substrates. For films deposited by N_2O PECVD, interface nitrogen contents are smaller than those of films deposited by O_2 PECVD. Such observations are consistent with the discussion in the previous section that suggests that a higher concentration of oxygen radical is produced by N_2O PECVD than by O_2 PECVD. These results indicate that N_2O PECVD is a good source for oxygen radicals but not an efficient method to introduce nitrogen atoms into high-k films. Also, as shown in Table 4.2, the O1s FWHMs of films from O_2 or N_2O PECVD decrease with increasing temperature. Therefore, it is possible that oxygen atoms at the interface can be reduced in concentration or more uniformly distributed throughout the films due to high temperature heat treatments.

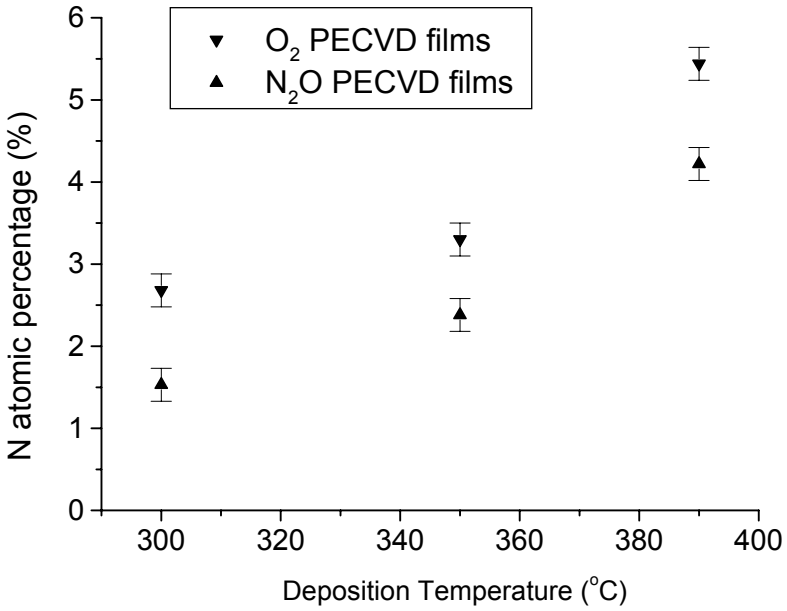

Figure 4.13 N atomic percentages of HF etched films (interfaces) deposited at different temperatures. Thicknesses of etched films are ~7-8 nm.

Electrical Properties

The dielectric constant and leakage current of the deposited films have been characterized by CV and IV measurements on MOS structures; dielectric constants calculated from accumulation capacitance values are listed in Table 4.5. With an increase in deposition temperature, the dielectric constants of the deposited films increase. This trend is due to higher film densities, perhaps because fewer oxygen interstitials are incorporated higher film densities at higher deposition temperatures. The average oxide charge (interface states and charge) density of the films is estimated from the flatband shift of CV curves according to the expression $Q_{ox} = C_i \Delta V_{fb} / q$ [33]; the resulting values are shown in Table 4.6. For these calculations, the Pt work function is 5.3 V and p-Si wafer doping density is 10^{19} /cm^3[46]. Table 4.6 shows that the defect densities of films

deposited in O_2 or N_2O PECVD are in the range of 1 - 4 $\times 10^{12}$, which are higher than those of films deposited in O_2 MOCVD [20]. These films also have relatively high leakage currents that are between 10^{-5} and 10^{-6} A/cm^2 at an electrical field of 0.2 MV/cm. The increased oxide charge densities and leakage currents in O_2 or N_2O PECVD are likely due to the interstitial oxygen distorted bond structures at the hafnium oxynitride/silicon interfaces [45].

Table 4.5 Dielectric constants of films deposited by O_2 PECVD and N_2O PECVD at different temperatures.

Temperature (^{o}C)	250	300	350	390
O_2 PECVD	14.4	18.0	21.7	22.5
N_2O PECVD	15.0	16.6	20.9	22.6

Table 4.6 Oxide charge densities in the films deposited by O_2 PECVD and N_2O DMPECVD at different temperatures.

Temperature (^{o}C)	250	300	350	390
O_2 PECVD	2.08e12	1.61e12	1.37e12	6.3e11
N_2O PECVD	3.15e12	3.21e12	1.62e12	1.35e12

Thermal Stability

Films deposited by PECVD were annealed at 900 ^{o}C by RTP under the protection of N_2; after RTP annealing, films were characterized by GIXRD again. GIXRD patterns of annealed films (deposited at 350 ^{o}C) are shown in Figure 4.14.

Although both as-deposited films were amorphous, RTP annealed films show obvious crystalline phases. Both tetragonal and monoclinic phases are detected from the GIXRD measurements. Based on the GIXRD patterns, films deposited by N_2O PECVD contain a higher fraction of tetragonal phase after annealing than do films deposited by O_2 PECVD, which suggests that more interstitial oxygen atoms promote the formation of tetragonal crystallites after high temperature annealing. Furthermore, these results illustrate that the amorphous films deposited by PECVD are unstable to high temperature annealing. In order to introduce amorphous films deposited under the current conditions by PECVD into microelectronic fabrication sequences, high temperature annealing should be avoided.

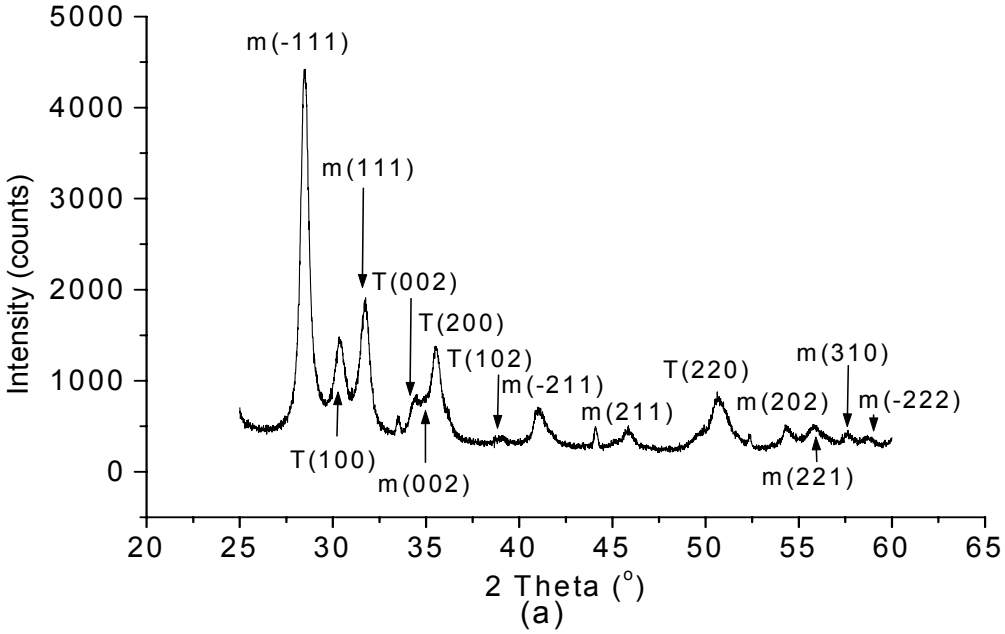

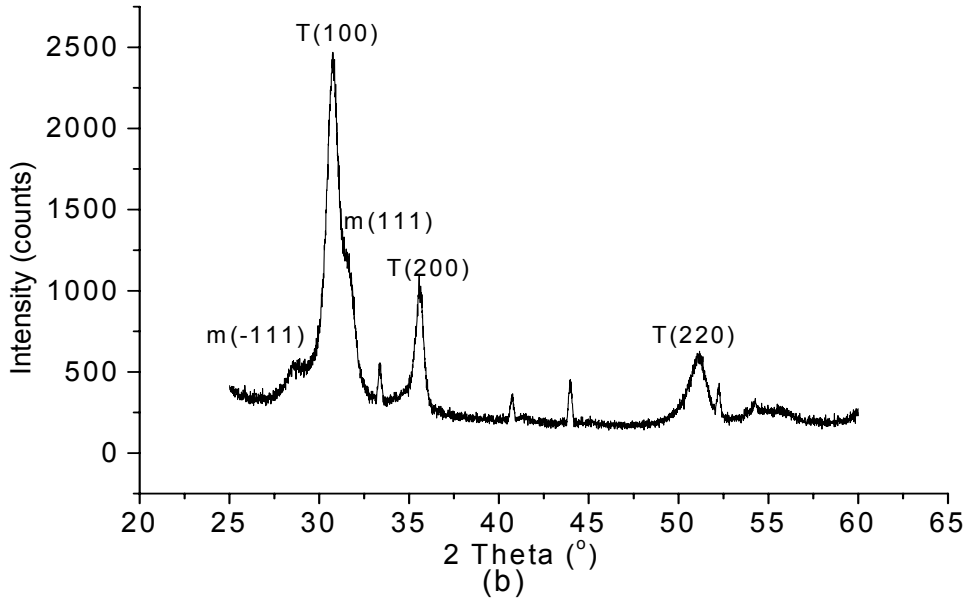

Figure 4.14 GIXRD patterns of 900 °C RTP annealed films deposited by O_2 PECVD (a) and N_2O PECVD (b) respectively.

Conclusions

Hafnium oxynitride films were deposited in downstream microwave plasma dissociated oxidants (O_2, N_2O, O_2/He, N_2O/N_2). At high temperatures (>350 ^oC), plasma enhanced depositions display negative activation energies. Oxygen radicals from downstream microwave plasma dissociated oxidants promote gas phase reaction of hafnium oxynitride precursors and reduce surface diffusion on substrates that lead to amorphous deposited films. The deposited films contain an excess amount of oxygen that appears to be incorporated as interstitial atoms. Interstitial oxygen atoms distort bond structures in the hafnium oxynitride network and introduce trap levels at the film/substrate interface. Higher deposition temperatures can reduce the interstitial oxygen or promote more uniform distributions that improve the electrical properties of films. Films deposited at higher temperatures also have larger dielectric constants due to their larger densities. N_2O PECVD can provide large amount of oxygen atoms for deposition processes but cannot efficiently introduce nitrogen atoms into deposited films. N_2O PECVD is able to introduce more interstitial oxygen atoms than is O_2 PECVD. Furthermore, reducing oxidant flow rates by changing O_2/He or N_2O/N_2 ratios has no obvious effects on the deposited films. The amorphous films deposited by PECVD are unstable to 900^oC RTP annealing; the annealed films contain tetragonal and monoclinic phases. Films deposited by N_2O PECVD contain a higher fraction of the tetragonal phase after annealing than do films deposited by O_2 PECVD.

REFERENCE

1. Maiti, C.K., Dalapati, G.K., Chatterjee, S., Samanta, S.K., Verma, S., and Patil, S., Solid-State Electron., 2004. **48**: p. 2235.
2. Albertin, Pereyra, I., and Alayo, M.I., Mater. Characterization, 2003. **50**: p. 149.
3. Zenasni, A., Raynaud, P., Sahli, S., Rebiai, S., and Segui, Y., Surf. and Coating Tech., 2003. **174-175**: p. 162.
4. Yamamoto, K., Asai, M., Horii, S., Miya, H., and Niwa, M., J. Vac. Sci. Technol. A, 2003. **21**: p. 1033.
5. Niu, D., Ashcraft, R.W., Chen, Z., Stemmer, S., and Parsons, G.N., J. Electrochem. Soc., 2003. **150**: p. F102.
6. Nishisaka, M. and Asano, T., Mater. Sci. in Semi. Processing, 2005. **8**: p. 225.
7. Carreno, M.N.P., Bottecchia, J.P., and Pereyra, I., Thin Solid Films, 1997. **308-309**: p. 219.
8. Albertin, K.F. and Pereyra, I., Microelectronic Engineering, 2005. **77**: p. 144.
9. Bae, C. and Lucovsky, G., Appl. Surf. Sci., 2004. **234**: p. 475.
10. Ray, S.K., Maiti, C.K., Lahiri, S.K., and Chakrabarti, N.B., J. Vac. Sci. Technol. B, 1992. **10**: p. 1139.
11. Chayani, M., Caquineau, H., Despax, B., Bandet, J., and Berjoan, R., Thin Solid Films, 2005. **471**: p. 53.
12. Bera, L.K., Mukhopadhyay, M., Ray, S.K., Nayak, D.K., Usami, N., Shiraki, Y., and Maiti, C.K., Appl. Phy. Lett., 1997. **70**: p. 217.
13. Kang, S.C., Oh, C.H., Lee, N.E., and Kwon, T.K., Surf. and Coating Tech., 2005. **193**: p. 350.

14. Cubaynes, F.N., Venezia, V.C., Marel, C.V., Snijders, J.H.M., Everaert, J.L., Shi, X., Rothschild, A., and Schaekers, M., Appl. Phy. Lett., 2005. **86**: p. 172903.

15. Mukhopadhyay, M., Ray, S.K., and Maiti, C.K., Electron. Lett., 1995. **31**: p. 1953.

16. Ohshima, I., Cheng, W., Ono, Y., Higuchi, M., Hirayama, M., Teramoto, A., Sugawa, S., and Ohmi, T., Appl. Surf. Sci., 2003. **216**: p. 246.

17. Ng, C.H., Chew, K.W., and Chu, S.F., IEEE Electron Dev. Lett., 2003. **24**: p. 506.

18. Wang, J.C., Shie, D.C., Lei, T.F., and Lee, C.L., Electrochemical and Solid-State Letters, 2003. **2003**: p. F34.

19. Beck, R.B., Giedz, M., Wojtkiewicz, A., Kudla, A., and Jakubowski, A., Vacuum, 2003. **70**: p. 323.

20. Chang, S.J., Lee, J.S., Chen, J.F., Sun, S.C., Liu, C.H., Liaw, U.H., and Huang, B.R., IEEE Electron Dev. Lett., 2002. **23**: p. 643.

21. He, G., Fang, Q., Liu, M., Zhu, L.Q., and Zhang, L.D., J. Crys. Growth, 2004. **268**: p. 155.

22. Saito, K., Jin, Y., and Shimada, M., J. Electrochem. Soc., 2004. **151**: p. G328.

23. Choi, K.J., Kim, J.H., Yoon, S.G., and Shin, W.C., J. Vac. Sci. Technol. B, 2004. **22**: p. 1755.

24. Bhandari, H.B., Chen, P., and Klein, T.M. in *Integration of Advanced Micro- and Nanoelectronic Devices - Critical Issues and Solutions*. 2004.

25. Chen, P., Bhandari, H.B., and Klein, T.M., Appl. Phy. Lett., 2004. **2004**: p. 1574.

26. Choi, K.J., Kim, J.H., and Yoon, S.G., J. Electrochem. Soc., 2004. **151**: p. G262.

27. Losurdo, M., Giangregorio, M.M., Luchena, M., Capezzuto, P., Bruno, G., Barreca, D., Gasparotto, A., and Tondello, E. *Mat. Res. Soc. Symp. Proc.* 2004.

28. Lao, S.X., Martin, R.M., and Chang, J.P., J. Vac. Sci. Technol. A, 2005. **23**: p. 488.

29. Mays, E.L., Hess, D.W., and Rees, W.S., Journal of Crystal Growth, 2004. **261**: p. 309.

30. Pai, C.S. and Chang, C.P., J. Appl. Phys., 1990. **68**: p. 793.

31. Cho, B.O., Wang, J., and Chang, J.P., J. Appl. Phys., 2002. **92**: p. 4238.

32. Luo, Q., Cernatescu, I.D., Snyder, R.L., Rees, W.S., and Hess, D.W., J. Electrochem. Soc., 2005. **in press**.

33. Koukab, A., Bath, A., and Losson, E., Solid-State Electron., 1997. **41**: p. 635.

34. Kim, B.H., Ahn, J.H., and Ahn, B.T., Appl. Phy. Lett., 2003. **82**: p. 2682.

35. Khandelwal, A., Smith, B.C., and Lamb, H.H., J. Appl. Phys., 2001. **90**: p. 3100.

36. Cho, B.K., Wang, J., and Chang, J.P., J. Appl. Phys., 2002. **92**: p. 4238.

37. Smith, B.C., Khandelwal, A., and Lamb, H.H., J. Vac. Sci. Technol. B, 2000. **18**: p. 1757.

38. Zatsepin, D.V., Starikovskaya, S.M., and Starikovskii, A.Y., Plasma Phys. Rep., 2003. **29**: p. 555.

39. Robertson, J., Eur. Phy. J. Appl. Phys., 2004. **28**: p. 265.

40. Chang, C.P., Pai, C.S., and Hsieh, J.J., J. Appl. Phys., 1990. **67**: p. 2119.

41. Winters, H.F. *Plasma Chemistry III*. in *Topics in Current Chemistry*. 1980. New York: Springer-Verlag.

42. Alper, A.M., *Phase Diagrams: Materials Science and Technology*. Vol. 6-V. 1978, New York: Academic Press.

43. Foster, A.S., Gejo, F.L., Shluger, A.L., and Nieminen, R.M., Phys. Rev. B, 2002. **65**: p. 174117.

44. Bhandari, H.B., Chen, P., and Klein, T.M. *Materials Research Society Symposium Proceedings*. in *Integration of Advanced Micro- and Nanoelectronic Devices - Critical Issues and Solutions*. 2004.

45. Park, J., Cho, M., Kim, S.K., Park, T.J., Lee, S.W., Hong, S.H., and Hwang, C.S., Appl. Phy. Lett., 2005. **86**: p. 112907.

46. Zeghbroeck, B.V., *Principles of Semiconductor Devices*. 2004, http://ece-www.colorado.edu/~bart/book.

CHAPTER 5

CONCLUSIONS AND FUTURE WORK

Conclusions

Hafnium oxynitride films have been deposited by Metalorganic Chemical Vapor Deposition (MOCVD) and downstream microwave Plasma Enhanced Chemical Vapor Deposition (PECVD) employing different oxidants such as O_2, N_2O, O_2 plasma, N_2O plasma, N_2O/N_2 plasma, and O_2/He plasma in the absence of any post-deposition thermal annealing. The effect of oxidants on deposition kinetics, morphology, composition, bonding structure, electrical properties and thermal stability of deposited films were investigated. Possible chemical/physical reasons for these effects were developed and mechanisms were proposed that are consistent with the experimental results. Oxygen radicals present in the oxidizing environments were found to play an essential role in determining film structures and the resultant electrical properties of deposited hafnium oxynitride films. This systematic investigation into oxidant effects on hafnium oxide/oxynitride thin film CVD represents a new understanding in the area.

For hafnium oxynitride film deposition by MOCVD, both depositions in oxygen and in nitrous oxide show surface reaction controlled kinetics. In the deposition temperature range of 300 – 410 ^{o}C, deposition rates for both oxidants increase with temperature. From Arrhenius plots of hafnium oxynitride film growth rate versus temperature, the effective activation energy (E_a) for oxygen MOCVD is 13.6 kcal/mol while E_a for nitrous oxide MOCVD is 9.9 kcal/mol. The difference in E_a results from the different bond energies for the oxidants. The O-O bond energy in O_2 is 119.2 kcal/mol

while the N-O bond energy in N_2O is 39.5 kcal/mol; thus, nitrous oxide is more extensively dissociated at low temperatures and thereby produces a relatively higher concentration of oxygen radicals when compared to O_2.

Compositions of deposited films were characterized by X-ray photoelectron spectroscopy (XPS). Bulk films deposited in oxygen and in nitrous oxide contain 0.5 – 2.0 atomic percent nitrogen, which indicates that nitrogen atoms cannot be effectively introduced into deposited films by using nitrous oxide as the oxidant in the specific temperature range investigated. Films were etched in dilute HF solutions to assist evaluation of film characteristics. Etch profiles of films show that both films have two layers with different etching rates that can be attributed to different densities and compositions. The composition of interfacial layers was consistent with nitrided hafnium silicate layers. Films deposited in oxygen have much slower etch rates in HF solution than those deposited in nitrous oxide. Compositions of the interfacial region between hafnium oxynitride films and the silicon substrate are also characterized by XPS. Nitrogen content at interfaces is higher than those in the film bulk, demonstrating that nitrogen atoms accumulate at the oxynitride/silicon interface. However, the nitrogen atom accumulation at the interface is more extensive in films deposited in oxygen than in films deposited in nitrous oxide. Also, Hf4f peak positions in the interfacial region are located at higher binding energy than the Hf4f peak position in the film bulk. The shift to higher binding energy is larger for films deposited in nitrous oxide than for films deposited in oxygen. The XPS results indicate that nitrous oxide can provide more oxygen radicals than oxygen, and these radicals can remove nitrogen atoms from deposited films

(especially interfacial layers), thereby increasing the extent of oxidation of the deposited films.

The morphology of deposited films was characterized by grazing incidence X-ray diffraction (GIXRD). Films deposited in oxygen are polycrystalline; the phase is cubic and the crystallite size increases with deposition temperature. However, films deposited in nitrous oxide in the temperature range of 300 – 410 ^{o}C are amorphous according to the GIXRD results. Oxygen atoms are thought to play an essential role in determining the phase of deposited films. Oxygen atoms promote gas phase reactions that produce oxidized film precursor and have a high sticking coefficient on the silicon surface, thus limiting surface diffusion. For these reasons, films deposited with nitrous oxide are amorphous.

Electrical measurements demonstrate that films deposited in oxygen have higher dielectric constants (20-25) than films deposited in nitrous oxide (15-19). The different densities of crystalline and amorphous films are believed to be responsible for this observation. Oxide charge density in oxygen deposited films (5.1e11-3.5e12) is higher than that in nitrous oxide deposited films (3.9e11-2.1e12), and leakage current through the former films is higher than leakage current though the nitrous oxide films. It is believed that oxygen radicals can remove defects such as Si-H, Si-OH and intrinsic oxygen vacancies in the interfacial region or in the high-k film bulk and thus improve the electrical quality of films. Higher deposition temperature can also reduce the oxide charge density and the leakage current because more oxygen atoms can be produced at higher temperatures for both oxidants. Unfortunately, films deposited in both oxidants cannot withstand 900 ^{o}C Rapid Thermal Processing (RTP) for 10 seconds so

incorporating the films into microelectronic fabrication requires the elimination of high temperature processing.

Downstream microwave plasma activated oxidants were also used to deposit hafnium oxynitride films. Kinetics studies display negative activation energies for depositions at temperatures higher than 300-350 ^{o}C, indicating that surface adsorption/desorption is the rate-determining step for PECVD processes. Plasma activation assists dissociation of oxygen and nitrous oxide and introduces energetic oxygen atoms and nitrogen molecules into the deposition atmosphere. Increasing the microwave power from 150 Watts to 450 Watts does not increase the deposition rate, suggesting that no further dissociation of oxidants occurs at higher microwave power. O/Hf ratio in PECVD films is in the range of (2.2 – 2.7), which is higher than the stoichiometric value. Full-width-at-half-maximum (FWHM) of XPS O1s peaks and Hf4f peaks are broadened because a large distribution of bonding structures exists in deposited films. In addition, there is a shift of the binding energies of Hf4f peaks to higher values, indicating that plasma activated oxidants can effectively introduce a oxygen atoms into deposited high-k films. The broadening of O1s and Hf4f peaks and the position shift of the Hf4f peak are more obvious for films deposited by nitrous oxide PECVD than for films deposited by oxygen PECVD, again indicating that nitrous oxide PECVD can introduce more oxygen atoms into films than oxygen PECVD. Excess oxygen atoms in films are believed to be in interstitial positions; with increased deposition temperature, peak broadening and peak shifts were reduced, because less interstitial oxygen is incorporated into films deposited at higher temperature.

Nitrogen accumulation at the oxide/silicon interface is observed for all films formed by PECVD; fewer nitrogen atoms were detected at film/substrate interfaces of films from nitrous oxide PECVD than were detected at film/substrate interfaces of films deposited from oxygen PECVD. A reduction of the N_2O/N_2 ratio or O_2/He ratio does not significantly reduce the O/Hf ratio, nor significantly change the nitrogen concentrations in films. Although plasma dissociated oxidants promote the introduction of oxygen atoms into films, plasma activation cannot efficiently produce nitrogen atoms or NO to incorporate more nitrogen into hafnium oxynitride films. Both films deposited by plasma activated oxygen and nitrous oxide show amorphous morphology. This is further indication that oxygen radicals in deposition processes promote gas phase reactions and retard surface diffusion. Also, incorporated interstitial oxygen atoms can distort the atomic long-range order in deposited films. The dielectric constants of deposited amorphous films increase with deposition temperature and are in the range of 15-25. Interstitial oxygen atoms degrade the electrical properties of films; oxide charge densities are in the range of 6.0e11-3.5e12 /cm^2, which is higher than that in films deposited by MOCVD. Oxide charge density decreases with an increase in deposition temperature, suggesting less incorporated interstitial oxygens at higher deposition temperatures. All deposited amorphous films crystallized after 900 ^{o}C RTP annealing for 10 seconds, which demonstrates that application of these films in semiconductor fabrication with high-temperature annealing steps may be limited.

Based on the results of hafnium oxynitride depositions by MOCVD and PECVD in different oxidants (Table 5.1), it can be concluded that the oxygen radical content in the deposition environment is critical in establishing the morphology, composition, and

electrical performance of deposited high-k films. Prior to the work described in this thesis, little was known about the effects of oxidant on hafnium oxynitride film deposition by CVD. In particular, we believe that this is the first report about the role of oxygen radicals on morphology of high-k films. Results obtained in the thesis have the potential to be extended to other high-k materials (zirconium oxide, zirconium silicate, hafnium silicate and et al) and other deposition techniques (e.g., Atomic Layer Deposition, Physical Vapor Deposition). The results obtained in this thesis contribute to the design of high-k materials processing sequences required for the development of high-k materials for semiconductor device fabrication.

Table 5.1 Summary of properties of films deposited by MOCVD and PECVD in different oxidants. For comparison, industry requirements for high-k materials are also listed.

	Deposition temperature (^{o}C)	Morphology	Dielectric constant	Defect density (/cm^2)	Leakage current (A/cm^2) @ 0.2 MV/cm	Thermal Stability
O_2 MOCVD	350 - 410	Crystalline	20 - 25	5.1e11-3.5e12	6.3e-7 – 1.9e-5	Enhanced crystallinity after 900 ^{o}C RTP
N_2O MOCVD	350 - 410	Amorphous	15 - 19	3.9e11-2.1e12	4.4e-7 – 8.5e-6	Crystalline after 900 ^{o}C RTP
O_2 PECVD	250 – 390 or lower	Amorphous	15 - 25	6.3e11 – 2.1e12	7.8e-7 – 7.9e-6	Crystalline after 900 ^{o}C RTP
N_2O PECVD	250 – 390 or lower	Amorphous	15 - 25	1.4e12 – 3.2e12	1.3e-6 – 3.5e-6	Crystalline after 900 ^{o}C RTP
Industry requirement [1]	Low temperature (<500 ^{o}C)	Amorphous	> 15	10^{10} – low 10^{11} >10^{12}* [2, 3]	10^{-8} >10^{-7} * [4, 5]	Amorphous after 900 - 1000 ^{o}C RTP

* data reported by other research groups

Future Work

Based on various characterization results that have been discussed in the thesis, it is concluded that interstitial oxygen atoms, oxygen vacancies, and -OH, -H groups are important defects in deposited high-k films that likely degrade the performance of dielectrics. Further structural characterization of these defects may help us to know which defects can be significantly affected by oxygen radicals from different oxidants and how oxidants affect the quality of deposited films. For example, electron spin resonance (ESR) at low temperatures can be used to characterize defects such as $\equiv Si \cdot$ and O_2^- because of their unpaired electrons [6, 7]. Fourier-transform infrared spectroscopy (FTIR) can be used to measure the -OH, -H and interstitial O defects in bulk of thin film materials [8-11].

In order to incorporate hafnium oxynitride films into semiconductor device fabrication sequences, the interface between high-k films and the silicon substrate must be as thin as possible so that the Equivalent Oxide Thickness (EOT) of the gate oxide can be reduced to less than 1 nm. Thus, the effect of oxygen radicals on the interface thickness needs to be investigated. Transmission Electron Microscope (TEM) can be used to characterize the interface thickness and morphology. In this way, it may be possible to determine whether oxygen radicals will significantly increase the interface thickness and thus EOT.

From the composition and electrical properties of deposited films, it is concluded that interstitial oxygen atoms are incorporated into the hafnium oxynitride films by PECVD because large concentrations of activated oxygen atoms can be produced by plasma enhancement. Direct gas phase chemistry measurements are needed to confirm

that reasonable concentrations of oxygen atoms remain in the deposition chamber after flowing through a 90 ^{o} bend. It also needs to be confirmed if nitrous oxide PECVD can produce more oxygen atoms than oxygen PECVD. In addition, it will be useful to determine the specific nitrogen species present in N_2O and N_2O/N_2 PECVD so that we can understand why nitrogen atoms cannot be efficiently introduced into films by PECVD. (Quadrupole mass spectroscopy) QMS can be used for the gas phase chemistry characterization [12].

Understanding these fundamental questions by the proposed further studies could provide effective guidance to design and control the deposition process that will help to overcome the current barriers to the introduction of high-k films into high volume integrated circuit fabrication.

REFERENCE

1. Hori, T., *Gate dielectrics and MOS ULSIs: principles, technologies, and applications*. 1997, Springer.
2. O'Sullivan, B. J., Hurley, P.K., O'Connor, E., Modreanu, M., Roussel, H., Jimenez, C., Dubourdieu, C., Audier, M., and Senateur, J. P., 2004. **151**: p. G493.
3. Park, J., Cho, M., Kim, S. K., Park, T. J., Lee, S. W., Hong, S. H., and Hwang, C. S., Appl. Phys. Lett., 2005. **86**: p. 112907.
4. Song, M. K., Kang, S. W., and Rhee, S. W., Thin Solid Films, 2004. **450**: p. 272.
5. Takahashi, K., Funakubo, H., Hino, S., Nakayama, M., Ohashi, N., Kiguchi, T., and Tokumitsu, E., J. Mater. Res., 2004. **19**: p. 584.
6. Kang, A.Y., Lenahan, P.M., and Conley, J. F., J., Appl. Phys. Lett., 2003. **83**: p. 3407.
7. Hurley, P.K., O'Sullivan, B.J., Afanas'eV, V.V., and Stesmans, A., Electrochem. and Solid-State Lett., 2005. **8**: p. G44.
8. Cheng, C.L., Liao, K.S.C., Huang, C.H., and Wang, T.K., Appl. Phys. Lett., 2004. **85**: p. 4723.
9. Kim, B.H., Ahn, J.H., and Ahn, B.T., Appl. Phys. Lett., 2003. **82**: p. 2682.
10. Chabal, Y.J., Raghavachari, K., Zhang, X., and Garfundel, E., Phys. Rev. B, 2002. **66**: p. 161315.
11. Kim, S.S., Stephens, D.J., Lucovsky, G., Fountain, G.G., and Markunas, R.J., J. Vac. Sci. Technol. A, 1990. **8**: p. 2039.
12. Smith, B.C., Khandelwal, A., and Lamb, H.H., J. Vac. Sci. Technol. B, 2000. **18**: p.1757.

VITA

Qian Luo was born on July 12, 1978, in Yifeng, China, to Meiying Wu and Shizhan Luo. He finished his elementary education and secondary education in his hometown. In 1995, he attended Department of Chemistry of Fudan University, Shanghai, where he obtained his Bachelor degree in 1999 and Master degree in 2002. After that, he continued his graduate education in School of Chemistry and Biochemistry, Georgia Institute of Technology, where he obtained his PhD degree in December 2005.